Modelling, simulation and control of the cyclist effort by an intelligent electric bicycle.

Maxime Chorin

THÈSE

Pour obtenir le grade de

DOCTEUR DE L'UNIVERSITÉ GRENOBLE ALPES

École doctorale : EEATS - Electronique, Electrotechnique, Automatique, Traitement du Signal (EEATS)
Spécialité : Automatique - Productique
Unité de recherche : Grenoble Images Parole Signal Automatique

Modélisation, simulation et contrôle de l'effort du cycliste par un vélo électrique intelligent.

Modelling, simulation and control of the cyclist effort by an intelligent electric bicycle.

Présentée par :

Maxime CHORIN

Direction de thèse :

John Jairo MARTINEZ MOLINA PROFESSEUR DES UNIVERSITES, Université Grenoble Alpes	Directeur de thèse
Samuel VERGES DIRECTEUR DE RECHERCHE, Université Grenoble Alpes	Co-directeur de thèse

Rapporteurs :

Nacim RAMDANI
PROFESSEUR DES UNIVERSITES, UNIVERSITE D'ORLEANS
Stéphane PERREY
PROFESSEUR DES UNIVERSITES, UNIVERSITE DE MONTPELLIER

Thèse soutenue publiquement le **2 décembre 2022**, devant le jury composé de :

John Jairo MARTINEZ MOLINA PROFESSEUR DES UNIVERSITES, GRENOBLE INP	Directeur de thèse
Nacim RAMDANI PROFESSEUR DES UNIVERSITES, UNIVERSITE D'ORLEANS	Rapporteur
Stéphane PERREY PROFESSEUR DES UNIVERSITES, UNIVERSITE DE MONTPELLIER	Rapporteur
Samuel VERGES DIRECTEUR DE RECHERCHE, INSERM DELEGATION AUVERGNE-RHONE-ALPES	Co-directeur de thèse
Matteo CORNO PROFESSEUR ASSOCIE, Politecnico di Milano	Examinateur
Christophe BERENGUER PROFESSEUR DES UNIVERSITES, GRENOBLE INP	Président

À ma mamie Malou,

ses inquiétudes,
sa tendresse,
son humour.

Tu nous manques fort.

Acknowledgements

First, I thank the members of the jury. Christophe Bérenguer for accepting to preside my thesis defence. Nacim Ramdani and Stéphane Perrey for reviewing my thesis manuscript and for the relevance and the kindness of their comments. And Matteo Corno, for accepting to be an examinator of my thesis defense.

Then, I thank my thesis supervisors. John Martinez, for trusting me from the very start of our collaboration, for the flexibility and freedom he gave me during this thesis and for his resourcefulness and creativity when solving practical and research problems. And Samuel Vergès, for guiding my exploration of the field of exercise physiology and for our discussions. I also thank them both for the muscular energy spent during the data collection process!

A special thank to Alexandre Sarazin for being such a good colleague and good friend, for his enthousiasm and insights, and for successfully handling the technological matters of the implementation that would have drained me out of patience and hope! A special thank to Ariel Medero, for the journey through LMI based methods and LPV control is sometimes *(often?)* confusing and frustrating and he always was helping and helpful when I hit bottlenecks. For the impromptu and enlightening conversion we had about the works of Li and Horowitz I thank Carlos Canudas De Wit. And a thank to Nadia Rosero, for our fruitful collaboration.

I thank the human resources department of Gipsa-lab, and more specially Virginie Jalliffier-Talmat, who welcomed me on my very first day, and Marielle Di Maria for their efficiency and professionalism.

For the development of the the e-bike prototype I thank all the members of the technical staff of Gipsa-lab who contributed, in particular Sylvain Geranton for the microcontroller board and Jonathan Dumond. I also thank the staff of the HP2 research laboratory for handling the exercise sessions during data collection. And thanks to Hervé Dubouchaud for providing the gas exchange analyzers used for data collection.

For welcoming me and accommodating for me during my stays in Uppsala University I thank Alexander Medvedev, Åsa Cajander and Pär Ågerfalk.

A thesis is a long and personal journey. During mine, I frequently found myself in conversations saying "*I am* doing a thesis". I realize now that even though this sentence is correct, it

is not very meaningful. Of course, for each PhD subject there is one and only PhD student. Of course, this student is the main manager and the main executor of the work done over the thesis. However, in the end, the thesis is filled with much more than this. It is filled with encounters and memories that make the thesis a meaningful and deep life experience. Here, I want to thank the people who made this thesis for me.

My first words go to Estéban Carvalho, with whom I not only shared this journey, but also true moments of complicity in the ups and in the downs. I thank you for all the initiatives you took in order to bring everybody together, for sharing your passion of mountains with me and for being a friend for life.

Maria Castaldo, thank you for your generosity and for creating beautiful memories for all of us, we owe you.

Ariel Medero, thanks for filling our parties with dances and fueling them with your famous *Arielito*!

Mariana Mulinari Pinheiro Machado *and Omairi (depending on the timing?)*, thanks for shining your happy beams wherever you are and whoever you are with, and most importantly for the *Paçoquitas*, candies from heaven!

Louise da Costa Ramos, thank you for being such an open and enthusiastic person and also for the dance moves you taught me, I will make good use of them!

Lucas and Layana da Silva, thank you for being kind and positive, I wish you the best with your little family!

Nicolas Vanspranghe, thank you for being the best nerdy travel buddy on the way to Nice! I wish you success in your post-doc and your future *Warcraft* multiplayer campaigns.

Bob Aubouin Pairault, Patrick Omairi, Houssem Meghnoudj *grand gaillard*, thank you for the teamwork and resourcefulness during the pirate challenge, GIPSABORDAGE! And thank to the other Gipsa-boys for the fun competition.

Matthias Réus, thank you for the improvised party night, it was a lot of fun!

Sohaïb El Outmani, thank you for the insights of the start-up world and for making our lunches tastier during the pandemic!

Chhayarith Heng Uy, thank you for the helpful conversations during my thesis writing.

Elena Romero and Antoine Quentin, thank you for the memories in Cyprus and the amazing parties at your place!

Mônica Spinola Felix, thank you for the nice discussions. *Libra gang!*

Lakshitha Daham Makewita, thank you for being part of our little adventures in Gotland, and Sashini also for the amazing Sri Lankan food!

Laurent Brincat, thank you for the extensive and original tour of Milan you planned for us during the two trips we took there, and thanks for all the fun *Vagante* games!

Jean Phillipe Bias, Thank you for the week-end in Aix-les-Bains and for the hike at the *dent du chat*!

Rémi Bazinette *a.k.a Rémo*, thank you for all the fun dinner nights and for taking us to unexplored territories aboard the *Rémobile*!

Thanks to all of you and to all the people I did not name here, you made my journey rich and colorful and I wish you the best in your future professional and personal projects!

At this point, I want to address a very special thank you to Shweta. When we met in India four years ago I like to think that I already had the stem of a taste for research but that you convinced me to let it grow, which I never regretted. Time flew since we met, and we now have many precious memories together and I am certain that more will come, given your ability to make me leap out of my comfort zone! Your honesty is refreshing, your insights stimulating and you have not forgotten how to see the world with the eyes of a child which makes your company so special. For trusting me with your friendship, thank you.

Of course, all of this would not have been possible without the unconditioned support of my family. Maman, Papa, there are things that this thesis could not teach me, since you had done a perfect job years ago. You taught me the importance of education, of finding an occupation in which I would truly believe. You taught me to be sincere in my work, whatever the outcome. But most importantly you always supported me, trusted me and made me believe that nothing was out of reach. I love you tenderly, forever.

Thanks to my sister Roxane, for keeping me in touch with the homeland and for the unexpected visits you gave me!

Thanks to my uncle Eric and my aunt Françoise, for welcoming me, making me feel at home and taking care of me. You are people I can always open and share with which is very precious.

Thanks to my *(other!)* uncle Eric, for the interest you showed in my work and for the kind comments about my manuscript.

Thanks to my papi Albert, for making me feel taller and stronger than I really am, for improving substantially the quality of my reports and for introducing to mechanics and robotics when I was a kid.

Thanks to my mamie Claudine, for the support and the regular and heartly phone calls you gave me.

Abstract

This thesis concerns the control of the effort of a cyclist by an intelligent electric bicycle. The main idea is to use the electrical assistance of an e-bike in order to increase or lower the mechanical load perceived by the cyclist. The effort level is chosen based on the physiological characteristics of the rider formulated in terms of respiratory gas exchange. Thus, the solution proposed constitutes a *personalized* and *automatic* strategy to control the exercise intensity perceived by the cyclist.

In order to solve this problem using control system theory, a dynamical model is proposed in order to describe the effect of exercise on the cyclist. On the physiological point of view, a dynamical model describing the evolution of the *oxygen consumption* and *carbon dioxide production* under the form of a Linear Parameter Varying (LPV) model, is used. On the biomechanical point of view, the action of cyclist on the pedal is modeled using a pedalling *force-velocity characteristic*. Both models depend on the considered individual and are identified using experimental data collected during biking sessions. The proposed model for the cyclist is then used in order to simulate the physiological behaviour of a cyclist in simulations and in order to formulate estimation and control laws.

Because respiratory gas exchange is used in order to characterize the physiological reaction of the cyclist to exercise, it is important to access it in real time in order to adapt the assistance provided by the bike. However, because direct measurements are cumbersome and costly, methods aiming at *estimating* respiratory gas exchange during exercise are proposed in this thesis. The first method is based on an Explicit Error Bounds Set-Membership state observer and allows the estimation of the oxygen consumption and carbon dioxide production of the cyclist with uncertainty bounds computed based on hypotheses regarding the noise level affecting the model. The second method is a robust Proportional Integral state observer which allows the reconstruction of the Basal Metabolic Rate (BMR) of the cyclist, as well as respiratory gas exchange. Both state observers are formulated by solving Linear Matrix Inequalities (LMI) problems and suppose a direct measurement of carbon dioxide production or minute ventilation. Both methods are validated in simulation using experimental data.

Finally, in order to control the physiological response of the cyclist during exercise, the electrical assistance of the bike is adapted in real time. To do so, control laws are used in order to automatically choose the level of assistance to provide to the cyclist based on physiological

considerations and on the objectives set. Two control strategies are proposed in this thesis. The first solution is based on a Proportional Integral (PI) controller. The second one is based on a Linear Quadratic Regulator (LQR). Both control strategies enable the control of either the oxygen consumption or carbon dioxide production of the cyclist during exercise. These control strategies are designed in simulation and validated indoor and outdoor during real cycling tests.

Table of Contents

List of Tables

Table **Page**

List of Figures

Figure **Page**

Chapter 1

Introduction

Contents

1.1 Research environment and funding

This thesis was fully supported by a *contrat doctoral* provided by the French *Ministère de l'enseignement supérieur, de la recherche et de l'innovation*. It is the product of the collaboration of two research units from the *Université Grenoble Alpes* :

- The mixed *CNRS* and *Grenoble-INP* research team *SAFE* from the *Gipsa-lab* laboratory.
- The *INSERM* research team *Hypoxie-Exercice* from the *HP2* laboratory.

The major of the thesis is *Automatic Control and Production Systems*, which belongs to the doctoral school *EEATS* of the *Université Grenoble Alpes*.

1.2 Context of the thesis

1.2.1 The growth of biking

More than two hundred years have passed since the very familiar bike technology was proposed by baron Karl Von Drais in Germany in 1817, and yet the 21th century is on the verge of re-introducing it as a key solution to modern issues. With the *Pan-European Master Plan for Cycling Promotion* [4] 27 European countries agreed on investing in infrastructures, research and policies to put biking at the center of global strategy for better health, transport and environment. The expected impact of this plan is multi-fold :

- On *health*, the increase in regular physical activity associated with biking increases the average life expectancy. In addition, commuting by bike promote social physical distancing and reduces the risks of contamination, which is more than relevant in this covid pandemic times.
- On *sustainability*, the use of bikes implies a drastic decrease in noise, fine particles and carbon dioxide emissions compared to fossil-fuel based solutions.
- On *transportation*, because bikes are extremely space and energy efficient they are expected to reduces traffic and congestion.
- On *economy*, because the use of bikes for small trips encourages proximity shopping.

Moreover, users have now access to a large variety of biking technologies. In addition to the classical mechanical bike, affordable electrical solutions are available. Examples are the Powered Bicycles (PB), which can move solely using their electrical motor, or Power Assisted Bicycles (PAB), which use the electrical motor to enhance the cycling capacity of the rider. Electric bicycles, or e-bikes, were first proposed in Japan in 1980s [6] to ease the access to biking to elderly communities. The first models were limited by the weight of electrical motors and the

autonomy of batteries but in the 2000s, the development of Li-ion batteries and the dramatic increase in their efficiency as well as a reduction of their cost, made the e-bike technology a real alternative on the market.

Thanks to their increased speed, lesser feeling of exhaustion and a reduced environmental impact, e-bikes convinced city commuters to keep their car in the garage [9]. Medium and large cities started implementing Intelligent Transport Systems (ITS) such as Bike Sharing Systems (BSS) or E-Bike Sharing Systems (EBSS) allowing users to pick and drop a bike using an app for their transportation [8]. This market is in expansion, with an annual growth rate of 79.3% for both BSS and EBSS combined between 2008 and 2018.

1.2.2 Exercise to tackle sedentary behaviours

As stated in [11], sedentary behaviours can be defined in opposition to physical activity :

"physical activity is defined as any bodily movement produced by skeletal muscles that requires energy expenditure and can be performed at a variety of intensities, as part of work, domestic chores, transportation or during leisure time, or when participating in exercise or sports activities. At the low end of the intensity range, sedentary behavior is defined as any waking behavior while in a sitting, reclining or lying posture with low energy expenditure".

and examples of sedentary behaviors are watching television, working on a computer, playing video games, reading or phone calling. In France, in 2015, the ESTEBAN study [1] pointed out that physical inactivity is spreading in the population. For example, adults spend an average of 6 hours and 35 minutes inactive during a day. This number tends to be worse for younger adults, with 7 hours a day for 18-39 years old, compared to older adults, with 5 hours 48 minutes for 55-74 years old. Sedentary behaviors are very widely spread, with 89% of the population qualifying for moderate to high levels of physical inactivity.

This high level of physical inactivity has a negative effect on the health of the population. The World Health Organization (WHO) reported that physical inactivity had direct consequences on all-cause mortality, cardiovascular mortality, cancer mortality, cardiovascular disease incidence and type-2 diabetes incidence among others [3], which directly translates in a reduced life expectancy. Furthermore, direct consequences of physical inactivity like diabetes, obesity or heart diseases, recently turned out to be comorbidities in case of covid 19 contamination which increased the likely of occurrence of severe form of the disease and complications. In France, the cost related to physical inactivity was estimated to be as high as 17 billions euros per year in 2018 [10], with 87% of this amount being attributed to the direct cost on health systems and 12% of this amount to productivity losses. Worldwide, physical inactivity is considered responsible of up to 3.2 million deaths each year according to the WHO [7].

In order to tackle this issue, the WHO published a set of guidelines and suggestions addressed to policymakers [2] such as :

- spreading knowledge about the risks and benefits associated with physical activity and inactivity using advertisement campaigns, training of health and education professional, creation of MOOCs and podcasts, etc.

- enabling active transportation modes like biking or walking by restricting the access of specific areas to motor vehicles, reducing the maximum speed limits, building cycling paths, etc.

- encouraging the practice of a physical activity in schools and workplaces.

1.2.3 Prescribed exercise for prevention and therapy

According to the WHO, a regular physical activity plays a role in preventing non-communicable diseases such as cardiovascular diseases, type-2 diabetes, breast or colon cancer and the maintenance of a healthy weight [3].

In addition to this prevention role, exercise is also used as an active part of treatments for chronic diseases [5]. The intensity, frequency and duration as well as the type of prescribed exercise sessions are tailored to the patient's physical aptitudes and psycho-social resources so that the risks-benefits trade-off is maximized. For example :

- for type-2 diabetes, muscle strengthening combined with endurance activities of moderate to strong intensity is advised.

- for chronic obstructive pulmonary diseases (COPD), long-term regular endurance and muscle strengthening is advised.

- for asthma, endurance exercise increasing the maximum aerobic capacity (VO_{2max}) is advised.

Nowadays, these sessions are mostly performed at the hospital, under the supervision of health professionals like in the university hospital of Grenoble, in the *Sport et Pathologies* department. As stated in [5], the success of such approaches depends on their flexibility in terms of intensity, frequency and duration in order to fit the patients' needs but also on the understanding and control the patients have of their treatment. They are often assisted by technology with the patients' vital signals being monitored during the exercise sessions and the use of tunable cycle-ergometer or treadmills.

1.3 Thesis motivation and objectives

The objective of this thesis is to design theoretical and practical solutions to the problem of controlling the physiological response of a given individual during biking exercise using the electrical assistance of an e-bike. The main motivation is to propose a device, here an electric-bike, able to control the intensity of exercise in an automatic fashion and in an uncontrolled setup. The assistance strategy is personalized to the user with the use of a respiratory gas exchange model identified using personal exercise data. Such electric-bike provides new guarantees compared to the ones commonly proposed on the market, for which the assistance strategy does not depend on a physiological understanding of the user. Such electric-bike could be found suitable in rehabilitation strategies or personalized training strategies.

To achieve this objective, multiple problems are tackled :

- First, the dual system {cyclist and e-bike} to be controlled is modelled in order to simulate its behavior and apply control systems theory.
- Second, to estimate in real-time the evolution of such system, state observers and estimators are designed.
- Finally, using the previous items, a control law for the electrical assistance of the e-bike is proposed in order to regulate physiological quantities during cycling.

The organization of the manuscript is the following :

- In chapter one, an overview of the phenomenon determining the response of the human body to exercise *from the exercise physiology perspective* is given. This overview includes a description of the different metabolic pathways used in order to produce mechanical power, of the different regimes of exercise. This chapter also covers the role played by respiratory gas exchanges, such as oxygen consumption and carbon dioxide production, during exercise. The muscle structure is also presented and the effects of training are described.
- In chapter two, an overview of the models proposed to describe an exercising individual *from the control science perspective* is given. First, different models previously proposed to describe the evolution of respiratory gas exchange or heart rate during exercise are presented. Then, a more detailed description of the respiratory gas exchange model chosen for this thesis is given, with an explanation of its structure, of its identification protocol and of its validation. Finally, a novel approach is proposed in order to simulate the behavior of an exercising cyclist in simulation. This approach is based on a force-velocity characteristics which allows to generate realistic mechanical and physiological signals for any predefined exercise session.

- In chapter three, estimation strategies are proposed in order to estimate respiratory gas exchange during exercise. First a set-membership state observer is proposed and its performances are analyzed in simulation. Then a robust proportional integral observer is proposed in order to tackle the influence of model uncertainties in estimation. The use of a discrete-time Kalman filter, coupled with a heart rate characteristic, is explored in order to estimate respiratory gas exchange in a non-invasive way. Finally, an external force estimator is proposed based on a robust proportional integral state observer.

- In chapter four, two control strategies are proposed in order to control the respiratory gas exchanges of the cyclist during exercise. The first strategy is based on a proportional integral controller and the second on a linear quadratic regulator. Both control strategies are validated in simulations and experimentally using an e-bike prototype. Also, the simulation strategy proposed in Chapter 3 is validated using the data collected during experimental scenarios.

1.4 Contributions of the thesis

The main contributions of the thesis are the following :

- A large review of literature is given regarding the modeling and control of physiological variables during exercise, from the physiology and the control science perspectives.

- A model of the mechanical behaviour of the cyclist based on the use of a pedalling force and velocity characteristic is proposed. An experimental protocol is proposed in order to identify this characteristic from experimental data. This model is then used in order to simulate realistic cyclist behaviours for arbitrary biking scenarios.

- Two strategies are proposed in order to estimate the respiratory gas exchanges of an exercising cyclist. The first one is based on a set-membership observer which allows to define uncertainty bounds on the estimation. The second one is based on a robust proportional integral observer and in addition to the respiratory gas exchange variables, estimates the basal metabolic rate of the cyclist during exercise.

- Finally, two strategies are proposed in order to control the respiratory gas exchanges of an exercising cyclist using the electrical assistance of an e-bike. The first one is based on a proportional integral controller and the second on a linear quadratic regulator. Both strategies aim at automatically choosing the level of electrical assistance to control the intensity of the effort of the cyclist.

Bibliography

[1] Etude de santé sur l'environnement, la biosurveillance, l'activité physique et la nutrition (Esteban 2014-2016).
Rapport du ministère de la Santé, Ministère de la Santé, France, September 2017.

[2] PLAN D'ACTION MONDIAL DE L'OMS POUR PROMOUVOIR L'ACTIVITÉ PHYSIQUE 2018-2030.
Technical report, Organisation Mondiale de la Santé, 2019.

[3] WHO GUIDELINES ON PHYSICAL ACTIVITY AND SEDENTARY BEHAVIOUR.
Technical report, World Health Organization, 2020.

[4] Pan-European Master Plan for Cycling Promotion.
Health and Environment, page 57, 2021.

[5] Julie BOICHE, François CARRE, Béatrice FERVERS, Damien FREYSSENET, Isabelle GREMY, Thibaut GUIRAUD, Cédric MORO, Christelle NGUYEN, Serge POIRAUDEAU, Grégory NINOT, Claire PERRIN, Alain VARRAY, Agnès VINET, and Guillaume WALTHER.
Physical activity, prevention and treatment of chronic diseases.
Technical report, EDP Sciences, January 2019.

[6] Jennifer Dill and Geoffrey Rose.
Electric bikes and transportation policy: Insights from early adopters.
Transportation research record, 2314(1):1–6, 2012.

[7] Philippe Furrer.
LA SANTÉ EN ACTION – No 454 – Décembre 2020 Promouvoir la santé par l'activité sportive et physique.
(454):4, 2020.

[8] Nikolaos-Fivos Galatoulas, Konstantinos N Genikomsakis, and Christos S Ioakimidis.
Spatio-temporal trends of e-bike sharing system deployment: A review in europe, north america and asia.
Sustainability, 12(11):4611, 2020.

[9] Tim Jones, Lucas Harms, and Eva Heinen.
Motives, perceptions and experiences of electric bicycle owners and implications for health, wellbeing and mobility.
Journal of transport geography, 53:41–49, 2016.

[10] Laurence LEFEVRE.
Activité physique et sportive, santé et qualité des finances publiques.
publication du ministère des Sports, January 2018.

[11] on behalf of SBRN Terminology Consensus Project Participants, Mark S. Tremblay, Salomé Aubert, Joel D. Barnes, Travis J. Saunders, Valerie Carson, Amy E. Latimer-Cheung, Sebastien F.M. Chastin, Teatske M. Altenburg, and Mai J.M. Chinapaw.
Sedentary Behavior Research Network (SBRN) – Terminology Consensus Project process and outcome.
International Journal of Behavioral Nutrition and Physical Activity, 14(1):75, December 2017.

Chapter 2

Exercise Physiology Concepts

Contents

Anybody can describe the feelings associated with the practice of sport, of a long or short exercise. The warming up of the body, with each breath getting longer and deeper, the increase of the heart rate and its resonating sound in the head. The feeling of exhaustion, getting out of breath, with cramps and muscle pains. Also, the feeling of wellness, when drinking water or eating, after a sport session. However, not anybody can describe in detail the physiological processes ensuring the adaptation of the body to exercise. Exercise physiology is the branch of science dedicated to the understanding of this topic and in this chapter, we will try to summarize its key aspects.

2.1 The metabolic pathways during exercise

During exercise, a human organism transforms chemical substrates stored in the body such as glucids, lipids or proteins into an organic compound called *adenosine triphosphate* (ATP). ATP is the chemical energy currency used in the cells to produce muscular contractions during effort. Energy is produced when ATP is hydrolyzed to adenosine diphosphate (ADP), by losing a phosphate compound (P_i). It is stored in small quantities in the cells, in order to ensure the first 5 seconds of contraction, but has to be produced in a continuous fashion to ensure the power production during exercise. To do so, multiple chemical reactions happen in parallel producing ATP. Each of these reactions also create by-products such as lactate or carbon dioxide which have to be processed by the organism in order to maintain the homeostasis, the nominal steady state of the body. In the following, an overview of the four main pathways for ATP production and their use during exercise is given.

Two main distinctions are made in order to differentiate the metabolic pathways of exercise. The first one regards the use of dioxygen (O_2), or not, in the reactions. In the case where dioxygen is not required, the reaction is labeled as *anaerobic* and when it is the reaction is labeled as *aerobic*. The second distinction regards the production of lactate (La) in the process. In the case where lactate is not produced the reaction is *alactic* and in the case where lactate is produced the reaction is called *lactic*.

2.1.1 The phosphagen pathway

The first pathway to mention is the phosphagen pathway. This pathway is anaerobic, and is the first one to be triggered when an effort is performed. This pathway uses the phosphocreatine (PCr), stored in the muscles, to produce ATP in a very fast and intense fashion. The reaction used is the following :

$$PCr + ADP \rightleftharpoons ATP + Cr \tag{2.1}$$

However, PCr is stored in little quantities in the muscles, and this pathway can only be activated in the first seconds of exercise, until the PCr resources are empty. Reaction (2.1) is

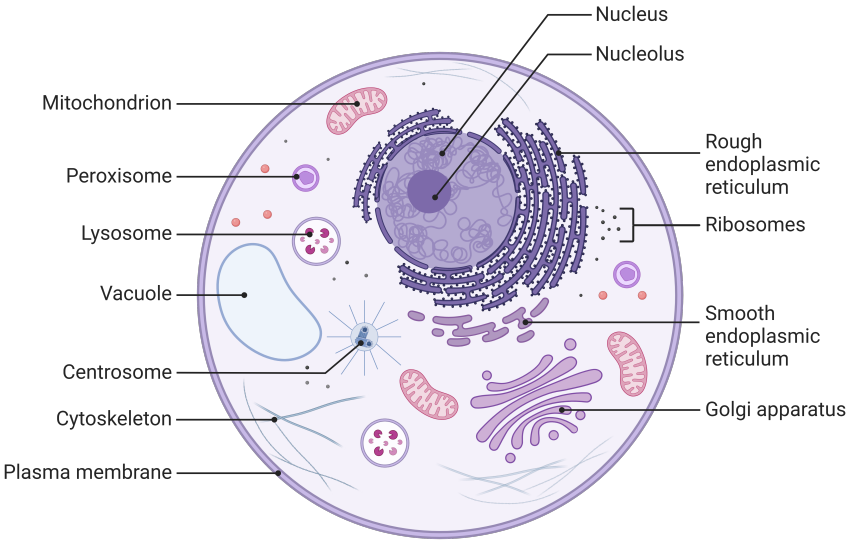

Figure 2.1: Diagram of a eukaryote cell.

reversible, and during rest the stocks of PCr are replenished.

2.1.2 The anaerobic alactic pathway

The anaerobic pathway starts in the cytoplasm of the cell with the glycolysis. The glycolysis is a chemical reaction oxidizing a molecule of glucose into pyruvate. Glycolysis can be expressed as a total of 3 different chemical reactions happening in parallel :

$$\text{glucose} + 2NAD^+ \rightarrow 2 \text{ pyruvate} + 2NADH + 2H^+ \tag{2.2}$$

$$NAD^+ + 2H^+ + 2e^- \rightleftharpoons 2NADH + H^+ \tag{2.3}$$

$$2ADP + 2P_i + 2H^+ \rightarrow 2ATP + 2H_2O \tag{2.4}$$

These reactions are summed up in Fig. 2.2.

Equation (2.2) corresponds to the oxidation of glucose in pyruvates. This reaction is catalyzed by reaction (2.3) corresponding to the NAD interconversion reaction, a reversible catalytic reaction ensuring protons and electrons mobility.

Equation (2.3) is a net reaction, equivalent to the oxidative phosphorilation, and produced over the course of glycolysis.

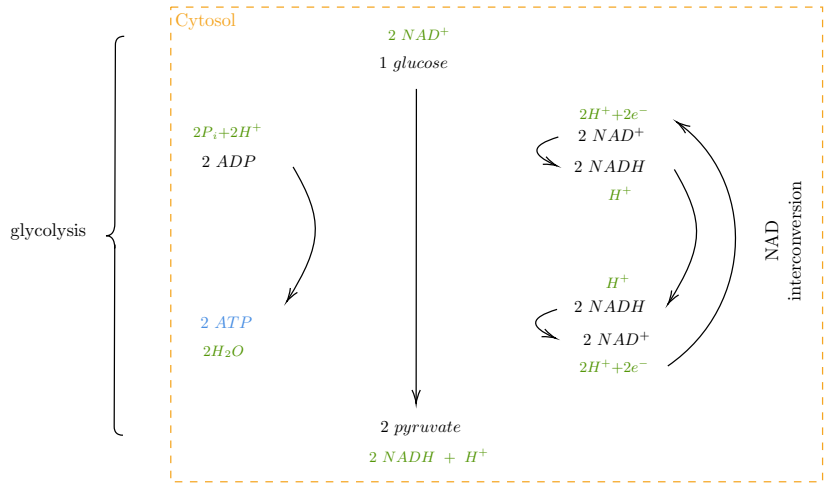

Figure 2.2: This diagram represents the reaction of glycolysis, constituted of the oxydative phosphorilation (2.4) *(on the left)*, the oxydation of glucose (2.2) *(in the middle)*, of the NAD interconversion (2.3) *(on the right)*. This reactions results in the production of ATP and pyruvate from glucose.

At this point, pyruvate and ATP are produced from glucose and without using oxygen. Glycolysis is thus *anaerobic*. However, two different following reactions using the pyruvate are possible. The first one is the pyruvate decarboxylation, which occurs in presence of oxygen and degrades pyruvates without producing lactate. The metabolic pathway composed of the glycolysis followed by the pyruvate decarboxylation is called the *anaerobic alactic* pathway. It is depicted in Fig. 2.3.

For the chemical reaction to occur, the pyruvate is first moved from the cytosol of the cell inside a mitochondrion. A figure of a eukaryote cell is depicted in Fig. 2.1. There, it reacts with a Coenzyme-A (CoA), to form Acetyl-CoA, used in the mitochondrion in the Krebs cycle, and carbon dioxide (CO_2). Like in glycolysis, this reaction is catalyzed by the NAD interconversion.

$$2 \text{ pyruvate} + 2NAD^+ + \text{CoA} \rightarrow 2 \text{ acetyl-CoA} + 2NADH + 2CO_2 \tag{2.5}$$

2.1.3 Anaerobic lactic pathway

In order to deal with the pyruvate produced by the glycolysis in absence of oxygen, a different reaction takes place in the cytosol : the fermentation. This reaction produces lactate (La), responsible for the acidification of the muscle which translates into muscle fatigue and pain. Again, this reaction is catalyzed by the NAD interconversion. It is depicted in Fig. 2.4. The metabolic pathway composed of the glycolysis followed by the fermentation is called the *anaerobic lactic* pathway.

$$\text{pyruvate} + NADH \rightarrow La + NAD^+ \tag{2.6}$$

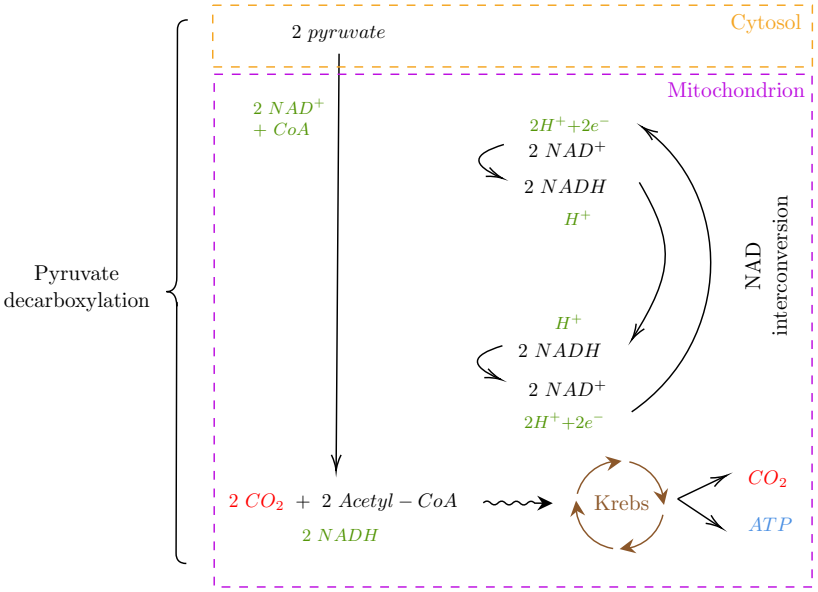

Figure 2.3: This diagram represents the reaction of pyruvate decarboxylation (2.5) *(on the left)*. This reaction results in the production of ATP and CO_2 from the pyruvate produced by the glycolysis (2.2). The glycolysis together with the pyruvate decarboxylation constitute the *anaerobic alactic pathway.*

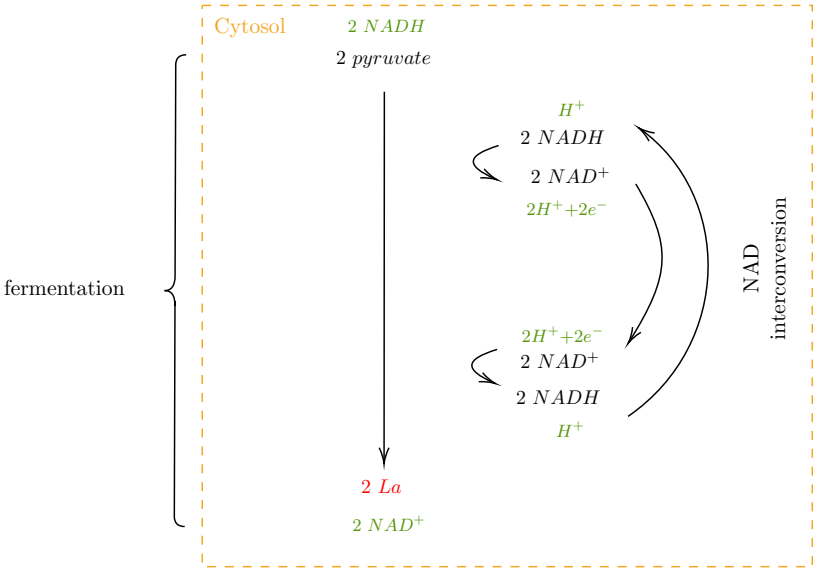

Figure 2.4: This diagram represents the reaction of fermentation (2.6) *(on the left)*. This reaction produces lactate (La) from the pyruvate produced by the glycolysis (2.2). The glycolysis together with the fermentation constitute the *anaerobic lactic pathway.*

Lactate is then either used as a substrate in the Krebs cycle (also called the citric acid cycle) in order to produce additional ATP or is cleared by the organism. There are multiple lactate clearance mechanism, the main ones are the lactate oxidation and the glyconeogenesis.

The lactate oxidation occurs in the cytoplasm of the muscle cells. It is depicted in Fig. 2.5.

This reaction consists in the oxidation of the lactate back to pyruvate and is catalyzed by the lactate dehydrogenase enzyme according to the following equation :

$$2La + 2NAD^+ \rightarrow 2 \text{ pyruvate} + 2NADH \tag{2.7}$$

Gluconeogenesis is a part of the Cori cycle in which the lactate present in the muscles is moved to the liver in order to be converted to glycogen which will later be used to generate glucose.

During intense workout, the previously mentioned clearance mechanism can fall short in comparison to the rate of production of lactate. This implies a rise in the muscle and blood lactate concentration called the lactate threshold. This threshold can be used in order to define the tolerance of a training individual to exercise intensity by identifying the maximal power output that can be sustained without an increase in lactate concentrations. This intensity is coined as the maximal lactate steady state (MLSS).

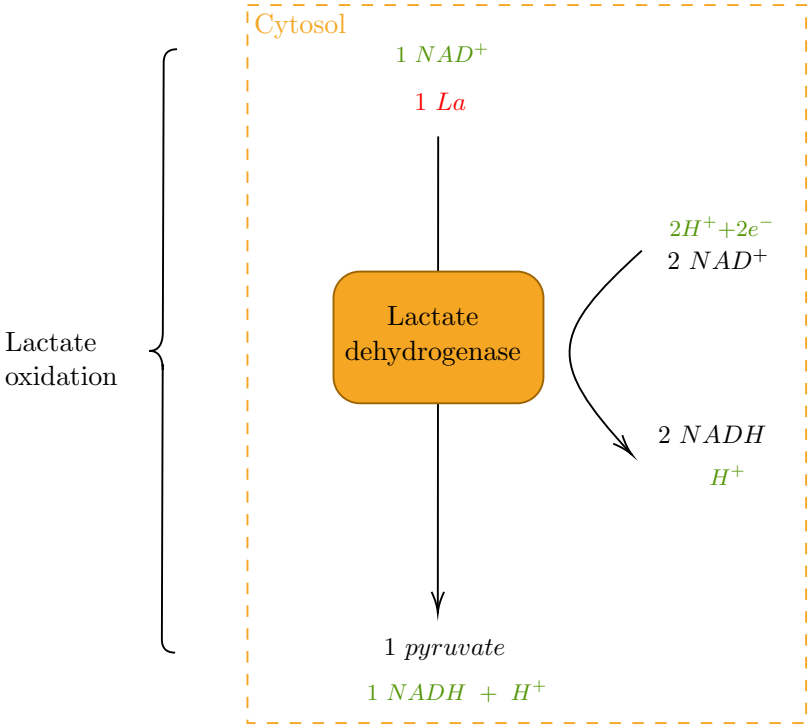

Figure 2.5: This diagram represents the reaction of lactate oxidation (2.7). This reaction produces pyruvate from the lactate (La) produced by the fermentation (2.6).

2.1.4 The aerobic pathway

The last pathway is the *aerobic pathway*. This pathway requires an adequation of the oxygen supply and demand of the organism to face the intensity of the effort. This pathway is the main

one used throughout our lives and is the most efficient. This pathway uses glucose, with the oxydative phosphorilation, or fatty acids, with the β-oxidation, as substrates.

The oxidative phosphorilation occurs in the matrix of the mitochondria. For this reaction to happen, a *proton gradient* is required between matrix of the mitochondrion and the inter-membrane space of the mitochondrion. This means that protons H^+ have to displaced from the matrix to the inter-membrane space. This task is performed by the electron transport chain.

The electron transport chain is a series of reactions happening in the matrix and its membrane in which a flow of electron implies the displacement of protons from the matrix to the inter-membrane space. Electron carriers like succinate $FADH_2$ or nicotinamide adenine dinucleotide $NADH$ are oxidized under the action of proteins (or complexes) resulting in the transport of protons H^+. Also, water H_2O is formed after an atom of oxygen O accepts two electrons and two protons ; the energy released by this reaction is used to move additional protons through the membrane.

Then, the imbalance in protons between the matrix and the inter-membrane space is used to power the oxidative phosphorilation. The protons come back to the matrix through the complex 5 (or ATP synthase). The movement of protons back to the matrix mechanically enables the reaction of phosphorylation, producing ATP. This reaction is depicted in Fig. 2.6.

A summary of the different reactions involved in the aerobic and anaeroic pathways is given in Fig. 2.7

2.1.5 Metabolic pathways activation and efficiency

The type of metabolic pathway that is used during exercise depends on different factors. The first factor is the *duration of the effort*.

When an individual is performing an intense effort in a sudden manner (a sprint for example), the organism has to face a high power expenditure with the cardiovascular and ventilatory systems close to resting performances. The oxygen and substrates required to use the aerobic pathway cannot yet reach the muscles and other pathways are used to cope with the cardiovascular and ventilatory systems response time. The pathway activation is described in Fig. 2.8.

1. The first ATP molecules to be consumed are the “free” ATP stored in the muscle cells. Because they are stored in very little quantities, they can only fuel the effort during the first 5 seconds.

2. The phosphagen pathway is then used, using the phosphocreatine molecules in the muscle to produce ATP. This pathway is mainly used for very high intensity efforts in very short periods of time (such as weight lifting). Again, because phosphocreatine is stored in little quantities in the muscle, this pathway is not sustainable for more than 10 seconds.

3. Then, during the first two minutes, the anaerobic pathway is used.

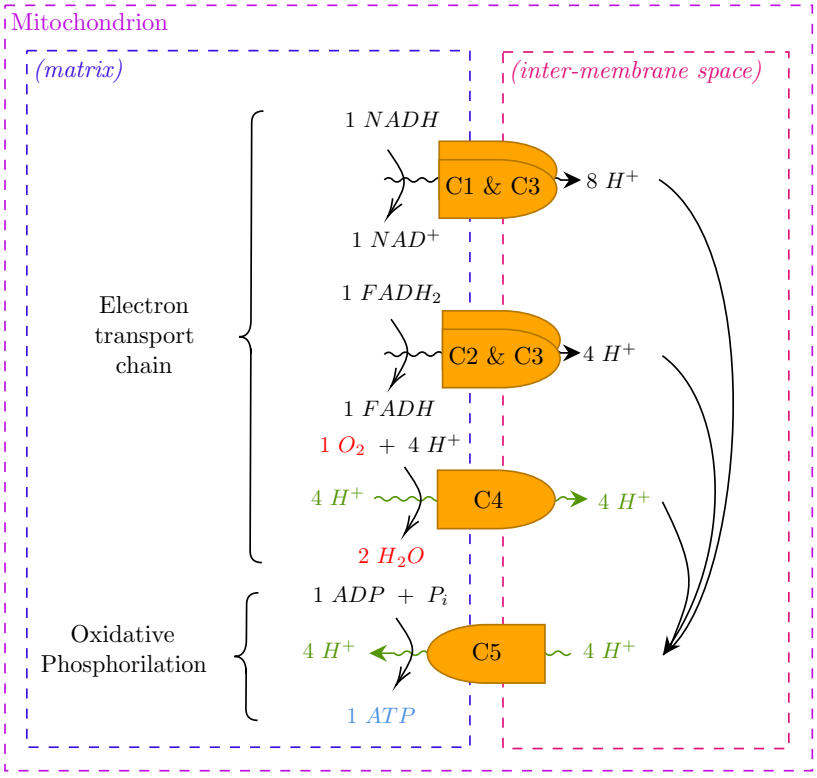

Figure 2.6: This diagram represents the reaction of oxidative phosphorilation. First, the electron transport chain moves protons H^+ from the matrix to the inter-membrane space. Then, this H^+ gradient is used to power the oxidative phosphorilation as the protons move back to the matrix from the inter-membrane space. This reaction constitutes the *aerobic pathway*.

4. After two minutes, the heart rate and ventilation have reached their steady state. The muscles are well alimented with oxygen and substrates and the aerobic pathway is used.

The second factor is the *intensity of the effort*, meaning the power output required.

At high effort intensity, the human body can reach physiological limits, preventing certain pathways to be used sustainably. It is agreed on that one of the main factors limiting the exercise capacity is the oxygenation. This translates in an index called VO_{2max}, corresponding to the maximal oxygen intake (in L/min). This index depends on the individual and is susceptible to be increased through training. An overview of this concept is given in [1].

Multiple factors can explain this plateau in oxygen consumption during effort :

1. The limitation of the cardiac output is one of them [17]. Cardiac output is defined as the product of heart rate and stroke volume and is expressed in L/min. While the maximal heart rate during exercise is mostly explained by age, the stroke volume is likely to be improved with endurance training. A larger cardiac output allows to move larger quantities of oxygen from the lungs to the muscles.

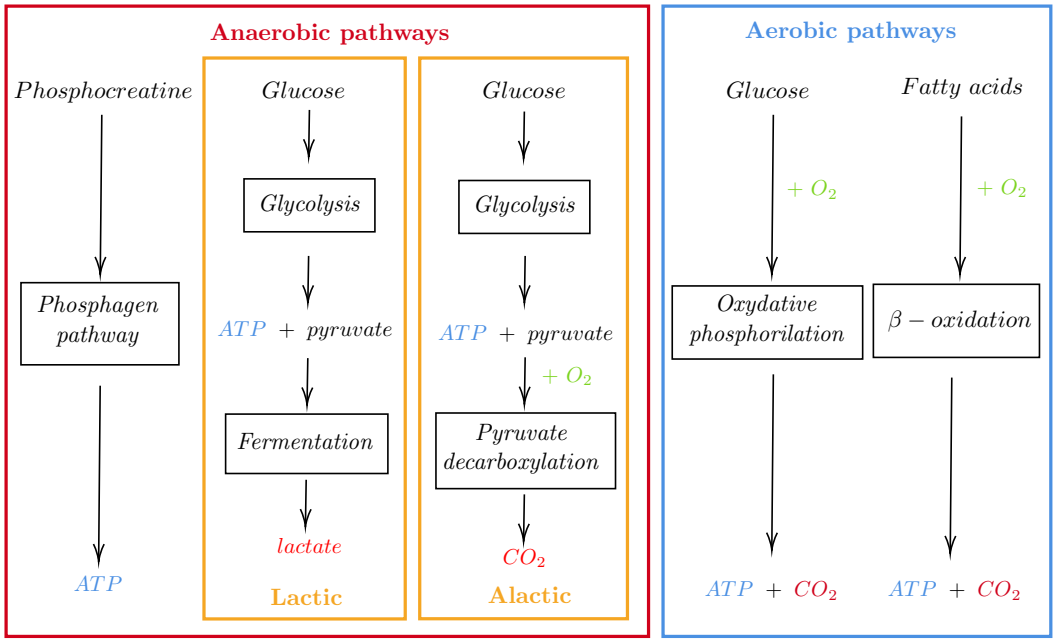

Figure 2.7: This diagram is a summary of the different reactions involved in the *aerobic* and *anaerobic* pathways.

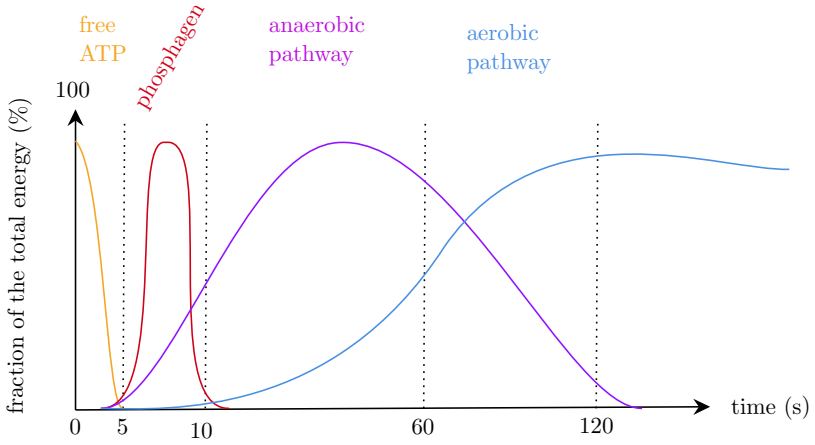

Figure 2.8: This diagram represents the chronology of activation of the different exercise pathways, from the onset of exercise to steady state.

2. An other factor is the pulmonary diffusion. Pulmonary diffusion is the capacity of the lungs to exchange oxygen and carbon dioxide between the blood and the atmosphere. For untrained individuals, this factor is rarely limiting but it can come into play for highly trained athletes.

3. The blood volume and flow is also to be taken into account. Blood, and more precisely, red blood cells, are responsible for carrying the oxygen from the lungs to the muscles. Endurance training is susceptible to increase the total blood volume, by increasing the

plasma volume. Increasing the blood volume reduces its viscosity, which improves the oxygen distribution to the muscles.

4. Substrates availability plays a significant role as well. In particular, glucose resources, which are replenished by eating carbohydrates, can run low during endurance exercise and limit the performances of the individual.

When muscles are not well oxygenated, anaerobic pathways are used to compensate the limitations of the aerobic pathway. The anaerobic pathway is not sustainable and such rate of exercise can not be maintained for a long period of time without consequences. Thus, the terms *aerobic* and *anaerobic* are used to characterize the regime of effort as well : when only the aerobic pathway is used (in low effort intensity) the effort is labeled as *aerobic* and when anaerobic pathways add up to it (in high effort intensity) the effort is labeled as *anaerobic*. To quote Wasserman [26] :

> *"If the number of muscle units which must contract to generate the required power exceeds the oxygen delivery and exhaust the O_2 stores, the oxygen level will drop to critical levels in each muscle unit and prevent the ATP, which is needed for the muscle contraction, from being generated at an adequate rate by the respiratory enzymes in the mitochondria. This will result in increased anaerobic glycolysis to sustain the availability of ATP. The consequence is an increased rate of lactic acid production."*

2.2 The different regimes of exercise

Seminal works of Wasserman and colleagues proposed a paradigm in which respiratory gas exchanges are used in order to characterize the individual response to exercise. In particular, they proposed the concept of *anaerobic threshold* (AT) as a tipping point in an incremental exercise in which the body increases the contribution of the anaerobic pathway to face the power output demand. This concept is based on the observation that intramuscular thresholds, such as the lactate threshold, correlate in time with a nonlinear increase in the exhaled carbon dioxide and air flow. This observation is helpful in practice since it cancels the need of blood sampling and analysis during exercise. Even though the causality between these two phenomenons is questioned nowadays, the AT is still widely used by practitioners since it is one of the best predictors of individual physical performances.

An other threshold was proposed by Monod and Scherrer in [20] under the name of *critical power*. In their study, the authors were interested in defining the amount of work a muscle can do before being exhausted and the conditions for fatigueless tasks. They defined the critical power as the maximum rate of exercise that can be sustained for long periods of time without

fatigue. This threshold is interesting because any exercise above of it will inevitably imply that the physiological limits of the individual are reached after some time.

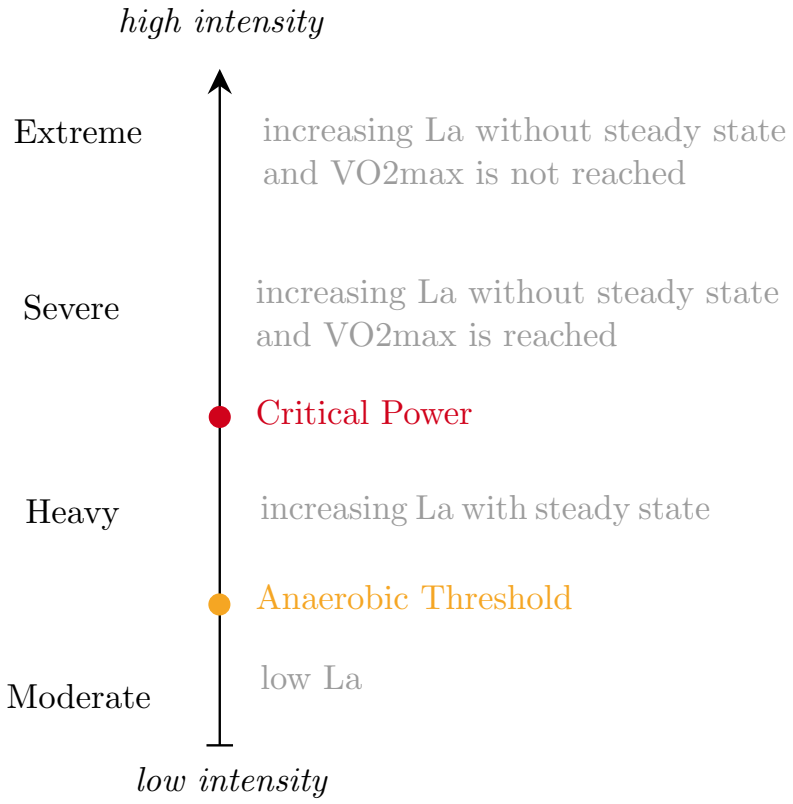

Figure 2.9: Exercise intensity domains

The two previous thresholds, the anaerobic threshold (AT) and the critical power (CP), can be used to partition the exercise intensity domain as explained in [19, 22]. Theses domains are coined as *moderate, heavy, severe* and *extreme*, ranging from the lowest intensity to the highest. Theses domains are depicted in Fig. 2.9, inspired from [21]. They are defined such that each of them triggers a different physiological reaction :

- The moderate domain corresponds to the region below the anaerobic threshold (AT). Hence, the lactate clearance mechanism are regulating the lactate (La) around its nominal values. Respiratory gas exchanges reach a steady state. The exercise is comfortable.
- The heavy domain corresponds to the region above the AT and below the critical power (CP). In this region, the lactate concentration starts rising but eventually reaches a steady state.
- The severe domain corresponds to the region at which the exercise ends because of exhaustion, which can happen before or soon after reaching VO_{2max}. In this region, the lactate concentration increases continually.

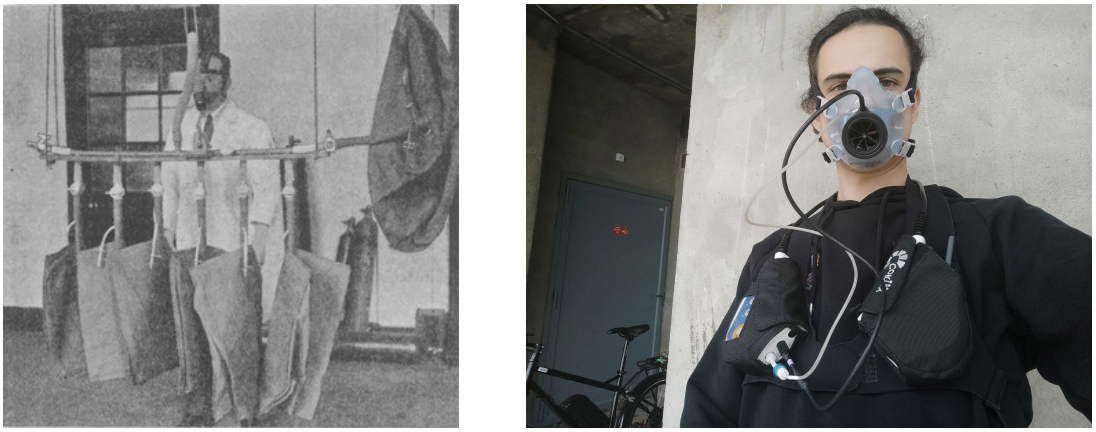

(a) (b)

Figure 2.10: (a) Picture of the Douglas bags method, (b) picture of the Metamax 3B portative gas exchange analyzer.

- Finally, in the extreme domain, the exercise intensity is so high that VO_{2max} can not be reached before exhaustion.

For an overview of the different methods aiming at defining exercise intensity regions, the reader is referred to the following review work by Jamnick and colleagues [16].

2.3 The study of gas exchange during exercise

Because monitoring physiological reactions happening at the muscular cell level is extremely difficult and invasive, exercise physiologists have developed tools to study exercise on a macroscopic level. One of these tools is the study of respiratory gas exchange and was initially suggested by Hill and colleagues, after noting a correlation between the intensity of the exercise and the consumption of oxygen.

2.3.1 Ergospirometry, the measurement of gas exchanges

The measurement of respiratory gas exchange is called *spirometry* and is used as a proxy to gather live information about physiological phenomenons happening in the body. Quantities such as the air flow of gas exhaled VE (in L/min), the flow of oxygen consumed in VO_2 (L/min) or the flow of carbon dioxide produced VCO_2 (in L/min) are of particular interest.

In the early 1900s, these quantities were estimated by closed-circuit spirometer using impermeable canvas bags, like in the Douglas bags method (2.10a). The bags were filled with the exhaled gases and their content was analyzed after the exercise by emptying them. Open circuit methods were then developed, like the portable respirometer of Nathan Zuntz, used for high altitude studies.

Later, in the 1970s, the first online measurements appeared thanks to the progress in microelectronics and sensor technology, like the Cosmed K2 for example. However only a measurement of VO_2 was available at that time.

In the middle of the 1990s, VCO_2 was measured using infra-red CO_2 sensors, like with the Cosmed K4. With both VO_2 and VCO_2 measured, online studies of the respiratory exchange ratio (RER) became possible.

Finally, in the 2000s, breath-by-breath (BxB) measurement became possible based on comparisons between the gas mixture of the air inhaled and exhaled, as well as the airflow. The spirometer Metamax 3B (2.10b) is based on such technology.

2.3.2 Modelling gas exchange during exercise

In order to understand the processes ensuring the oxygenation of the muscles and the removal of wastes during exercise, physiologists have tried to describe the evolution of gas exchange along time, also called *gas exchange kinetics*. They designed various tests, collected experimental data from different groups, in order to investigate the nature of gas exchange kinetics and the links existing with intra-body reactions. They mostly focused their effort in describing the kinetics of oxygen consumption VO_2 and the carbon dioxide production VCO_2 during effort. A brief summary of their results is given in the following sections.

2.3.2.1 VO_2 during exercise : a linear description with nonlinear limitations

After noting the correlation between the intensity of the exercise and the oxygen consumption, a natural assumption to describe VO_2 kinetics was to consider first order dynamics. For example, in [13], it was formulated that for a constant work rate the consumption of oxygen during effort could be described using two constant parameters a_0 and k and take the following exponential form :

$$VO_2(t) = a_0(1 - e^{-kt}) \tag{2.8}$$

Here, a_0 is the static gain of the exponential response, and k its time constant. In their paper, it was expected that these two quantities are independent of the work rate, at least for moderate intensities, where only the aerobic metabolism is active. Based on experimental data, they showed that these parameters can however show inter-individual variability. Other studies formulated similar conclusions, for example [5].

The same authors proposed a new approach in [14]. There, an additional, slower, exponential component parameterized by a_2 and k_2 was used to model the VO_2 kinetics :

$$VO_2(t) = a_1(1 - e^{-k_1 t}) + a_2(1 - e^{-k_2 t}) \tag{2.9}$$

From experimental data, they noted that the first fast component was the most significant, but that during more intense workout the second term, the *slow component*, became present too. They interpreted this as a relation between the slow component and the lactate clearance mechanisms. This result was latter confirmed in [2, 4, 8, 28].

Then, the existence of a VO_2 slow component grew in credibility and studies describing its behaviour and proposing physiological justifications were published. In [10], it was proposed that the apparition of the slow component depends on the exercise intensity. Authors made a distinction between exercise performed below the lactate threshold (LT) and where VO_2 reaches a steady state quickly following a mono-exponential response ; and exercise performed above the (LT) where the VO_2 steady state is delayed by a slower component. The response time of the VO_2 could be greatly increased, from the average 3 minutes below CP to up to 15 minutes above CP. In [25], different justifications for this intensity dependence were investigated. One of them was the temperature : it was hypothesized that the slow component was caused by an increased body temperature. This was then proved wrong by [18] were exercising muscles were artificially heated during exercise without significant increase in VO_2. Finally, in [23], it was shown that the type of muscle fiber used had an effect. Indeed, the use of fast-twitch fibers, whose efficiency is lower, during high intensity exercise, would generate an additional oxygen consumption.

In order to add some degree of complexity to the VO_2 kinetics model, the use of delays was also explored. For example, in [7], delays were proposed for both the fast and the slow components :

$$VO_2(t) = A(1 - e^{(-t-T_D)/\tau}) \tag{2.10}$$

$$VO_2(t) = A_1(1 - e^{(-t-T_D)/\tau_1}) + A_2(1 - e^{(-t-T_D)/\tau_2}) \tag{2.11}$$

With A, A_1, A_2 the static gains, τ, τ_1, τ_2 the time constants and T_D the delay. This delay is motivated by the mechanical delays present all along the oxygen transport chain, from the lungs to the muscles. By designing step exercise sessions with rest to exercise and exercise to exercise transitions, Hughson and Morissey showed that this delay, or the time response in general, of VO_2 kinetics could depend on the exercise intensity the individual is starting from [15]. They found that VO_2 was reaching steady state quicker after a step from prior exercise, which was confirmed later in [12].

2.3.2.2 The 2-phased nonlinear carbon dioxide production

As described in [27], the VCO_2 kinetics exhibit a 2-phased behaviour. First, in the moderate exercise domain, VCO_2 increases mono-exponentially until it reaches its steady state and is linearly related to VO_2. However, beyond the anaerobic threshold (AT), its behaviour changes. Indeed, after crossing the lactate threshold (LT), the rate of production of lactates becomes higher than the rate at which it is metabolized by bicarbonate $HCO3^-$ in the blood, which translates in a excess of carbon dioxide in the lungs. Furthermore, beyond the LT, the VO_2 slow component appears, implying an additional oxygen consumption and carbon dioxide production.

Thus, the behaviour of VCO_2 kinetics depends on the AT. Using this property, Beaver, Wasserman, Ward and colleagues proposed a method to determine the AT from gas exchange measurements [3]. This method is called the *V-slope method*. In order to identify the AT, an exercising individual performs an incremental cycling test, in which the load increases of a fixed amount, after a fixed period of time (usually 15 Watts every minutes) until exhaustion. During this exercise session, gas exchange is monitored, VO_2 and VCO_2 in particular. The AT is then identified, by computing the intersection of two tangent curves in the $VO_2 - VCO_2$ plane, one computed before the AT and one after. Thus, the AT can be expressed in the same units as VO_2, or converted to a mechanical power as shown in (2.11). This method has the advantage of estimating the AT in a non-invasive manner compared to the traditional blood sampling and analysis, and it thus vastly employed.

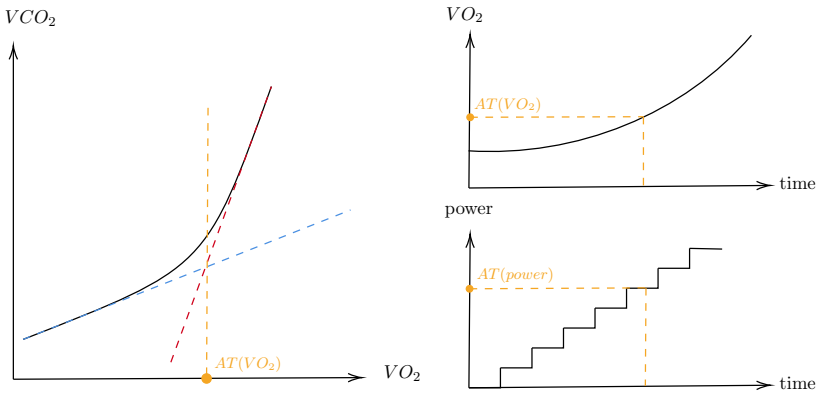

Figure 2.11: Determination of the anaerobic threshold (AT) using the V-slope method. On the left, the AT is identified at the intersection of two tangeant curves, the blue one for the low intensity region of exercise and the red one for the high intensity region of exercise. At the AT, the proportionality between VO_2 and VCO_2 changes. The AT is expressed in terms of VO_2 or in term of power output by associating the identified $AT(VO_2)$ with the power produced during the incremental exercise test.

2.3.3 Indirect calorimetry

Calorimetry is the study of energy exchanges along time. In terms of exercise physiology this corresponds to the calories burnt during a workout session. Initially the main motivations were to maximize human productivity and reduce the energy cost required to perform specific tasks. The first method used to estimate this quantity is called *direct calorimetry*, and requires the studied individual to be kept inside an insulated room (similar to a chemical calorimeter) during the whole duration of the exercise. The second method is the *indirect calorimetry* and is based on the measurement of respiratory gas exchanges. The latter is easier to implement and can be performed on a mobile subject. The substrates being oxidized at the cellular level are inferred from measurements of VO_2 and VCO_2 and the corresponding energy is computed. For example, formulas are known to estimate the carbohydrates and lipid oxidation as presented in [6] :

$$Carbohydrates\ Oxydation\ (mg/min) = 4.585\ VCO_2 - 3.2255\ VO_2 \tag{2.12}$$

$$Lipid\ Oxydation\ (mg/min) = -1.7012\ VCO_2 + 1.6946\ VO_2 \tag{2.13}$$

2.4 Substrates, the body energy resources

During exercise, two main substrates are used to fuel the muscles : glucose and fatty acids. Both these molecules can be stored in organs, or in the blood. For example, glucose is stored in the blood plasma or in the muscles and the liver under the form of glycogen. Similarly, fatty acids are stored in the blood plasma or in the muscles under the form of triglyceride. Depending on the *intensity* and *duration* of the effort, the contribution of each substrates can vary.

First, regarding the exercise *intensity* :

- at low effort intensity (around 25% of VO_{2max}), the main contribution comes from plasma fatty acids (85%) and in smaller proportions from plasma glucose and muscle triglyceride.
- at moderate effort intensity (around 65% of VO_{2max}), half of the energy comes from glucose oxidation and half from fatty acids oxidation (with equal contributions of plasma fatty acids and muscle triglyceride).
- at high effort intensity (around 85% of VO_{2max}), the rate of oxidation of fatty acids becomes insufficient and glucose is used as the main energy source (65%).

The potential energy of fatty acids is higher than the one of glucose, however, because its rate of oxidation is limited, when the effort intensity increased the glucose pathway is used to compensate.

Then, even when the effort intensity is constant, *duration* has an impact as pathways change over time :

- at low effort intensity (around 25% of VO_{2max}), the oxidation of plasma fatty acid is sufficient to ensure energy production and can be used for hours.

- at moderate effort intensity (around 65% of VO_{2max}), fatty acids and glucose are overall used in the same proportion all along the exercise. However, as muscle stocks of triglyceride and glycogen run lower, the plasma fatty acids and plasma glucose contributions increase.

During rest, the stocks of glycogen are replenished after eating carbohydrates and the stores of fatty acids after eating lipids.

The nature of the substrate oxidized during exercise can be determined using indirect calorimetry. This technique is based on the measurement of gas exchange during effort. In particular, the respiratory exchange ratio (RER) computed by dividing the volume flow of carbon dioxide exhaled by the volume flow of oxygen inhaled (both expressed in L/min). The RER varies depending on the kind of substrate oxidized, for exemple, it is close to 1 when carbohydrates are used and close to 0.7 when fatty acids are used. For detailed explanations on this subject, the reader is referred to [9, 11].

2.5 The cardiovascular and respiratory systems

The cardiovascular system is constituted of the heart and the network of blood vessels. Its function is to ensure the blood flow to the organs and muscles in order to bring the necessary substrates and oxygen and remove the wastes. Additional functions are also to regulate the hormones level and the body temperature. The blood vessels network is constituted of elements of different size, ranging from the smallest, the capillaries, to the biggest, the arteries. The heart behaves like a pump that regulates the blood flow and pressure. The heart rate of contraction, expressed in beats/min, increases during exercise. The regulation of the heart rate is performed by the autonomic nervous system via the action of the *sympathetic nervous system* (SNS) and the *parasympathetic nervous system* (PNS). The sympathetic nervous system can increase the heart rate by releasing hormones like epinephrine. The parasympathetic nervous system can decrease the heart rate by releasing hormones like acetylcholine. The heart rate is also affected by exterior factors like the sleep level, caffeine or respiration.

The respiratory system is constituted of the lungs, nose, mouth and trachea. It is an interface between the atmosphere and the body and it ensures the exchange of gas through ventilation. The lungs contain capillaries and dedicated cells called alveoli which purpose is to extract the carbon dioxide from the blood to the inside of the lungs and to increase the oxygen concentration of the blood. Thus, blood rich in carbon dioxide enters the right atrium of the heart, is pumped to the lungs, and comes back to the left atrium of the heart, rich in oxygen, ready to fuel to body.

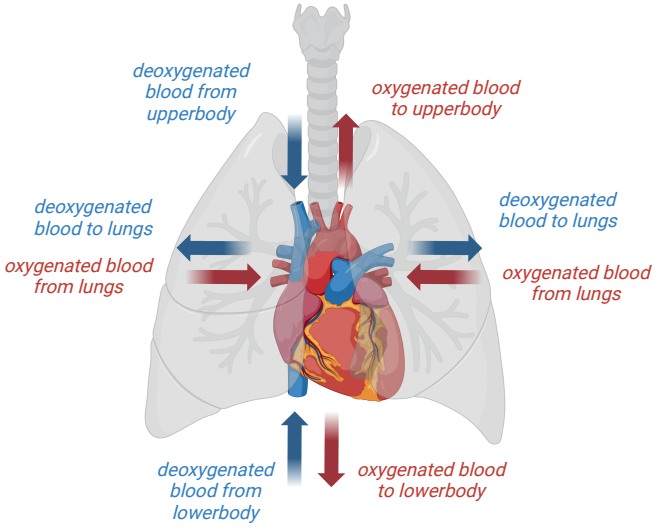

Figure 2.12: Diagram of the blood flow between the heart and the lungs.

2.6 Muscle structure and use during exercise

Body movement is ensured by the contraction of skeletal muscles. This contraction is triggered by an electrical current coming from the motor nerves and motoneurons, and implies a rotation of the bones around the joints. Muscles constitute around 40% of the total mass of the body. They are constituted of cylindrical muscle cells called *myofibrils* formed by fibers called *myofilaments*. These cells are fueled by capilaries, bringing oxygen and substrates and removing wastes.

Muscles fibers belong to three different types depending on their mechanical properties and the metabolic pathway used :

1. The type I fibers, or slow oxidative (SO) fibers - these fibers are powered by aerobic oxidation and are used for endurance exercise like running, swimming or cycling.

2. The type IIa fibers, or fast twitch oxydative-glycolytic (FOG) fibers - these fibers are powered both by aerobic oxidation and anaerobic glycolysis and are used for power exercise like weight lifting, sprinting or jumping.

3. The type IIb fibers, or fast twitch glycolytic (FG) fibers - these fibers are similar to the IIa fibers but are solely powered by anaerobic glycolysis.

The distribution of these muscles fibers depends on each muscle. For example, the biceps (in the arm) is constituted of around 50% of type I fibers, the soleus (in the leg) of around 80% of type I fibers and the orbicularis oculi (in the eye) of around 15% of type I fibers. The

distribution also depends on the physical activity. For example, the total skeletal muscle mass of sedentary individuals is constituted of around 50% of type I fibers and 50% of type II fibers but endurance runners will develop their type I muscle mass while sprinter will develop their type II muscle mass.

2.7 Training and benefits

2.7.1 The consequences of physical activity

A regular physical activity has beneficial effects on health. In fact, the world health organization (WHO) recommends at least two and a half hours of exercise per week for adults.

A regular physical activity triggers physiological modifications :

- endurance training at low to moderate intensities for long durations (from 20 min to hours) improves health and performances as it increases the aerobic capacity (VO_{2max}). This can be explained by a increased number of alveoli in the lungs, an increase in number and in size of mitochondria and an increased size of the heart. In addition, it reduces blood pressure, and increase the rate of clearance of lactate.
- strength training increases the stocks of phosphocreatine PCr in the muscles, thus extending the action of the phosphagen pathway.
- high intensity interval training increases the rate of production of ATP by the glycolytic pathway.

For more information on this subject the reader is referred to [24].

2.7.2 Physical exercise for rehabilitation

Because of the benefits that exercise yields, it is used by physicians in rehabilitation programs in order to treat chronic diseases such as diabetes, chronic obstructive pulmonary disease (COPD) or cancer.

Because the patients benefit from exercise but their physical conditions is weakened due to their disease, the exercise sessions are performed with care. Indeed, they often happen at the hospital, supervised by health practitioners. The exercise sessions are monitored by recording respiratory gas exchange variables, blood pressure or electrocardiogram (ECG) signals. Also, the exercise sessions are tailored to the individual. For example the Borg rating of perceived exhaustion (RPE) can be used. This scale associates a number to the exercise level from 0, for no exhaustion, to 20 for maximal exhaustion. The exercise intensity can also be chosen as a multiple of the basal metabolic rate using the metabolic equivalent of task (MET) or fractions of the maximal aerobic capacity of the individual VO_{2max}.

2.8 Conclusion

In this chapter an overview of the physiological concepts involved in the understanding of the exercise is given.

First, the complexity of the energy production process at a microscopic level is showed. This process is ensured by a complex set of chemical reactions, using different substrates, producing energy and waste with different efficiencies. Two main pathways are used to simply describe the energy production process : the *aerobic* pathway, fueled by oxygen O_2, efficient but slow to activate ; and the *anaerobic* pathway, quick to activate in absence of O_2 but less efficient and not durable due to the wastes it produces and the depletion of substrates stocks.

Then, the proxy strategies used by the physiologist to study exercise at a macroscopic level are described. These strategies are based on live measurement of respiratory gas exchanges called *spirometry*. As part of these strategies, physiologists use measurements of the oxygen consumption VO_2 and the carbon dioxide production VCO_2 in order to derive information of the physiological stress undergone by the body, on the exercise capacity of individuals or on the resources used by the body. To understand VO_2 and VCO_2, models describing their evolution during exercise were proposed by physiologists. These models showed that even though both these variables can be fairly accurately described by simple mono-exponential models for low intensity of effort, they fail in describing complex behaviours like the slow oxygen component or the anaerobic threshold, which calls for more complex model structures.

Bibliography

[1] Cengiz Akalan, Len Kravitz, and Robert R Robergs.
Vo2max: Essentials of the most widely used test in exercise physiology.
ACSM's Health & Fitness Journal, 8(3):5–9, 2004.

[2] Thomas J Barstow and Paul A Molé.
Linear and nonlinear characteristics of oxygen uptake kinetics during heavy exercise.
Journal of Applied Physiology, 71(6):2099–2106, 1991.

[3] William L Beaver, KARLMAN Wasserman, and Brian J Whipp.
A new method for detecting anaerobic threshold by gas exchange.
Journal of applied physiology, 60(6):2020–2027, 1986.

[4] Christopher Bell, Donald H Paterson, John M Kowalchuk, Javier Padilla, and David A Cunningham.
A comparison of modelling techniques used to characterise oxygen uptake kinetics during the on-transient of exercise.
Experimental physiology, 86(5):667–676, 2001.

[5] William E Berg.
Individual differences in respiratory gas exchange during recovery from moderate exercise.
American Journal of Physiology-Legacy Content, 149(3):597–610, 1947.

[6] Jean-Frederic Brun, Emmanuelle Varlet-Marie, Ahmed Jerome, and Jacques Mercier.
Measurement and physiological relevance of the maximal lipid oxidation rate during exercise (LIPOXmax).
In *An International Perspective on Topics in Sports Medicine and Sports Injury*. InTech, February 2012.

[7] R. Casaburi, T. J. Barstow, T. Robinson, and K. Wasserman.
Influence of work rate on ventilatory and gas exchange kinetics.
Journal of Applied Physiology, 67(2):547–555, August 1989.

[8] Cain CT Clark and Stephen B Draper.

A detailed comparison of oxygen uptake kinetics at a range of exercise intensities.
Motriz: Revista de Educação Física, 25, 2019.

[9] Edward F Coyle.
Substrate utilization during exercise in active people.
The American journal of clinical nutrition, 61(4):968S–979S, 1995.

[10] Carrie Ferguson, Harry B Rossiter, Brian James Whipp, Andrew J Cathcart, Scott R Murgatroyd, and Susan A Ward.
Effect of recovery duration from prior exhaustive exercise on the parameters of the power-duration relationship.
Journal of applied physiology, 108(4):866–874, 2010.

[11] KN Frayn.
Calculation of substrate oxidation rates in vivo from gaseous exchange.
Journal of applied physiology, 55(2):628–634, 1983.

[12] ANTHONY Gerbino, SUSAN A Ward, and BRIAN J Whipp.
Effects of prior exercise on pulmonary gas-exchange kinetics during high-intensity exercise in humans.
Journal of Applied Physiology, 80(1):99–107, 1996.

[13] Franklin M Henry.
Aerobic oxygen consumption and alactic debt in muscular work.
Journal of Applied Physiology, 3(7):427–438, 1951.

[14] Franklin M Henry and Janice C DeMoor.
Lactic and alactic oxygen consumption in moderate exercise of graded intensity.
Journal of Applied Physiology, 8(6):608–614, 1956.

[15] R. L. Hughson and M. Morrissey.
Delayed kinetics of respiratory gas exchange in the transition from prior exercise.
Journal of Applied Physiology, 52(4):921–929, April 1982.

[16] Nicholas A Jamnick, Robert W Pettitt, Cesare Granata, David B Pyne, and David J Bishop.
An examination and critique of current methods to determine exercise intensity.
Sports Medicine, 50(10):1729–1756, 2020.

[17] Norman L Jones and Kieran J Killian.
Exercise limitation in health and disease.
New England Journal of Medicine, 343(9):632–641, 2000.

[18] Shunsaku Koga, Tomoyuki Shiojiri, Narihiko Kondo, and Thomas J Barstow.
Effect of increased muscle temperature on oxygen uptake kinetics during exercise.
Journal of Applied Physiology, 83(4):1333–1338, 1997.

[19] KE Lansley, FJ Dimenna, SJ Bailey, and AM Jones.
A 'new'method to normalise exercise intensity.
International journal of sports medicine, 32(07):535–541, 2011.

[20] H Monod and J Scherrer.
The work capacity of a synergic muscular group.
Ergonomics, 8(3):329–338, 1965.

[21] David C Poole and Andrew M Jones.
Oxygen uptake kinetics.
Compr Physiol, 2(2):933–96, 2012.

[22] David C Poole, Casey A Kindig, Brad J Behnke, and Andrew M Jones.
Oxygen uptake (vo2) kinetics in different species: a brief review.
Equine and comparative exercise physiology, 2(1):1–15, 2005.

[23] DAVID C Poole, WALTER Schaffartzik, DOUGLAS R Knight, TONI Derion, BRIAN Kennedy, HAROLD J Guy, RENATO Prediletto, and PETER D Wagner.
Contribution of excising legs to the slow component of oxygen uptake kinetics in humans.
Journal of applied physiology, 71(4):1245–1260, 1991.

[24] Mária Rendi, Attila Szabo, Tamás Szabó, Attila Velenczei, and Árpád Kovács.
Acute psychological benefits of aerobic exercise: A field study into the effects of exercise characteristics.
Psychology, Health & Medicine, 13(2):180–184, 2008.

[25] Ronald Terjung, editor.
Comprehensive Physiology.
Wiley, 1 edition, January 2011.

[26] K Wasserman, B J Whipp, S N Koyl, and W L Beaver.
Anaerobic threshold and respiratory gas exchange during exercise.
Journal of Applied Physiology, 35(2):236–243, August 1973.

[27] Brian J. Whipp.
Physiological mechanisms dissociating pulmonary CO $_2$ and O $_2$ exchange dynamics during exercise in humans: Pulmonary gas exchange dynamics in exercise.
Experimental Physiology, 92(2):347–355, March 2007.

[28] BRIAN J Whipp and KARLMAN Wasserman.
Oxygen uptake kinetics for various intensities of constant-load work.
Journal of applied physiology, 33(3):351–356, 1972.

Chapter 3

Modeling the Exercising Cyclist

Contents

In the previous chapter, attempts to use mathematical modelling to describe the adaptation of the human body to exercise are presented. The models presented come from the *exercise physiology research community* and have for goal to describe as best as possible the evolution of respiratory gas exchange and heart rate during exercise. In this chapter, propositions coming from *the control research community* to describe the same phenomenons are presented. Then, the formulation, identification and validation of the respiratory gas exchange model used in this thesis is presented. A novel bio-mechanical model to describe the interaction between the cycling force and cycling velocity is proposed and validated using experimental data. Finally, both the respiratory gas exchange model and the bio-mechanical models are used in a new simulation strategy aiming at generating realistic cyclist behaviours in simulation.

3.1 Control systems theory applied to physiological modelling

Control systems is the science aiming at manipulating physical quantities by operating actuators in an automated fashion. In order to do so, models describing the input-output relationships ruling the behaviour of the considered system are derived. More precisely, the "behaviour" of a system is the dynamic evolution of quantities called *states* under the action of the actuators and possibly external disturbances. The concept of system is extremely generic, and virtually any process exhibiting input-output relationships can qualify, like vehicles, chemical reactors, thermostats, robots, etc.

To implement automated control strategies, control scientists first try to propose a rigid mathematical description of the considered system : a *model*. Under close examination, every system is unique but share similar properties with others. Thus, the control system theory is very rich of the families of mathematical models that can be used in order to describe the physical world, which makes it very adaptable and powerful.

As described in Subsection 2.3.2, the entire human body, but more specifically the cardio-vascular and respiratory systems, vary under the influence of work rate during exercise. In particular, it was shown that the evolution in time of the oxygen consumption or the carbon dioxide production can be described to a certain extent using mathematical relationships. This is the starting point of a successful modelling investigation which is why researchers from the control system community attempted to propose accurate models of the evolution of physiological quantities during exercise. In the next sections, models proposed to describe the evolution the heart rate (HR) and the respiratory gas exchange (RGE) are presented.

3.1.1 Physiology and control : two different philosophies of modelling

One main difference that can be noted between the modelling approaches proposed by physiologists and control scientists is that while the models proposed by physiologists focus on the *description* of the evolution of physiological signals, control scientists focus on the *robustness* of

their models, particularly their ability to *predict* future data from independent data-set of the one used for the identification.

Also, physiologists pay attention to justify the structure of their model based on literature and theory. This is not necessary true for the control community where usually the quality of a model is evaluated based on its ability to achieve "good" performances, in terms of control of the variable of interest or of the prediction of the modelled quantities. Thus, a performing control model can be purely mathematical, while it is not so likely for physiology models.

> *"Black box models like Hammerstein-Wiener models do not offer the same understanding as physiological models have, but they bring other advantages. Detached from physiological evidence they are more flexible and can adjust better to data and therefore, may deliver better fitting results."* [6]

3.1.2 Heart rate models

Various approaches have been proposed by the control community to model the evolution of heart rate during exercise. They differ by the mathematical *structure* used to describe the phenomenon, by the *input/output* relationships chosen and by the *type of physical activity* described. A non-exhaustive review of these approaches in proposed in the following. For a comparative review of analytical models and machine learning models, the reader is referred to [25] and [24].

Cheng and colleagues in [11] focused on characterizing the evolution of heart rate during treadmill exercises. The model they proposed is nonlinear, expressed in continuous time, and relates the heart rate with the speed of the treadmill in the following way :

$$\dot{x}_1(t) = -a_1 x_1(t) + a_2 x_2(t) + a_2 u^2(t) \tag{3.1}$$

$$\dot{x}_2(t) = -a_3 x_2(t) + \Phi(z(t)) \tag{3.2}$$

$$z(t) = x_1(t) \tag{3.3}$$

$$\Phi(z(t)) = \frac{a_4 x_1(t)}{1 + exp(-(x_1(t) - a_5))} \tag{3.4}$$

with a_1, a_2, a_3, a_4 and a_5 positive scalars, x_1 the HR component related to the central response to exercise (i.e. the action of the sympathetic and parasympathetic neural responses) and x_2 the slower and peripheral effects (such as the increase in body temperature, hyperventilation or loss of body fluids). The input u is the speed of the treadmill. This model was used to design control strategies to pilot the HR during treadmill exercises.

For rhythmic exercises like walking, cycling and rowing, Baig and colleagues proposed a model relating the exercise rate (in Hertz) to the heart rate (in beats per minutes) in [7]. The main motivation of choosing the exercise rate as input is that it does not depend on the type of physical activity performed. In their study they first showed the limits of a linear time invariant (LTI) description of the phenomenon and then opted for a linear time varying (LTV) approach. The model they proposed is the following :

$$\begin{aligned} y(t) = a_1(t)y(t-1) + a_2(t)y(t-2) + ... + a_p(t)y(t-p) \\ + b_1(t)u(t-1) + b_2(t)u(t-2) + ... + b_p(t)u(t-p) \end{aligned} \tag{3.5}$$

The parameters of the model $a_1(t), ..., a_p(t)$ and $b_1(t), ..., b_p(t)$ are time-varying and are estimated online using a Kalman Filter (KF). In their study, the order of the model p was chosen equal to 2.

The choice of a second order model with time varying coefficients to describe HR was later confirmed in [20]. This paper is a comparative study of the performances of LTI, LTV, first order and second order models to describe the evolution of HR during running exercises. It showed that HR was best described by second order LTV dynamic equations. Authors considered two inputs for their models, the power output (in Watts) and the slope of the road (in degrees). The different model structures are the following :

$$y_k = -a_1 y_{k-1} + b_0 u_{k-\delta} \tag{3.6}$$

$$y_k = -a_1 y_{k-1} - a_2 y_{k-2} + b_0 u_{k-\delta} + b_1 u_{k-\delta-1} \tag{3.7}$$

$$y_k = -a_1 y_{k-1} + b_{1,0} u_{1,k-\delta 1} + b_{2,0} u_{2,k-\delta 2} \tag{3.8}$$

$$y_k = -a_1 y_{k-1} - a_2 y_{k-2} + b_{1,0} u_{1,k-\delta 1} + b_{1,1} u_{1,k-\delta 1-1} + b_{2,0} u_{2,k-\delta 2} + b_{2,1} u_{2,k-\delta 2-1} \tag{3.9}$$

with y the measured heart rate, u_1 the measured power output and u_2 the road gradient. Scalars $\delta 1$ and $\delta 2$ are time delays for both the inputs. Coefficients a_i and $b_{i,j}$ could either be time invariant or time variant.

A nonlinear model relating the evolution of HR to the power output (in Watts) and the rate of exercise (in Hertz) during cycling was proposed in [26]. It is defined as follows :

$$\dot{r} = A(r - r_0)^{\alpha}(r_x - r)^{\beta}(D - r)^{\gamma} \tag{3.10}$$

$$\dot{D} = B(f(p, w) - D)^{\kappa} \tag{3.11}$$

$$f(p, w) = c_0 + c_1 p + c_2 \omega + c_3 p^2 + c_4 \omega^2 + c_5 p\omega \tag{3.12}$$

with r the heart rate and $\dot{r}$ its time derivative, $A, B, \alpha, \beta, \gamma, \kappa, c_0, c_1, c_2, c_3, c_4, c_5$ are constant parameters, r_0 and r_x correspond to the basal and maximal HR respectively. The term D represents the heart rate demand, associated with the exercise intensity, and $\dot{D}$ its time derivative. The input p corresponds to the power output (in Watts) and ω to the exercise rate (in Hertz).

3.1.3 Gas exchange models

On the same line, different approaches have been explored in order to model the evolution of respiratory gas exchange during exercise. In the next sections, an overview of these methods is given. First, gas exchange models for simulation are presented. Then, parametric and non parametric analytical models are presented. Finally, approaches based on machine learning and wearable sensors are presented.

3.1.3.1 Simulation models

Simulation models are dynamic models which consist in the direct translation of the physical laws describing a system (like mass conservation, fluid transport, etc). For respiratory gas exchange, a simulation model was developed as a PhD work by Thamrin [36] in 2008.

In this work, the entire respiratory control system during exercise is modeled. The model is constituted of different compartments : the lungs, the brain, the muscle and the tissues departments. This structure allows for a deep level of detail regarding each element. For example, in the muscle compartment, the acidosis phenomenon is taken into account with the accumulation of lactate in the muscle, allowing to take into account the influence of exercise intensity on the respiratory system.

Because the focus of this model is essentially descriptive, it is possible to include physiological variables which would not be taken into account in a control oriented model (like the partial pressure of oxygen in the blood Pa_{O_2}). It is also possible to make hypotheses regarding the implicit feedback strategies happening in the body in order to regulate respiratory gas exchanges.

One advantage of such model is to carry on theoretical investigation regarding the influence of specific parameters on the closed loop respiratory gas exchange system. For example, investigating the influence of an increased inspired fraction of carbon dioxide on the transient and steady state values of ventilation, and their adequacy with similar experimental results.

However, even if this high level of complexity is essential for such “sand-box” model, it makes it impossible to be used in practical situations for estimation and/or control, contrarily to the models presented in the following sections.

3.1.3.2 Parametric analytical models

First, the parametric analytical models are presented. These models have in common that they are defined by a rigid, predefined structure, parameterized by coefficients which value is determined as part of one or multiple optimization problems. The optimization is solved in order to minimize a cost function depending in most cases on the prediction error of the model. The choice of their structure is usually informed by theory and practical considerations in order to take into account known linear or nonlinear behaviours for example. These models are designed for a specific goal, which can be the estimation of respiratory gas exchange, their control during exercise, or both.

A common approach to design parametric analytical models of respiratory gas exchange is the use of Hammerstein-Wiener models. This structure allows to separate the linear and nonlinear parts of a system. Common subcases of Hammerstein-Wiener models are the Hammerstein models, which are constituted of a nonlinear input affecting linear dynamics, and Wiener models which are linear dynamics whose output depends nonlinearly on the states as depicted in Figure 3.1.

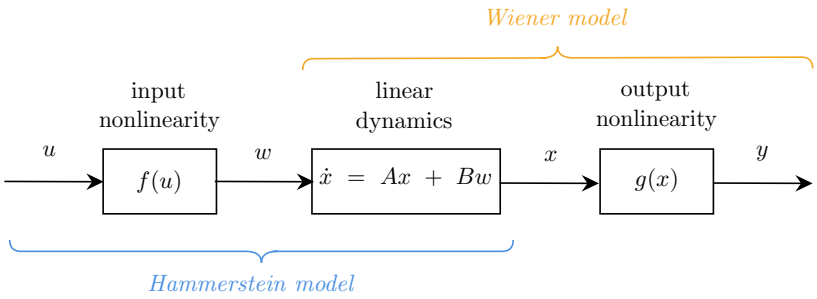

Figure 3.1: Hammerstein-Wiener models.

In the case of respiratory gas exchange during exercise, such structure is interesting for multiple reasons. As showed in Section (2.3.2), the mono-exponential behaviour of VO_2 and VCO_2 in the moderate intensity region can be described by *linear dynamics*, nonlinearities such as the anaerobic threshold can be described by an *output nonlinearity* and the dependency of VO_2 and VCO_2 to the effort intensity can be described by an *input nonlinearity*.

Initially investigated by Su and colleagues in 2007, the Hammerstein model structure was proposed to describe the evolution of VO_2 during treadmill exercises [35]. The authors considered the speed v of the treadmill (in m/sec) as the input of their model. They split the identification process in two phases. First, the linear component of the model was identified using linear regression and experimental data of VO_2 acquired during an exercise session. During this session, the treadmill speed profile was designed as a Pseudo Random Binary Signal (PRBS), a common excitation signal for model identification. Then, the nonlinear input component was identified using the Support Vector Regression (SVR) technique. This model was later used in order to regulate the oxygen consumption during treadmill exercises by conveniently chosing

the speed of the treadmill. In 2009, they extended this approach in order to estimate the oxygen consumption in a non-invasive way using wearable HR sensors and accelerometers using an Hammerstein model [34].

Later, in 2008, a similar approach was used by Hunt and colleagues in [17] in order to control the physiological response of an individual during robotic-assisted gait exercises on treadmills. There, they proposed a *stochastic* Hammerstein model. The stochastic component came from the choice of affecting the Hammerstein with a Poisson process in order to take into account the irregularities of the human ventilation during exercise. The authors chose a smooth gain affecting the input of the linear system to take the nonlinearties of the VO_2 response during exercise. As previously, this model was then used for control purposes.

Finally, in 2012, Baig and colleagues proposed to estimate the oxygen consumption during rhythmic exercise (like cycling and rowing) in a non-invasive fashion using a Hammerstein model [8]. To do so, they used a wearable device measuring the heart rate (HR) and the respiratory rate (RespR) as well as a separate measure of the frequency of exercise also called exercise rate (ER). They found that the input linearity depended on the type of activity performed (cycling or rowing).

An interesting approach was used by Artiga Gonzalez and colleagues in 2015 in [4] to estimate oxygen consumption during cycling exercise sessions of varying intensity. The model they proposed is closely connected to physiology theory since it uses the Critical Power (CP) as a parameter of the model in order to define the exercise regions which dictate the behaviour of the system. As part of the data acquisition process, the studied individual performed an incremental test which was also used to determine the value P_c of the CP as the exercise intensity at which the blood lactate increased substantially.

The model they proposed followed the following equations :

$$\dot{V}O_2(t) = \dot{V}O_{2base} + x_1(t) + x_2(t) \tag{3.13}$$

$$\dot{x}_1 = \tau_1^{-1}(A_1(P) - x_1) \tag{3.14}$$

$$\dot{x}_2 = \tau_2^{-1}(A_2(P) - x_2) \tag{3.15}$$

As shown in equation (3.14), the equation depends on 3 components, the constant basal oxygen consumption $\dot{V}O_{2base}$, the first *fast* dynamic oxygen component x_1 and the slow oxygen component x_2. The fast and slow oxygen components have different time constants, τ_1 and τ_2 respectively with $\tau_1 < \tau_2$. The terms A_1 and A_2 both relate to the static gain of each component, and are supposed to depend on the power output P. This dependence is structured as follows :

$$A_1(P) = min(s \cdot P, \dot{V}O_{2max} - \dot{V}O_{2base}) \tag{3.16}$$

$$A_2(P) = \begin{cases} V_\Delta \cdot exp(-(P_c - P)/\Delta) & (if \;\; P \leq P_c) \\ \dot{V}O_{2max} - \dot{V}O_{2base} - A_1(P) & (if \;\; P > P_c) \end{cases} \tag{3.17}$$

with s the constant slope of the slow component, V_Δ the maximum amplitude of the slow component, Δ the decay constant of the slow component and VO_{2max} the maximal aerobic capacity of the exercising individual.

During model validation, authors concluded that the model performed well in low intensities, but had the tendency to overestimate the slow component for high effort intensities. They supposed that the quality of the estimation could be improved by including the identification of the CP in the optimization problem itself. They also suggested that removing the slow component from the model, or at least question its additive exponential nature could lead to better results. These works led to other publications [5, 6].

The last approach to be mentioned is of Ludwig and colleagues in 2016 [23]. In their paper, they studied the use of a convolution model, with a reduced number of parameters, in order to describe the responses of VO_2, VCO_2 and HR during exercise. The model is formulated as follows :

$$y(t) = a_2 \cdot \left[\frac{1}{a_1} (u * e^{-\tau/a_1})(t) \right]^{a_4} + a_3 \tag{3.18}$$

with $(u * e^{-\tau/a_1})$ representing the discrete time convolution of lag τ, $\sum_\tau u(\tau) \cdot x(t - \tau)$ and a_1, a_2, a_3 and a_4 scalar coefficients. In their paper, they explain the link existing between this model and the traditional Hammerstein-Wiener approaches. The paper illustrates the method with an HR model and validate it using experimental data. Finally, authors claim that the accuracy of the proposed model is equivalent to other analytical approaches but has the advantage of depending on only 4 parameters.

3.1.3.3 Nonparametric analytical models

As mentioned before, the respiratory gas exchange system contains its share of nonlinearities. In a parametric identification strategy, the structure of the model has to be chosen beforehand, with a given number of parameters, which might not necessary be suitable for the considered system. This difficulty motivated the use of nonparametric identification methods to tackle the issue of finding accurate models to respiratory gas exchange during exercise.

The main difference between parametric and nonparametric approaches is that nonparametric approaches focus directly on modelling the frequency or time response of the system, for example, the finite input response (FIR). This type of methods is usually applied to nonlinear systems

and the parameters of the parametric identification are replaced by a basis of nonlinear kernel functions covering the input space of the system. The choice of the kernel's shape is a problem in itself, and many different shapes have been explored (linear, radial basis, splines). For a detailed comparison of parametric and nonparametric methods, readers are referred to [29] and references therein.

For the estimation of VO_2 during treadmill exercises Ye and colleagues developed a non-parametric approach in [39, 40]. In these papers, the finite impulse response (FIR) between the treadmill speed and the oxygen consumption is identified using stable spline kernels and radial basis kernels. They concluded that stable splines performed better, and that the proposed model was suitable for VO_2 estimation during treadmill exercises.

Also, in 2022, YU and colleagues proposed to use a nonparametric approach to model the oxygen consumption during stair exercises [41]. They compared the prediction performances of their approach to other parametric approaches.

3.1.3.4 Machine learning models

Finally, with the development of machines learning methods, neural networks have been applied to the estimation of physiological variables during exercise. These methods present several advantages. They are usually based on the measurement of easily accessible signals (like heart rate, ventilation, accelerations, etc.) which can be monitored using wearable devices and allow the estimation of gas exchange in free exercise setups (like outdoor running or cycling for example). Thanks to their flexibility, neural networks can merge input signals which would be difficult to relate in a structured fashion (like body accelerations and heart rate for example).

In Table 3.1, a brief summary of the applications of neural networks to respiratory gas exchange during exercise is given. For a comparative review of AI methods, readers are referred to [42].

3.2 Explored gas exchange model

In this thesis, estimation and control strategies are based on the respiratory gas exchange model developed during the previous PhD work of Nadia Rosero in Gipsa-lab [18]. In particular, a model was proposed to describe the evolution of both the oxygen consumption and the carbon dioxide production during cycling. In the following sections the structure of this model, the identification and the validation process are presented.

Authors	Year	Inputs	Output	Model
Fudge et al. [13]	2007	HR, 3D accelerations	VO_2	linear regressions
Altini et al. [2]	2016	3D accelerations	VO_2	linear, exponential and logistic transfer functions
Borror et al. [9]	2019	HR, $\dot{HR}$, power, cadence, body mass	VO_2	shallow neural network
Zignoli et al. [43]	2020	HR, power, cadence, respiratory frequency	VO_2	recurrent neural network
Amelard et al. [3]	2021	power, $\dot{VE}$, HR, HR variability	VO_2	temporal convolutional network

Table 3.1: Machine Learning methods in the literature

3.2.1 Structure of the model

The model proposed in [18] belongs to the family of parametric analytical models. In opposition to the vast majority of approaches that were presented so far, this model allows the estimation of both the oxygen consumption and the carbon dioxide production. It focuses on the estimation of respiratory gas exchange during cycling, but can virtually be applied to any type of exercise where the power output is easily measured or estimated. The model is formulated as follows :

$$\begin{cases} \mathbf{x}_{k+1} &= \mathbf{A}\mathbf{x}_k + \mathbf{B}u_k + \mathbf{B}w_0 \\ \mathbf{y}_k &= \mathbf{C}(\rho_k)\mathbf{x}_k \end{cases} \tag{3.19}$$

where $\mathbf{x}_k \in \mathbb{R}^3$ is the state vector at instant k given by $\mathbf{x}_k = [x_1, x_2, x_3]^T$ with $x_1 = mO_2$ the consumed mass of oxygen per unit of time (in g/min), $x_2 = mCO_2$ the *aerobically* produced mass of carbon dioxide per unit of time (in g/min) and $x_3 = \varepsilon CO_2$ stands for the *anaerobically* produced mass of carbon dioxide per unit of time or excess of CO_2 (in g/min).

The input $u_k \in \mathbb{R}$ stands for the mechanical power developed by the cyclist at the pedal level (in Watts). The symbol w_0 models an additional unknown power production (for instance, the power required for other physiological functions such as digesting, breathing, etc).

The output vector $\mathbf{y}_k \in \mathbb{R}^2$ is given by $\mathbf{y}_k = [y_1, y_2]^T$ with $y_1 = x_1$ the consumed oxygen mass per unit of time (in g/min) and $y_2 = x_2 + \rho x_3$ the total carbon dioxide mass per unit of time (in g/min) mCO_2^{tot} formed by adding the aerobic CO_2 contribution to a fraction ρ of the excess of carbon dioxide εCO_2. Matrices $\mathbf{A}$ and $\mathbf{B}$ are constant. Matrix $\mathbf{C}(\rho_k)$ depends affinely in the parameter ρ_k as follows :

$$\mathbf{C}(\rho_k) = \begin{pmatrix} 1 & 0 & 0 \\ 0 & 1 & \rho_k \end{pmatrix} \tag{3.20}$$

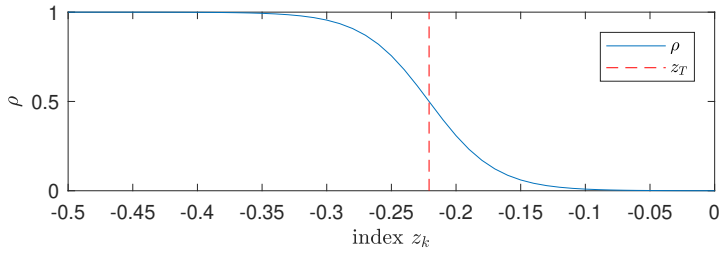

Figure 3.2: Evolution of the transition function ρ along the index z_k in blue. The index corresponding to the anaerobic threshold (AT), z_T, is represented in red. The region right of z_T is considered mostly aerobic and the region left of z_T mostly anaerobic.

The varying parameter ρ_k is the fraction of excess of carbon dioxide present in the total mass of CO_2 measured in output of the system. It is not a variable that can be directly measured in practice, thus, it is modeled as the following function of the states :

$$\begin{cases} z_k &= x_{1k} - x_{2k} - \rho_{k-1} x_{3k} \\ \rho_k &= 0.5 + 0.5 \tanh\left(\frac{z_T - z_k}{h}\right) \end{cases} \tag{3.21}$$

By definition, ρ takes its values between 0 and 1 with $\rho = 0$ corresponding to an aerobic effort and $\rho = 1$ corresponding to an anaerobic effort. The index z_k takes its values around 0 when there is a balance between mO_2 and mCO_2, corresponding to an aerobic effort. When the anaerobic threshold is crossed, the additional carbon dioxide production due to εCO_2 implies a growth of z_k in the negatives values. Here, z_T is the translation of the anaerobic threshold in the index z_k and h is a scalar modulating the rate of variation between the aerobic and the anaerobic pathways. The value of z_T is computed automatically during the identification process. The transition function is represented in Fig. 3.2.

The behaviour of the transition function is illustrated in Fig. 3.3. During an incremental exercise, the anaerobic contribution of carbon dioxide production, computed as $\rho \cdot \epsilon CO_2$, is adding up to the aerobic contribution. The maximal carbon dioxide production is reached when $\rho = 1$, in higher intensities of exercise.

The linear dynamics of the system are determined by matrices $\mathbf{A}$ and $\mathbf{B}$. These matrices are constant, and parameterized by coefficients θ_i in the following fashion :

$$\mathbf{A} = \begin{bmatrix} \theta_1 & \theta_2 & 0 \\ 0 & \theta_3 & 0 \\ 0 & \theta_5 & \theta_6 \end{bmatrix} \qquad \mathbf{B} = \begin{bmatrix} \theta_4 \\ \theta_4 \\ \theta_7 \end{bmatrix} \tag{3.22}$$

In total, the model is parameterized by 10 coefficients : $\theta_1, ..., \theta_7, w_0, z_T$ and h. These parameters depend on the individual and on the level of training and are identified using respiratory gas exchange and power output data. The identification methodology is detailed in section 3.2.3.

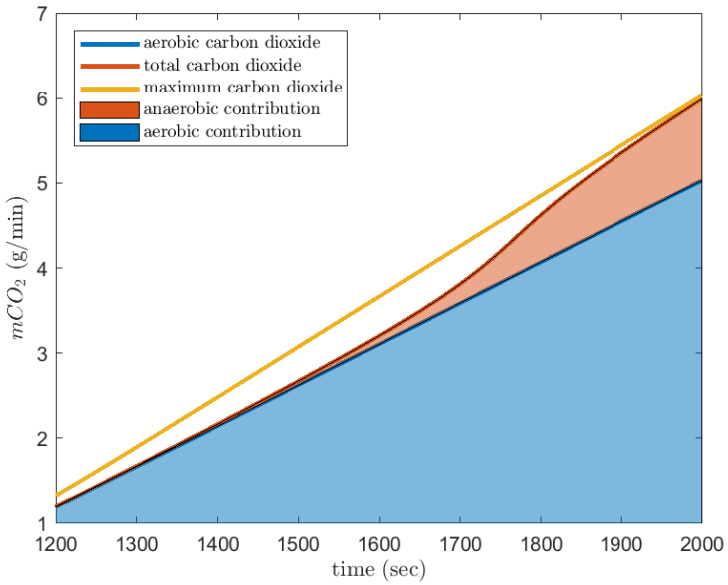

Figure 3.3: Contributions of the aerobic and anaerobic components in carbon dioxide production during a simulated incremental test. In this test, the power developed by the cyclist increases linearly with time. The aerobic contribution is mCO_2, the second state of the system (i.e. $\rho = 0$). The total carbon dioxide production mCO_{2tot} is the second output of the system. The maximum carbon dioxide production is mCO_{2tot} computed with $\rho = 1$. For low effort intensities, the total carbon dioxide production is close to the aerobic contribution. For high effort intensities, the total carbon dioxide production is close to the maximum carbon dioxide production due to the increase in the anaerobic contribution.

The structure of the model is similar to the one of a Wiener model, with linear dynamics and the output being a nonlinear map of the states. More precisely, it belongs to the class of quasi linear parameter varying system (qLPV). Linear parameter varying systems are systems with a linear structure but with matrices that depend on a varying parameter. Here, the varying parameter is ρ. Because this parameter depends on the state of the system through the variable z, the system is called quasi-LPV. This structure is interesting because it allows the use of specific techniques from robust control and estimation theory.

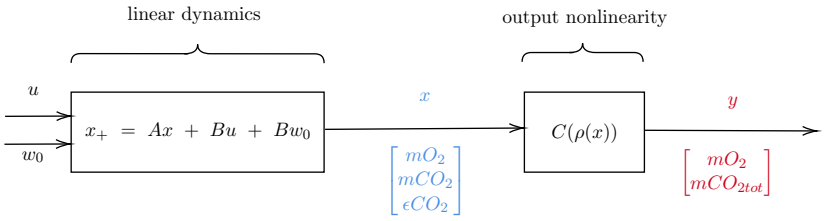

Figure 3.4: Similarities with the Wiener structure.

3.2.2 Theoretical and practical motivations

The formulation of the previous model is based on several assumptions :

- The influence of the oxygen slow component is neglected here. The dynamics of mO_2 are supposed to be purely linear.
- The influence of exercise intensity is taken into account via the distinction between the aerobic and anaerobic carbon dioxide production.
- A smooth transition between the aerobic and anaerobic modes is modeled by the continuous function ρ.
- The basal metabolic rate is supposed to be constant and modeled by w_0.
- The states of the system are expressed in *mass*. In the following, the density of dioxygen and carbon dioxide at 20°C and normal pressure conditions are supposed equal to $\delta_1 = 1.429\,(kg/m^3)$ and $\delta_2 = 1.842\,(kg/m^3)$ respectively. This way, the dependency of respiratory gas exchange to temperature and pressure conditions can be taken into account.
- The model is expressed in discrete time in order to ease its implementation on micro-controllers. It is identified at a constant sampling time $Te = 1\ sec$.

3.2.3 Identification protocol

As described in [33], two main approaches are available to identify LPV systems.

The first one is the *local approach*. It supposes that the varying parameter of the LPV model is available and can be set at *frozen* values while collecting the input and output data necessary to identify linear time invariant (LTI) models around these points by prediction error minimization. These models are then interpolated to obtain the full model in LPV form.

The second one is the *global approach*. This method uses input and output data as well as varying parameter data, which are directly measured or estimated, in order to identify the model in LPV form. However, these methods require a persisting excitation of the varying parameter during data collection, which can be difficult to ensure in practice.

In the proposed model, the varying parameter is the fraction ρ of εCO_2 that is measured in the output of the system, and can not be directly measured or controlled. This parameter takes continuous values between two extreme setups, the first one being the aerobic state, during low intensity effort, and the second one being the anaerobic state, during high intensity effort. Based on insights coming from the exercise physiology literature, equation (3.21) was proposed to model its behaviour. In this context, neither the *local* or the *global approach* can grasp the problem completely, thus, an hybrid approach was used.

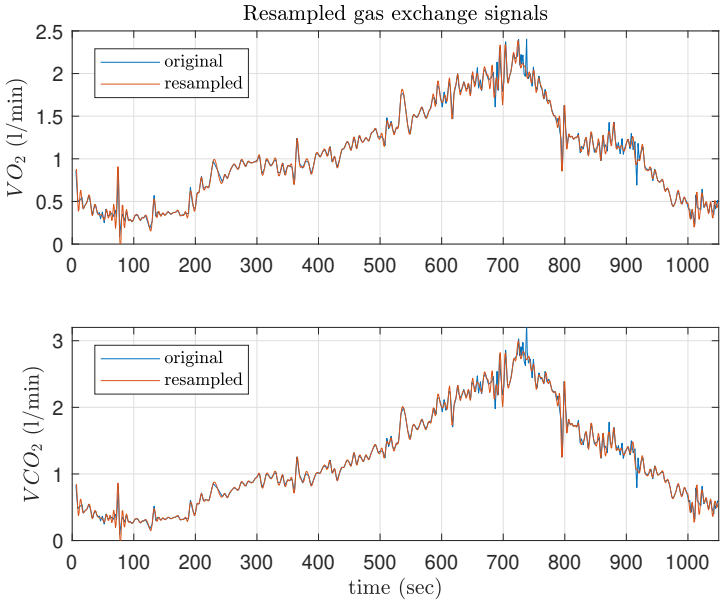

Figure 3.5: Resampled VO_2 and VCO_2 using the MATLAB spline interpolation method.

3.2.3.1 Data collection and processing

In order to identify the parameters of the model, experimental data is collected and processed. The signals of interest are the oxygen consumption VO_2, the carbon dioxide production VCO_2 and the power developed at the pedal level.

These signals are collected from two separate sources : the respiratory gas exchange signals are collected using an electronic ergospirometer (in our case the *Cortex Metamax 3B*) and the mechanical signals (like the pedalling cadence and the torque applied on the pedal) are measured directly on the electric bike (using connected pedals *Powertap P1*).

The respiratory gas exchange signals are measured breath-by-breath (BxB) which means that the respired gas is analyzed after each inhalation and each exhalation. Thus, the sampling period of these signals is not constant. Because the gas exchange model has to be identified at a constant sampling time Te, these signals are re-sampled by interpolation using the spline method implemented in MATLAB. An example of such interpolation is showed in Fig. 3.5. The mechanical signals are also resampled using the same technique.

After processing, new data sets are available are composed of synchronized VO_2, VCO_2 and power signals sampled uniformly. These data sets are used during the identification process to compute the parameters of the model.

3.2.3.2 Exercise profiles

In order to identify a model able to predict the behaviour of respiratory gas exchange for any exercise situation, the data sets used for the identification need to contain enough information

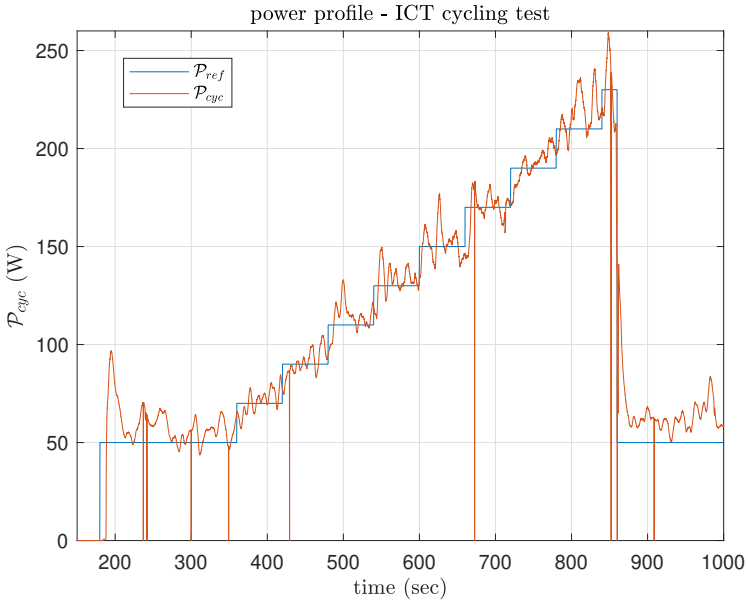

Figure 3.6: Power profile for the incremental cycling test (ICT). This test is constituted of steps of 20 Watts every minute until the maximal power $\mathcal{P}_{max}$ is reached.

about the behaviour of the system. Also, because the gas exchange model depends on the individual, the exercise sessions used for data acquisition have to be adapted to the individual's fitness. With this aim, three exercise scenarios were proposed : the *incremental cycling test* (ICT), the *iso-power cycling test* (ISO) and the *validation cycling test* (VAL).

First, the incremental cycling test is performed. This test is constituted of a resting period, followed by increments of 20 watts every minute until exhaustion. The aim of this test is to identify the maximal exercise capacity of the individual. The maximal exercise capacity is expressed in Watts as the maximal power $\mathcal{P}_{max}$ reached during the incremental test. The maximal capacity $\mathcal{P}_{max}$ is then used to calibrate the following tests. An example of the power profile of the incremental test is given in Fig. 3.6.

Then, the iso-power cycling test is performed. This test is composed by three steps of constant power separated by periods of rest. The first and last step are of 50% of the $\mathcal{P}_{max}$ identified in the ICT and the middle step is of 80% of the $\mathcal{P}_{max}$. The amplitude of the steps are chosen so that the first and last step are supposed *aerobic* and the middle step *anaerobic*. Thus, the dependency of the gas exchange dynamics to the effort intensity can be explored during the model identification. The on-off nature of the exercise is also useful to exhibit the kinetics of the gas exchange system. An example of the power profile of the iso-power test is given in Fig. 3.7.

Finally, the validation cycling test is performed. The purpose of this test is to provide an independent data-set than the ones used for the system identification in order to validate the model on new data. This test is constituted of a series of steps of varying intensity, very similar to what can be expected during an outdoor biking session. An example of the power profile of

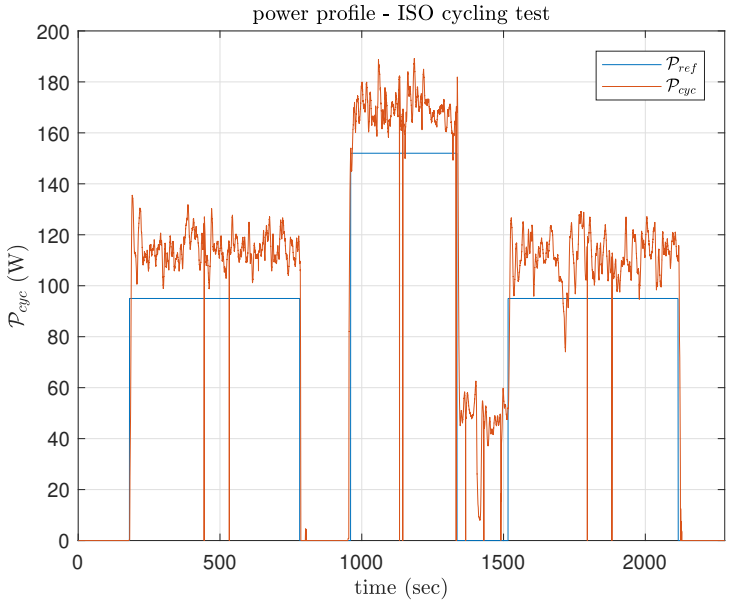

Figure 3.7: Power profile for the iso-power cycling test (ISO). The first and the last step are performed at 50% of the maximal power $\mathcal{P}_{max}$ reached during the incremental cycling test (ICT) and the middle step is performed at 80% of $\mathcal{P}_{max}$.

the validation test is given in Fig. 3.8.

3.2.3.3 Successive parametric optimization

In order to choose the most appropriate parameter values for the model, optimization problems are solved using experimental data. Because the role of the model is to provide a good estimation of the evolution of respiratory gas exchange during exercise, the cost function $J(p)$ of this optimization problem depends on the prediction error of the model and is expressed as follows :

$$J(p) := \sum_{k=1}^{N} \|\mathbf{y}(k) - \mathbf{y}_m(p,k)\|_2 \tag{3.23}$$

with p the vector containing the parameters of the model to be identified, $\mathbf{y}$ the vector containing the measured signals of mO_2 and mCO_{2tot}, $\mathbf{y}_m$ the output of the model and N the number of samples of the experimental signals.

The cost function J is minimized at each step of the identification process by solving the following non-convex optimization problem :

$$\min_{p} J(p) \tag{3.24}$$

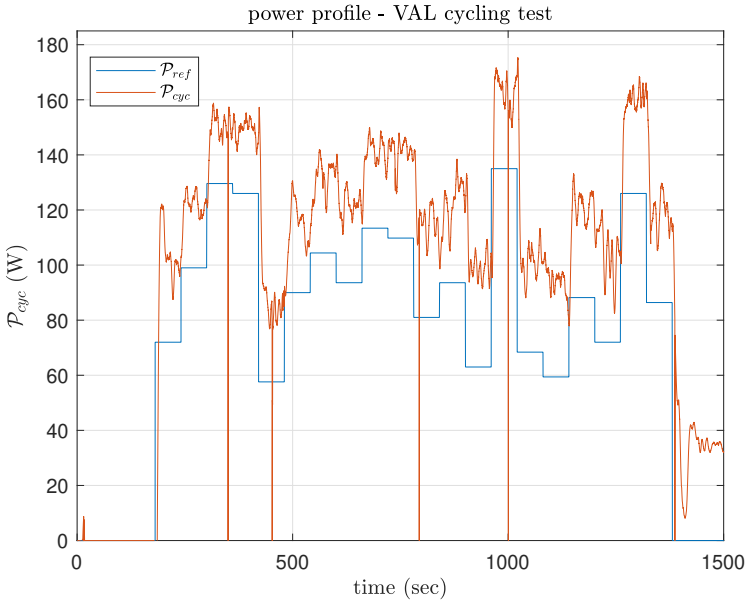

Figure 3.8: Power profile for the validation cycling test (VAL). This test is constituted of steps of random intensity aiming at reproducing an outdoor cycling session. The total duration of this test is 20 *min*.

subject to

$$\mathbf{x}_{k+1} = \mathbf{A}(\theta)\mathbf{x}_k + \mathbf{B}(\theta)u_k + \mathbf{B}(\theta)w_0 \tag{3.25}$$

$$\mathbf{y}_k = \mathbf{C}(\rho_k)\mathbf{x}_k \tag{3.26}$$

$$\rho_k = \rho(z_k) \tag{3.27}$$

1) Identification of the aerobic mode of the model

The parametric identification of the aerobic dynamics requires a sequence of data where the pedal power corresponds to an aerobic exercise, i.e. of moderate intensity. Here, we use the data of the first step of the ISO cycling test.

The identification process is carried out by considering only the parameters describing the aerobic dynamics which are θ_i for $i = \{1, \ldots, 4\}$ and w_0.

Here, $\rho = 0$ because it is assumed that there is no excess of carbon dioxide production in the considered data set due to the aerobic nature of the effort performed.

The optimization problem is formulated as follows :

Find the vector of parameters $p_1 = [\theta_1, \theta_2, \theta_3, \theta_4, w_0]^T$ *which minimizes (3.24), subject to (3.25) and (3.26), with matrices* $\mathbf{A}(\theta) = \mathbf{A}_1$, $\mathbf{B}(\theta) = \mathbf{B}_1$ *and* $\mathbf{C}(\rho_k) = \mathbf{C}_1$, *with*

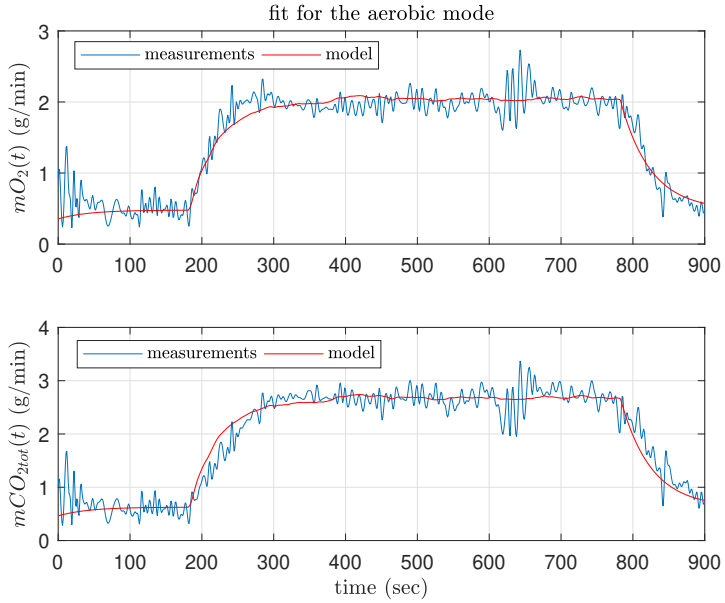

Figure 3.9: Fit between the experimental gas exchange signals and the output of the model for the aerobic mode.

$$\mathbf{A}_1 = \begin{bmatrix} \theta_1 & \theta_2 & 0 \\ 0 & \theta_3 & 0 \\ 0 & * & * \end{bmatrix} \qquad \mathbf{B}_1 = \begin{bmatrix} \theta_4 \\ \theta_4 \\ * \end{bmatrix} \qquad \mathbf{C}_1 = \begin{bmatrix} 1 & 0 & 0 \\ 0 & 1 & 0 \end{bmatrix} \tag{3.28}$$

The value of the coefficients denoted by $*$ is identified during the next steps of the identification process. A comparison of the experimental signals and the output of the model is shown in Fig. 3.9.

2) Identification of the anaerobic mode of the model

The parametric identification of the anaerobic dynamics requires a sequence of data where the pedal power corresponds to an anaerobic exercise, i.e. a high intensity workout. The identification process is carried out by considering only the parameters describing the anaerobic dynamics, which are θ_i for $i = \{5, 6, 7\}$.

Here, $\rho = 1$ because it is assumed that there is an important excess of carbon dioxide production in the considered data set. Coefficients θ_i for $i = \{1, \ldots, 4\}$ and w_0 are set to their identified value.

The optimization-based identification problem is formulated as follows :

Find the vector of parameters $p_2 = [\theta_5, \theta_6, \theta_7]^T$ *which minimizes (3.24), subject to (3.25)*

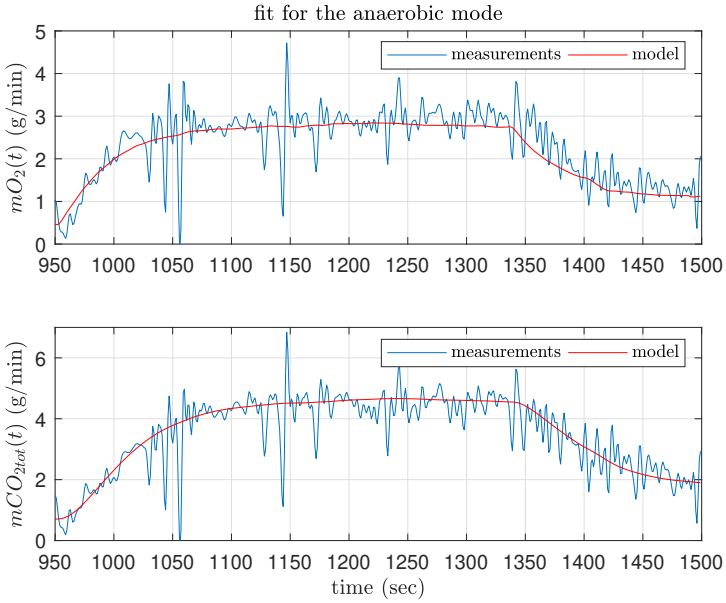

Figure 3.10: Fit between the experimental gas exchange signals and the output of the model for the anaerobic mode.

and (3.26), with matrices $\mathbf{A}(\theta)$ *and* $\mathbf{B}(\theta)$ *defined in (3.22) and* $\mathbf{C}(\rho_k) = \mathbf{C}_2$ *with*

$$\mathbf{C}_2 = \begin{bmatrix} 1 & 0 & 0 \\ 0 & 1 & 1 \end{bmatrix} \tag{3.29}$$

A comparison of the experimental signals and the output of the model is shown in Fig. 3.10.

3) Identification of the transition function ρ

Concerning the identification of the parameters of the transition function $\rho(z_k)$, given by (3.21), a data sequence including moderate and high intensity exercise has to be used. In this case, the full iso-power cycling test was used.

The optimization problem is formulated as follows :

Find the vector of parameters $p_3 = [\boldsymbol{z}_t, h]$ *which minimizes (3.24), subject to (3.25), (3.26) and (3.27), with matrices* $\mathbf{A}(\theta)$ *and* $\mathbf{B}(\theta)$ *defined in (3.22) and using the previously obtained parameters, i.e.* $\theta_1, ..., \theta_7, w_0$*. The matrix* $\mathbf{C}(\rho_k)$ *is defined as in (3.20) with* ρ_k *defined as in (3.21).*

A comparison of the experimental signals and the output of the model is shown in Fig. 3.11.

4) Refining the identified parameters

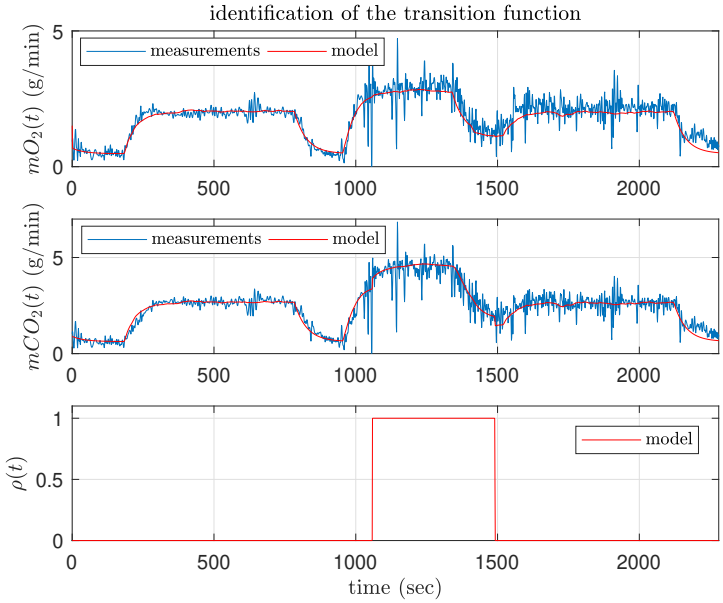

Figure 3.11: Fit between the experimental gas exchange signals and the output of the model for the transition function.

At the end of step *3)* all the parameters of the model have been assigned a value. However, each parameter was identified using specific scenarios. In order to reach good performances for non-specific scenarios, a last parametric identification problem is solved.

To do so, all the parameters are re-identified using the ICT and ISO datasets combined. The initial conditions for the optimization vector are taken equal to the parameter values obtained in steps *1), 2)* and *3)*.

The optimization problem is formulated as follows :

Find the vector of parameters $p_4 = [\theta_1, \theta_2, \theta_3, \theta_4, \theta_5, \theta_6, \theta_7, w_0, \boldsymbol{z}_t, h]$ *which minimizes (3.24), subject to (3.25), (3.26) and (3.27), with matrices* $\mathbf{A}(\theta)$ *and* $\mathbf{B}(\theta)$ *defined in (3.22) and using the previously obtained parameters, i.e.* $[\theta, w]^T$*. The matrix* $\mathbf{C}(\rho_k)$ *is defined as in (3.20) with* ρ_k *defined as in (3.21).*

A comparison of the experimental signals and the output of the model is shown in Fig. 3.12.

3.2.3.4 Model validation

Lastly, in order to verify that the model can perform well in any situations, its accuracy is tested using data-sets independent from the ones used for the identification. In this case, the validation cycling test is used.

A comparison of the experimental signals and the output of the model is shown in Fig. 3.13. After validation, it was concluded that the proposed respiratory gas exchange model is able to

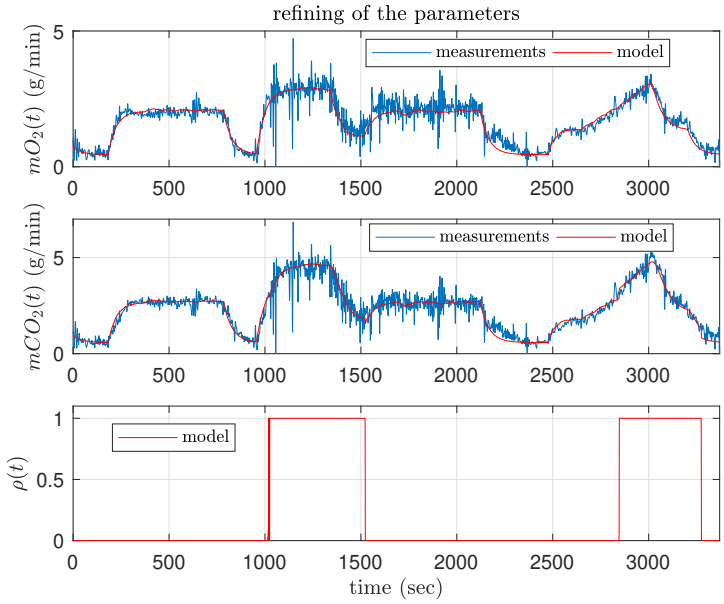

Figure 3.12: Refining of the parameters of the model.

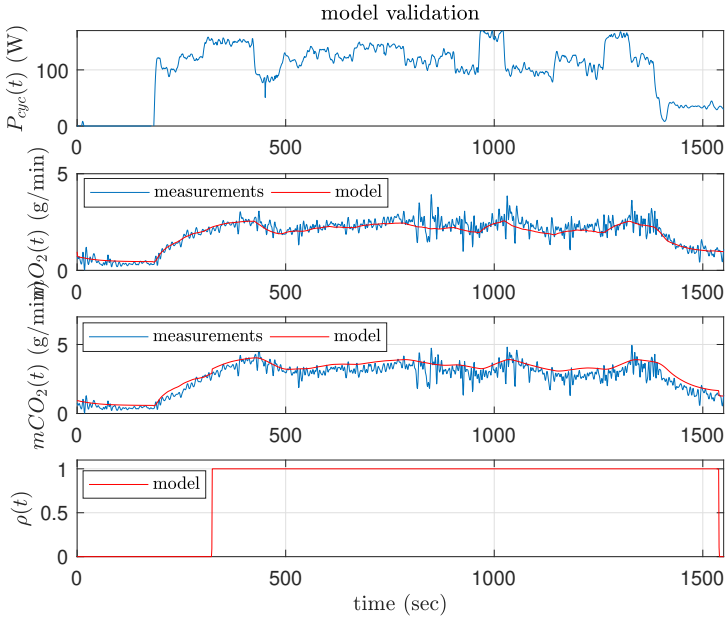

Figure 3.13: Validation of the model using the validation cycling test.

accurately estimate the oxygen consumption and carbon dioxide production during exercise. This model is used in this thesis as part of state estimation, control and simulation strategies.

3.3 Simulating cycling behaviors

In the previous sections, the development of a respiratory gas exchange model during exercise was presented. One of the main objectives of this thesis is to use this model in order to design control laws for an electric bike. To do so, the previous gas exchange model had to be completed using additional information regarding the dynamics of the bike and its interactions with the rider.

In this section, an approach is proposed in order to perform realistic simulations of cycling sessions based on models. To do so, two main problems have to be solved :

- First, the mechanical interactions of the bike and the environment (like the slope of the road for example) have to be described realistically using physical laws.
- Second, the behaviour of the cyclist has to be modeled. This problem is harder to tackle since a large number of factors influence the cycling behaviour of the cyclist (like its physical fitness, implicit feedback loops, road condition, etc.).

These two issues have already been considered in literature and the readers are referred to the very rich review work of Schwab and Meijaard regarding the modelling of bicycle dynamics and riders tracking behaviour using control theory [31].

The bicycle system if considered in all its complexity can lead to heavy nonlinear models. In the following, simple equations are proposed to describe the behaviour of the bike and the cyclist.

3.3.1 Equations of the bike's dynamics

In order to model the interactions between the bike, the cyclist and the environment, simplifying hypotheses were performed :

- *H1 - The movement of the bike takes place in the* $(\vec{x}_0, \vec{y}_0)$ *plane.*
- *H2 - The force applied by the cyclist is purely radial.*
- *H3 - The rolling movement of the bike wheels happens without sliding.*
- *H4 - The reduction ratio of the gears and chain is constant.*
- *H5 - The bike is not equipped with a freewheel system.*
- *H6 - The power transmission between the pedal and the rear wheel happens without loss.*

As conservative as these hypotheses may seem, they do not reduce the practical implementability of the solutions proposed, and are required in order to simplify the simulation setup and equation derivations. For example, the proposed control laws and estimators remain valid if the reduction ratio varies over time *(H4)* or if the real bike is equipped with a freewheel *(H5)*.

The system considered is constituted of both the bike and the cyclist, moving linearly on a slope of angle α in the $(\vec{x}_0, \vec{y}_0)$ plane. In the following, the linear forces are expressed using the notation $\vec{\mathcal{F}}_{\{P\}}$ and the torques $\vec{\mathcal{C}}_{\{P\}}$ with P the point of application.

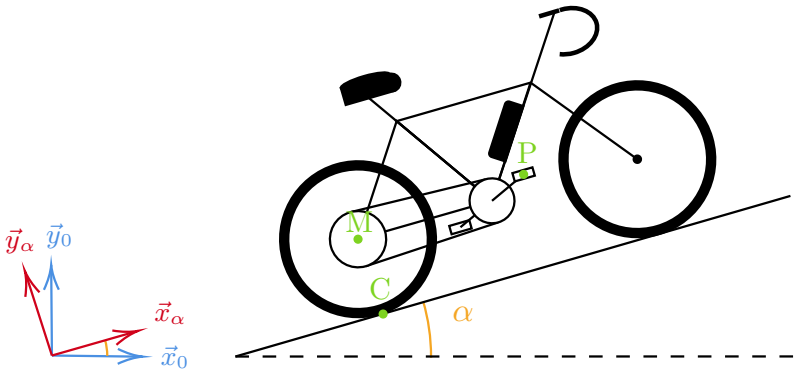

Figure 3.14: Bicycle in the plane.

The forces applied on the system are expressed at the point of contact C between the rear wheel and the ground :

- the action of gravity $\vec{\mathcal{F}}_g = -M_{tot} \cdot g \cdot \vec{y}_0$, with $M_{tot} = M_{bike} + M_{cyclist}$ the mass of the system.
- a viscous friction component $\vec{\mathcal{F}}_{vis} = -\beta \cdot v^2 \cdot \vec{x}_\alpha$ with β a positive constant and v the linear speed of the bike projected on $\vec{x}_\alpha$.
- the action of the electrical assistance $\vec{\mathcal{F}}_{mot\{C\}} = \mathcal{F}_{mot\{C\}} \cdot \vec{x}_\alpha$.
- the action of the cyclist $\vec{\mathcal{F}}_{cyc\{C\}} = \mathcal{F}_{cyc\{C\}} \cdot \vec{x}_\alpha$.

A cinematic model of the bike is given in Fig. 3.15 and the forces applied on the bike are represented in Fig. 3.16. The norms of $\vec{\mathcal{F}}_{mot}$ and $\vec{\mathcal{F}}_{cyc}$ are expressed as follows :

$$\mathcal{F}_{mot\{C\}} = \mathcal{C}_{mot\{M\}} \cdot R_w \tag{3.30}$$

$$\mathcal{F}_{cyc\{C\}} = \mathcal{F}_{cyc\{P\}} \cdot R_{PC} \tag{3.31}$$

The point M is located in the center of the rear wheel and the point P is located in the center of one of the pedals. The constant R_{PC} is the reduction ratio between the points P and C and is calculated using the gear ratio R as well as the pedalling radius R_p and the rear wheel radius R_w :

$$R_{PC} = \frac{R_p}{R_w} \cdot R \tag{3.32}$$

The relationships between the pedalling speed v_p and the speed of the bike v, as well as the force exerted by the cyclist on the pedal level $F_{cyc\{P\}}$ and the force exerted by the cyclist on the contact point C, $F_{cyc\{C\}}$, are recovered by conservation of the power. Indeed, using hypothesis *H6*, we have :

$$\mathcal{P}_{cyc\{C\}} = \mathcal{P}_{cyc\{P\}} \tag{3.33}$$

with $\mathcal{P}_{cyc\{P\}}$ the power developed by the cyclist on the pedal and $\mathcal{P}_{cyc\{C\}}$ the power developed by the cyclist on the wheel. By expanding this equation further, and using the definition of the reduction radio $R = \frac{w_p}{w} = \frac{R_{sp}}{R_{cr}} = \frac{\mathcal{C}_{cyc\{K\}}}{\mathcal{C}_{cyc\{M\}}}$ we have :

for the forces

$$\mathcal{P}_{cyc\{C\}} = \mathcal{P}_{cyc\{P\}} \tag{3.34}$$
$$\mathcal{F}_{cyc\{C\}} \cdot v = \mathcal{F}_{cyc\{P\}} \cdot v_p \tag{3.35}$$
$$\mathcal{F}_{cyc\{C\}} \cdot R_w \cdot w = \mathcal{F}_{cyc\{P\}} \cdot R_p \cdot w_p \tag{3.36}$$
$$\mathcal{F}_{cyc\{C\}} = \mathcal{F}_{cyc\{P\}} \cdot \frac{R_p}{R_w} \cdot \frac{w_p}{w} \tag{3.37}$$
$$\mathcal{F}_{cyc\{C\}} = \mathcal{F}_{cyc\{P\}} \cdot \frac{R_p}{R_w} \cdot R \tag{3.38}$$
$$\mathcal{F}_{cyc\{C\}} = \mathcal{F}_{cyc\{P\}} \cdot R_{PC} \tag{3.39}$$

for the speeds

$$\mathcal{P}_{cyc\{C\}} = \mathcal{P}_{cyc\{P\}} \tag{3.40}$$
$$\mathcal{F}_{cyc\{C\}} \cdot v = \mathcal{F}_{cyc\{P\}} \cdot v_p \tag{3.41}$$
$$\mathcal{C}_{cyc\{M\}} \cdot R_w \cdot v = \mathcal{C}_{cyc\{K\}} \cdot R_p \cdot v_p \tag{3.42}$$
$$v = \frac{\mathcal{C}_{cyc\{K\}}}{\mathcal{C}_{cyc\{M\}}} \cdot \frac{R_p}{R} \cdot v_p \tag{3.43}$$
$$v = R \cdot \frac{R_p}{R_w} \cdot v_p \tag{3.44}$$
$$v = R_{PC} \cdot v_p \tag{3.45}$$

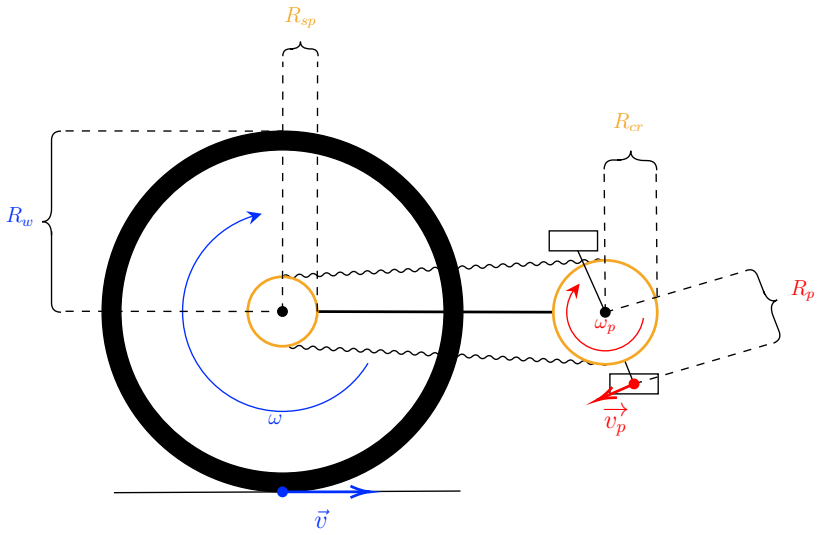

Figure 3.15: Cinematic model of the bike.

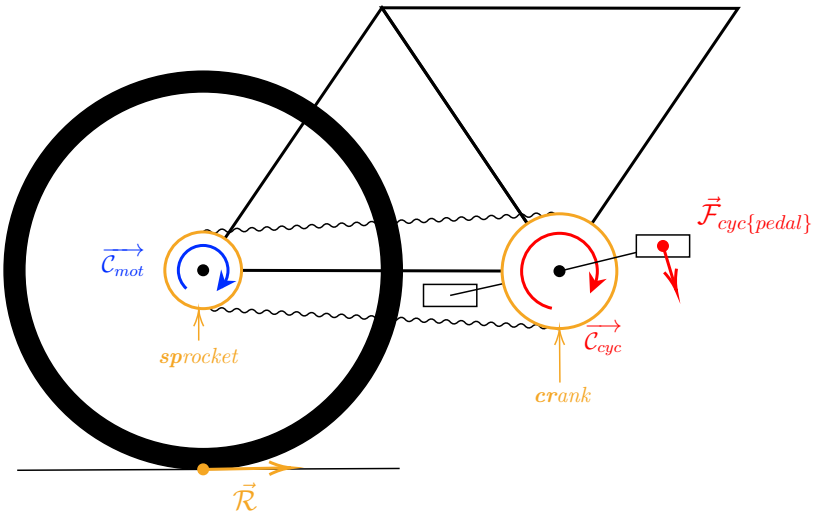

Figure 3.16: Actions applied on the bike.

The fundamental principle of dynamics applied to the contact point C gives :

$$M_{tot} \cdot \frac{d\vec{v}}{dt} = \vec{\mathcal{R}} \tag{3.46}$$

$$M_{tot} \cdot \frac{d\vec{v}}{dt} = \vec{\mathcal{F}}_{ext\{C\}} + \vec{\mathcal{F}}_{cyc\{C\}} + \vec{\mathcal{F}}_{mot\{C\}} \tag{3.47}$$

with $\vec{\mathcal{F}}_{ext\{C\}} = \vec{\mathcal{F}}_g + \vec{\mathcal{F}}_{vis}$ the sum of the action of gravity and viscous friction.

A discrete time version of equation (3.47) can be recovered by using a first order approximation $\frac{dv}{dt} \approx \frac{v(k+1)-v(k)}{Te}$ (with Te the sampling period) and projecting on $\vec{x_\alpha}$:

$$M_{tot} \cdot \frac{d\vec{v}}{dt}(t) \cdot \vec{x_\alpha} = \vec{\mathcal{R}}(t) \cdot \vec{x_\alpha} \tag{3.48}$$

$$M_{tot} \cdot \frac{d\vec{v}}{dt}(t) \cdot \vec{x_\alpha} = \vec{\mathcal{F}}_{ext\{C\}}(t) \cdot \vec{x_\alpha} + \vec{\mathcal{F}}_{cyc\{C\}}(t) \cdot \vec{x_\alpha} + \vec{\mathcal{F}}_{mot\{C\}}(t) \cdot \vec{x_\alpha} \tag{3.49}$$

$$M_{tot} \cdot \frac{d\vec{v}}{dt}(t) \cdot \vec{x_\alpha} = (\vec{\mathcal{F}}_{g\{C\}}(t) + \vec{\mathcal{F}}_{vis\{C\}}(t)) \cdot \vec{x_\alpha} \tag{3.50}$$

$$+\vec{\mathcal{F}}_{cyc\{C\}}(t) \cdot \vec{x_\alpha} + \vec{\mathcal{F}}_{mot\{C\}}(t) \cdot \vec{x_\alpha} \tag{3.51}$$

$$M_{tot} \cdot \frac{dv}{dt}(t) = -M_{tot} \cdot g \cdot sin(\alpha(t)) - K_{vis} \cdot v^2(t) + \mathcal{F}_{cyc}(t) + \mathcal{F}_{mot}(t) \tag{3.52}$$

$$M_{tot} \cdot \frac{v(k+1) - v(k)}{T_e} = -M_{tot} \cdot g \cdot sin(\alpha(k)) - K_{vis} \cdot v^2(k) + \mathcal{F}_{cyc}(k) + \mathcal{F}_{mot}(k) \tag{3.53}$$

And finally :

$$\begin{aligned} v(k+1) = v(k) &- \frac{g}{M_{tot}T_e} \cdot sin(\alpha(k)) - \frac{K_{vis}}{M_{tot}T_e} \cdot v^2(k) \\ &+ \frac{1}{M_{tot}T_e} \cdot \mathcal{F}_{cyc}(k) + \frac{1}{M_{tot}T_e} \cdot \mathcal{F}_{mot}(k) \end{aligned} \tag{3.54}$$

Thus, we expressed the relationship describing the evolution of the bike speed depending on the forces applied to it. The action of the motor $F_{mot}(k)$ is computed as the output of a control law. In order to express the action of the cyclist $F_{cyc}(k)$ in simulation, a novel approach is proposed in the following section.

3.3.2 The cycling force - velocity characteristic

3.3.2.1 Force - velocity characteristics in the literature

In order to perform simulations, the behaviour of the cyclist has to be approximated. One solution is to model it as a closed-loop system tracking a given speed or position trajectory over time. However, the objectives taken into account by a real cyclist during exercise are multi-fold and such strategy turns out to be oversimplifying.

In this approach, we propose to use a force-velocity characteristic of the cyclist in order to generate realistic $\mathcal{F}_{cyc}$ profiles in simulation. This choice is based on physiological considerations. Indeed, in 1938, Hill and colleagues demonstrated that a relationship existing between the load applied to a contracting muscle and its maximum speed of contraction [16]. The characteristic they proposed is the following :

$$(\mathcal{F} + a) \cdot (v + b) = c \tag{3.55}$$

with $\mathcal{F}$ the load, v the speed of contraction and a, b and c constant parameters. Formulated as such, this relationship can rewritten as

$$\mathcal{F} = \frac{c - ab - av}{v + b} \tag{3.56}$$

which is a rectangular hyperbola with asymptotes $\mathcal{F} = -1$ and $v = -b$. This formulation is interesting because it describes the fact that the faster the contraction happens the lesser the force, or as Hill hypothesized :

"the force exerted is greater the less rate of movement, and vice versa" [15]

An other interesting feature of this description is that a reachable maximal force $\mathcal{F}_{max}$ value (at $v = 0$) and maximal speed value v_{max} (at $\mathcal{F} = 0$) are admitted by the characteristic as described in Fig. 3.17, which translate the physical limitations of an exercising individual.

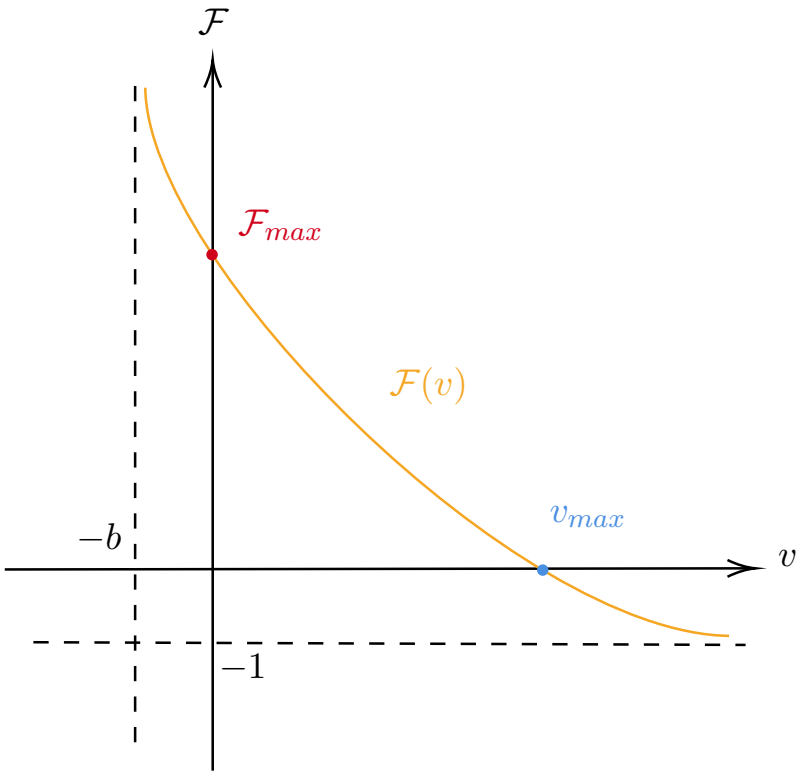

Figure 3.17: This figure represents the force - velocity muscle characteristic proposed by Hill. This characteristic shows that the force applied by a muscle decreases with the speed of its contraction. The maximal force $\mathcal{F}_{max}$ is applied at $v = 0$, and no force is applied for speeds higher than v_{max}.

Later, other models were proposed to describe this behaviour. These new approaches differed by the relationship they studied, which was either the force - velocity $\mathcal{F}(v)$ relationship or the torque - pedalling rate relationship $\mathcal{C}(w)$. Different shapes have been proposed to describe the characteristics, like linear, hyperbolic or double hyperbolic relationships. They also focused on different physical activities, in order to study the influence of training on the shape of the

characteristics. A brief summary of these approaches is proposed in Table 3.2, and readers are referred to the rich review paper of Alcazar and colleagues [1] for a more detailed analysis.

Authors	Year	Relationship	Model	Activity
Tihanyi et al. [37]	1982	$\mathcal{F}(v)$	hyperbola	knee extensions
McCartney et al. [27]	1985	$\mathcal{C}(w)$	inverse	cycling
Vandewalle et al. [38]	1987	$\mathcal{F}(v)$	linear	cycling
Seck et al. [32]	1995	$\mathcal{C}(w)$	linear	cycling
Buttelli et al. [10]	1996	$\mathcal{C}(w)$	linear	cycling
Rahmani et al. [30]	2001	$\mathcal{F}(v)$	linear	squat
Morin et al. [28]	2002	$\mathcal{F}(v)$	linear	cycling
Kholer et al. [19]	2005	$\mathcal{F}(v)$, $\mathcal{C}(w)$	linear, quadratic	cycling
Dorel et al. [12]	2005	$\mathcal{C}(w)$	linear, quadratic	cycling
Gardner et al. [14]	2007	$\mathcal{C}(w)$	linear	cycling

Table 3.2: Muscle characteristics in the literature.

The concept of cycling characteristics was used by Li and Horowitz in order to design adaptive control strategies for exercise machines in their pair papers [21, 22]. In order to do so, they first extended the concept of Hill characteristics in order to take into account the pedal angle during cycling. The new relationship they proposed took the form of what they called a *Hill surface* $\mathcal{F}(\theta, v)$. This Hill surface was used to characterise the personal cycling behaviour of the rider and was identified online using force, velocity and angle measurements in order to adapt the control strategy to the user. An example of Hill surface is represented in Fig. 3.18. This plot shows that for every pedal angle, a decreasing curve can be found between the force applied and the pedalling velocity. It also shows that for specific pedal angles, where the pedal sprocket is horizontal, the force applied is maximal, and where the pedal sprocket is vertical, the force applied is minimal. In order to simplify the parametrization of such curve $\mathcal{F}(\theta, v)$, they supposed affine relations $\mathcal{F}(v) = a(\theta) + b(\theta)v$ for each angle θ as shown in Fig. 3.19.

As mentioned in this section, a rigid mathematical relationship can be defined in order to model the decrease in the magnitude of the force applied by a contracting muscle in regard to the speed of contraction. Such relationship depends on the type of muscle considered and, to a larger extent, to the individual performing the effort. Thus, the force - velocity characteristic has *personalized* and *descriptive* properties. In the next sections, we propose to use such characteristic as a mean to generate realistic cycling force and velocity profiles in order to perform simulations.

3.3.2.2 Cycling characteristic : theoretical proposition

In this thesis, a cycling force - velocity characteristic was proposed. This characteristic relates the pedalling force on the pedal $\mathcal{F}_{cyc\{P\}}$ to the pedalling speed v_p in an affine fashion. For simplicity, in this section the point of application of the pedalling force is omitted and $\mathcal{F}_{cyc} \equiv \mathcal{F}_{cyc\{P\}}$. The proposed characteristic is given by :

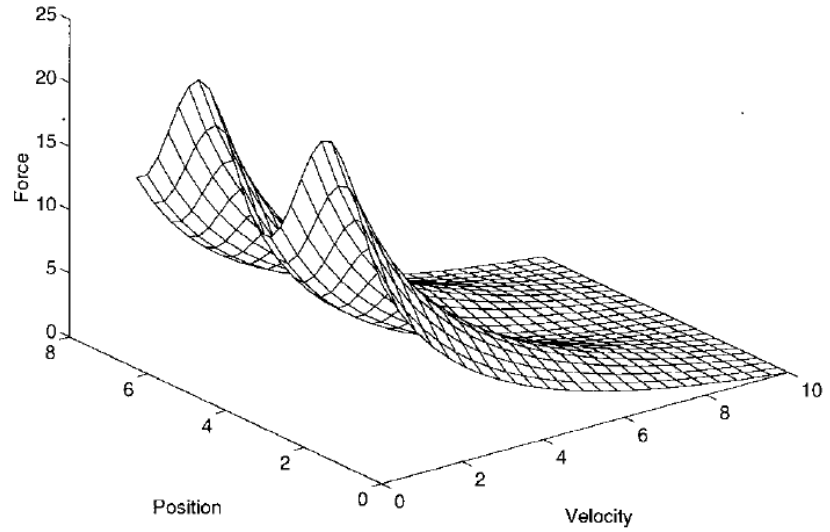

Figure 3.18: Hill surface proposed in [21], associating a Hill characteristic to any angle of the pedalling rotation.

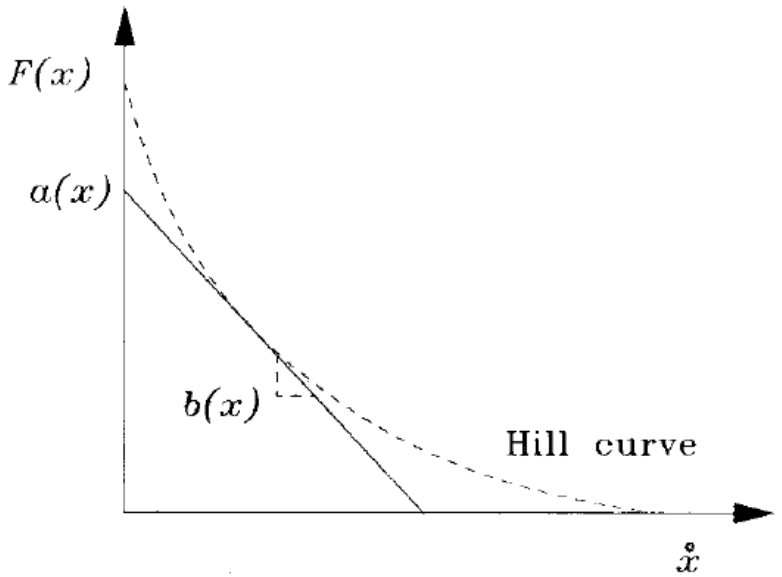

Figure 3.19: Affine approximation of a "slice" of the Hill surface for a given angle proposed in [21]. Here, x refers to the pedal angle θ and $\dot{x}$ to the pedalling speed v.

$$\mathcal{F}_{cyc}(v_p) = \mathcal{F}_{max} \qquad (\text{if } v_p \leq 0) \tag{3.57}$$

$$\mathcal{F}_{cyc}(v_p) = a v_p + b \qquad (\text{if } 0 \leq v_p \leq v_{max}) \tag{3.58}$$

$$\mathcal{F}_{cyc}(v_p) = 0 \qquad (\text{if } v_p \geq v_{max}) \tag{3.59}$$

with a and b constant parameters, $\mathcal{F}_{max} = b$ and $v_{max} = -\frac{b}{a}$. A representation of this characteristic is given in Fig. 3.20.

The main region of operation is given by equation (3.58), in this region the force applied on the pedal decreases affinely with the pedalling speed.

The region defined by equation (3.57) implies that for negative v_p the force applied on the pedal is equal to the maximum force $\mathcal{F}_{max}$. This is useful in simulation since it translates the will of the cyclist to always cycle forward. Also, this assumption is not a issue in practice since most bikes are equipped with a freewheel system that prevents the rider to cycle backward.

Finally, the region defined by equation (3.59) implies that for pedalling velocities higher than v_{max} the cyclist does not apply any force on the pedal. This assumptions translates the fact that if the speed of the bike is too high, the cyclist can not contribute in accelerating it through pedalling. Furthermore, the existence of such speed is given by the physiological limitations of the cyclist.

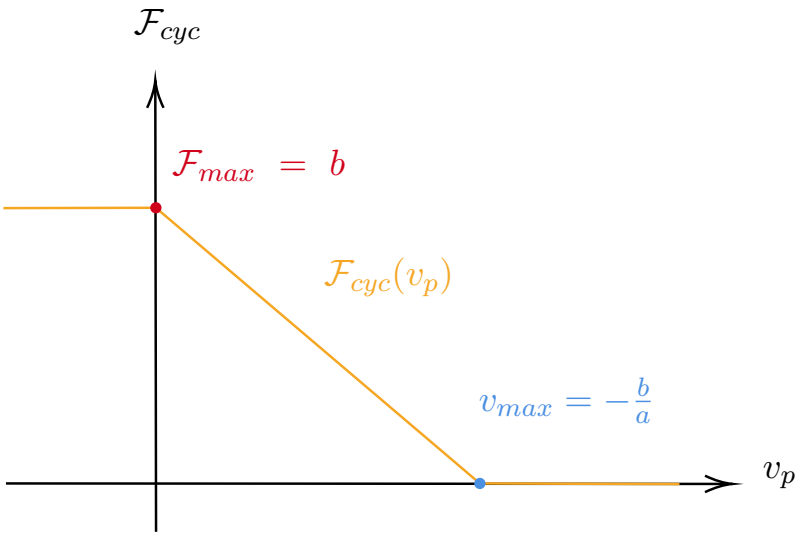

Figure 3.20: Proposed cycling force - velocity characteristic.

3.3.2.3 Cycling characteristic : practical validation

After proposing a structure for the cycling force - velocity characteristic, experimental data collection sessions were performed. The goal was to collect pedalling force and velocity signals for a given individual, identify the parameters a and b of the characteristic and check the validity of the identified characteristic against independent validation data.

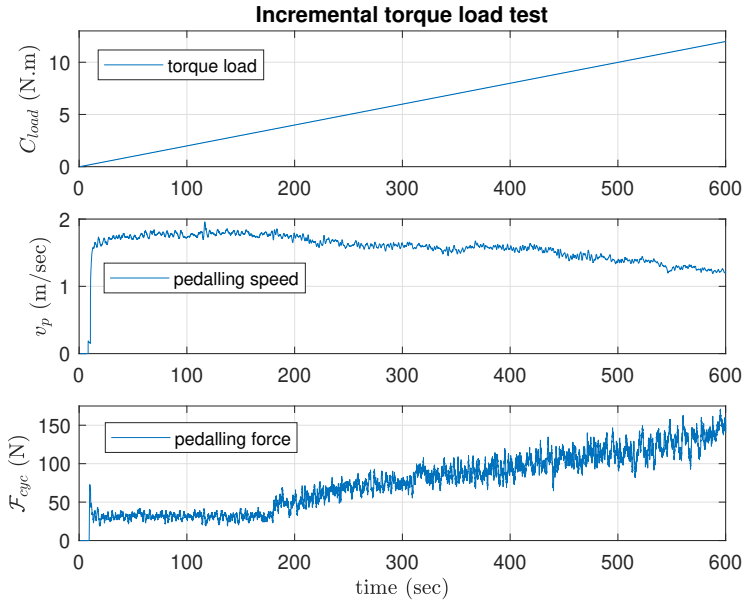

Figure 3.21: Experimental load profile for the identification of the cycling characteristic. Here, we see that the pedalling speed decreases and the pedalling force increases when the torque increases, which confirms the shape of the cycling characteristic.

1) Identification data collection

First, an exercise protocol was designed in order to collect the pedalling force and velocity data-sets required for the parameter identification. For the exercise session, the cyclist was asked to pedal at a chosen comfortable pedalling rate against a torque load increasing linearly with time generated by the electrical motor of the bike.

The test lasted 10 minutes and the torque load varied between 0 $N.m$ to 12 $N.m$. The cyclist was free to adjust its pedalling speed during the test. The collected experimental signals are showed in Fig. 3.21. During this test, the pedalling speed showed a slight decrease as the torque load increased and the pedalling force increased as the torque load increased. This translates in a correlation between an increase of the pedalling force when the pedalling speed decreases, which is coherent with the shape chosen for the characteristic.

2) Identification of the cycling characteristic

Then, the cycling characteristic was identified using the experimental data. In order to compute the parameters a and b of the characteristic, a polynomial of order 1, $\mathcal{F}_{cyc}^{char} = av_p^{meas} + b$, was identified in order to minimize the least square error between the measured cyclist force $\mathcal{F}_{cyc}^{meas}$ and the cyclist force computed using the characteristic $\mathcal{F}_{cyc}^{char}$. To do so, the *polyfit* MATLAB function was used.

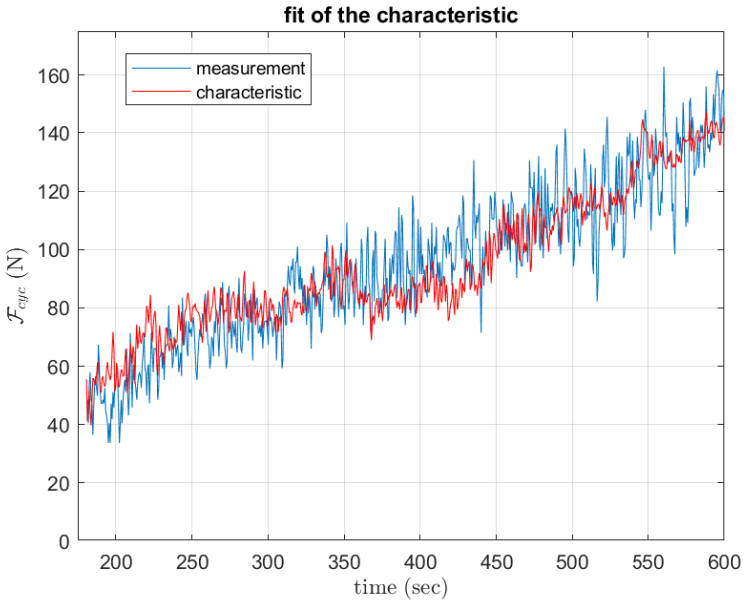

Figure 3.22: Fit of the cycling characteristic on the *identification* data-set.

For the presented data-set, the identified values for a and b are :

$$a = -162.64 \ (Nsec/m)$$
$$b = 340.68 \ (N)$$

The fit between $\mathcal{F}_{cyc}^{meas}$ and $\mathcal{F}_{cyc}^{char}$ computed using the identification data is showed in Fig. 3.22, and a comparison between the characteristic and the identification $(\mathcal{F}_{cyc}^{meas}, v_{cyc}^{meas})$ pairs is showed in Fig. 3.23. One can notice that the experimental pedalling force and velocity data reproduces a decreasing behaviour, captured successfully by an affine equation, as expected.

3) Validation data collection

In order to validate the robustness of the identified characteristic new data-sets were collected. A different cycling scenario, inspired from the respiratory gas exchange validation test of section 3.2, was chosen.

In this scenario, the torque load applied was piece-wise constant. It took values between $2N.m$ and $10N.m$ and changed every minute for a total of 8 minutes. The collected experimental signals are showed in Fig. 3.24.

4) Validation of the cycling characteristic

The fit between $\mathcal{F}_{cyc}^{meas}$ and $\mathcal{F}_{cyc}^{char}$ computed using the identification data is showed in

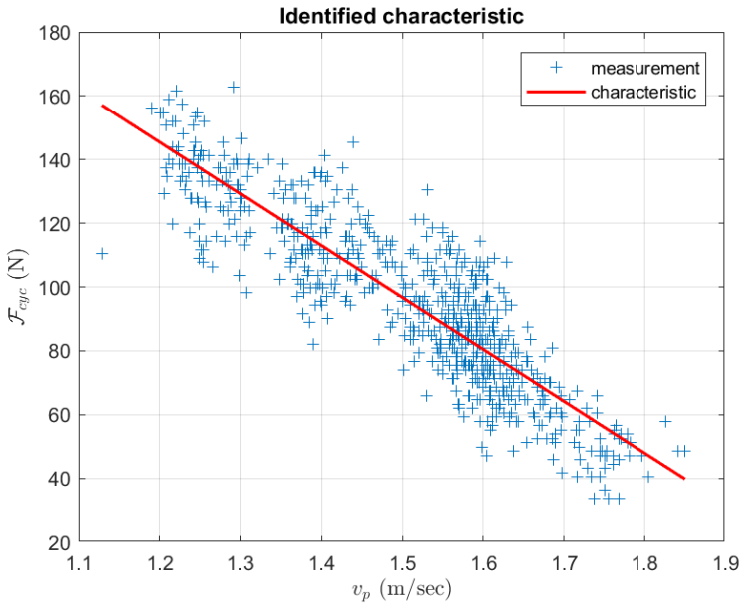

Figure 3.23: Experimental cycling characteristic against *identification* data.

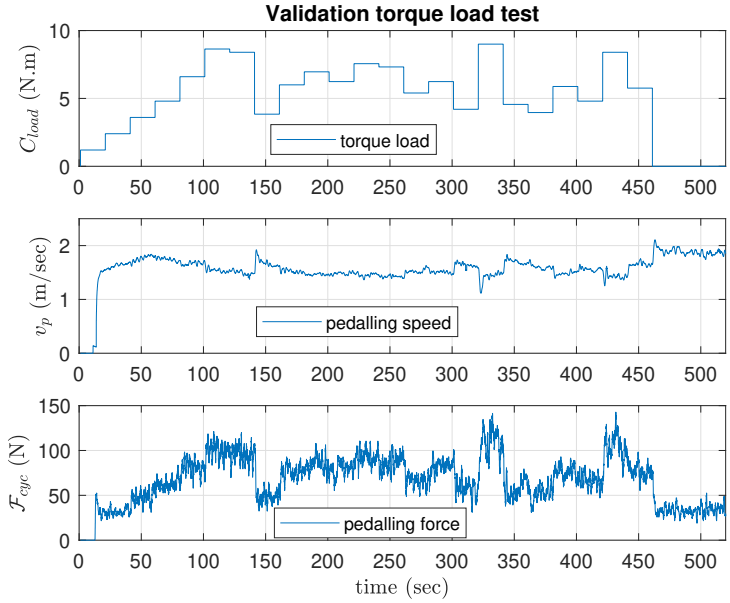

Figure 3.24: Experimental load profile for the validation of the cycling characteristic.

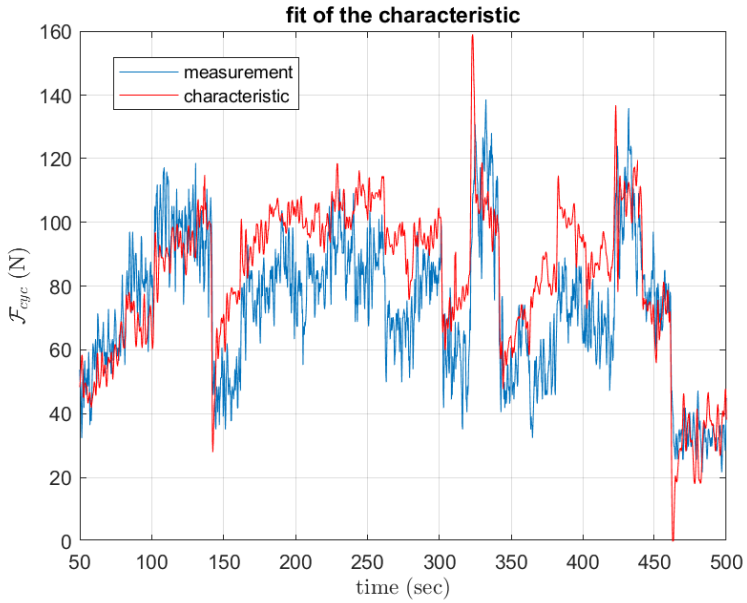

Figure 3.25: Fit of the cycling characteristic on the *validation* data-set.

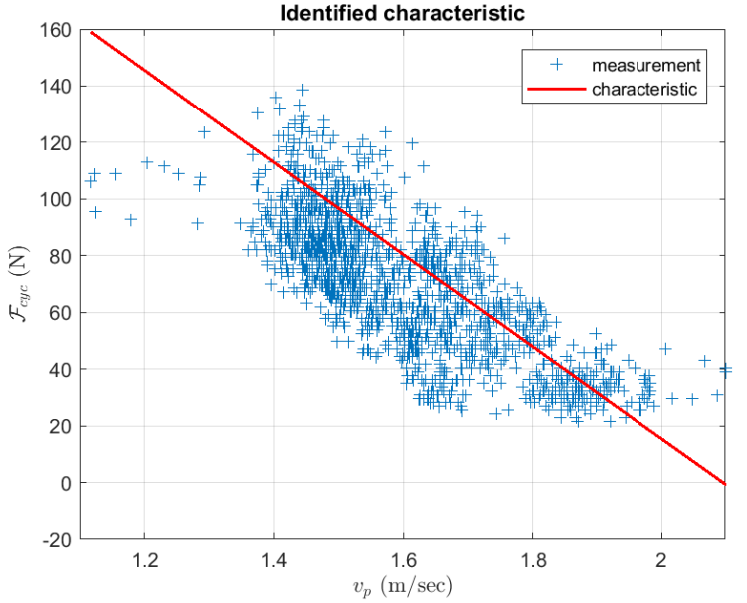

Figure 3.26: Experimental cycling characteristic against *validation* data.

Fig. 3.25, and a comparison between the characteristic and the identification $(\mathcal{F}_{cyc}^{meas}, v_{cyc}^{meas})$ pairs is showed in Fig. 3.26. These figures show a good fit between the previously identified characteristic and the validation data. This shows that the identified characteristic is able to reproduce similar pedalling force $\mathcal{F}_{cyc}$ based on values of pedalling speed v_p for a given individual.

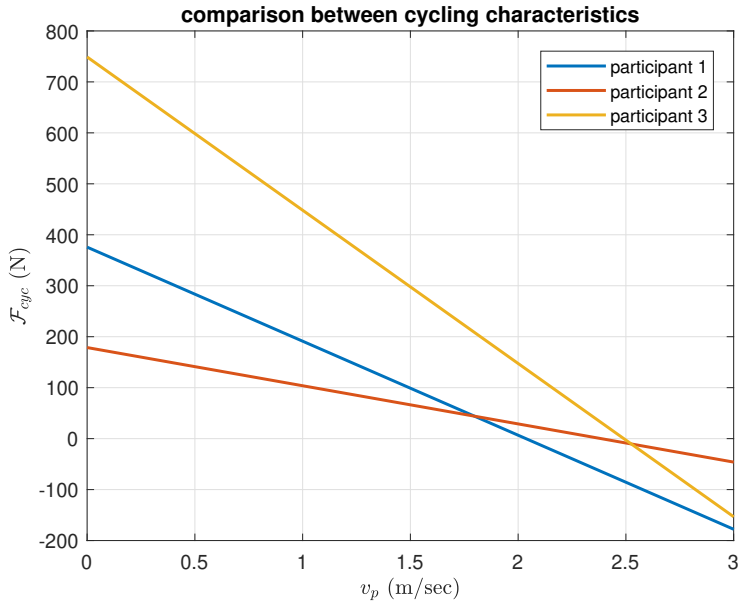

Figure 3.27: Comparison of the identified experimental cycling characteristics for 3 different individuals.

Multiple cycling characteristics were identified for different individuals and a comparison is showed in Fig. 3.27. This figure shows the characteristics of the two untrained individual (participants 1 and 2) and one trained individual (participant 3). One can notice that the maximal force $\mathcal{F}_{max}$, computed at $v_p = 0$, is much higher for participant 3, which correlates with the prior knowledge on its physical condition. The maximum pedalling speed v_{max} computed at $\mathcal{F}_{cyc} = 0$ does not differ greatly between the different participants, which can be explained by the fact that usually cyclist find a comfortable pedalling speed between 1 rotation per second and 2 rotations per second, corresponding here to $0.78m/sec$ and $1.57m/sec$.

5) Conclusion

The experimental tests permitted to draw several conclusions :

- *C1 - The affine structure chosen for the characteristic is coherent with experimental data.*
- *C2 - The cycling characteristic is robust against independent data.*
- *C3 - The cycling characteristic captures inter-individual differences.*

3.3.3 Simulation strategy

After validating the proposed cycling characteristic in practice, we propose to use such characteristic in order to generate realistic cycling force $\mathcal{F}_{cyc}$ profiles. To do so, at each instant k

of the simulation, the characteristic is used to choose the value for $\mathcal{F}_{cyc}(k)$ associated with the current value of pedaling speed $v_p(k)$. The value of $\mathcal{F}_{cyc}(k)$ is then used in the discrete time fundamental principal of dynamics applied to the bike and cyclist system, along with the current exterior force $\mathcal{F}_{ext}(k)$ and motor force $\mathcal{F}_{mot}(k)$ in order to compute the speed of the bike at the next instant $v(k+1)$. A scheme of the simulation strategy is proposed in Fig. 3.28.

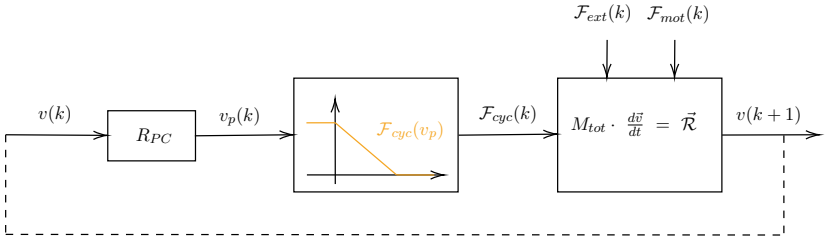

Figure 3.28: Cycling simulation method.

A simulation example is shown in the following figures. The scenario is the following, the bike starts the simulation with an initial velocity $v_0 = 0$, and accelerates under the action of the cyclist $\mathcal{F}_{cyc}$ and the external forces $\mathcal{F}_{ext}$. The extenal forces are computed as the sum of the action of gravity $\mathcal{F}_g = -M_{tot} \cdot g \cdot sin(\alpha)$, with α the angle of the slope in degrees, and the action of viscous friction $\mathcal{F}_{vis} = -K_{vis} \cdot v^2$. The angle of the slope is supposed equal to 0° for the first half of the simulation ($t = 0$ *sec* to $t = 150$ *sec*) and equal to 5° for the second half ($t = 150$ *sec* to $t = 300$ *sec*). The parameters of the simulation are the following :

Simulation parameter values		
$M_{tot} = 80$	$K_{vis} = 0.25$	$g = 9.8$
$a = -184.52$	$b = 375.72$	$T_e = 1$
$R_{PC} = 0.27$	$R = 15/42$	$R_p = 0.25$

The evolution of the mechanical and physiological quantities of the system is showed in Fig. 3.29. Initially, because the speed of the bike is equal to 0 and the slope is equal to 0, the only contribution is the pedalling force of the cyclist $\mathcal{F}_{cyc}$. At $v_p = 0$, the cyclist applies the maximum force $\mathcal{F}_{max}$ and the speed of the bike increases. With v increasing, the viscous friction increases, and the the pedalling force decreases. A first steady state is found when the system reaches a balance between the power developed by the cyclist $\mathcal{P}_{cyc}$ and the power depleted by the external actions $\mathcal{P}_{ext}$ as shown is Fig. 3.30. The respiratory gas exchange increase due to the increase in $\mathcal{P}_{cyc}$.

Then, at $t = 150$ *sec*, the slope of the road increases. The action of gravity $\mathcal{F}_g$ adds up to the viscous friction and the speed of the bike decreases. With the speed decreasing, the

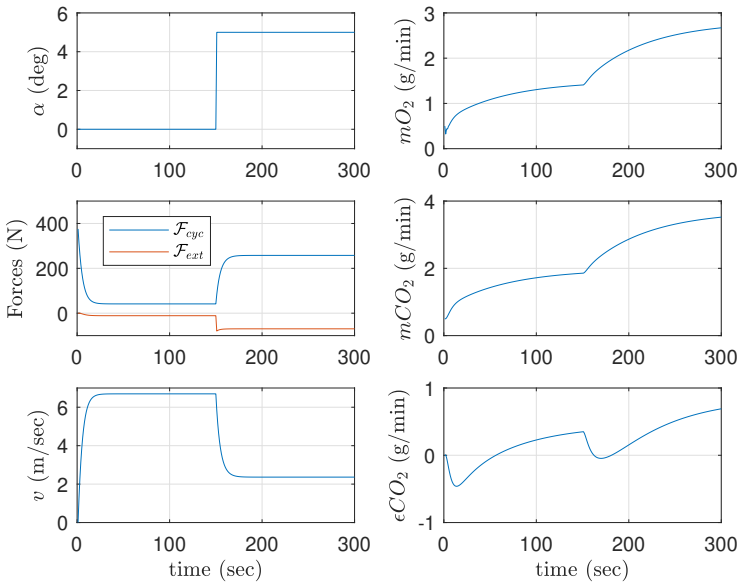

Figure 3.29: Evolution of the mechanical and physiological quantities of the system. The mechanical variables are displayed in the left column, with the angle of the slope α in degrees, the forces applied on the bike (the cyclist force $\mathcal{F}_p$ in blue, and the external force $\mathcal{F}_{ext}$ in red) and the bike velocity v. The physiological variables are displayed in the right column, with the oxygen consumption mO_2, the aerobic carbon dioxide production mCO_2 and the excess of carbon dioxide production ϵCO_2.

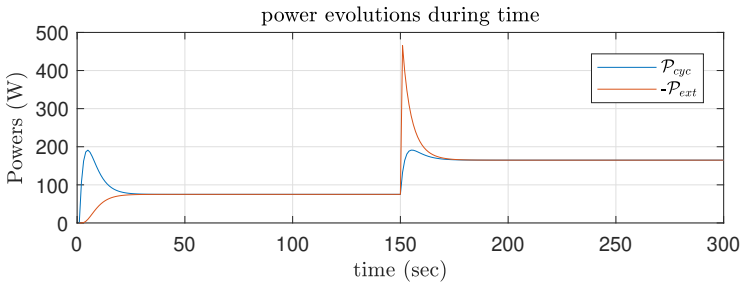

Figure 3.30: Evolution of the power provided by the cyclist and dissipated by the external forces. The powers are defined as $\mathcal{P}_{cyc} = \mathcal{F}_{cyc} \cdot v_p$ and $\mathcal{P}_{ext} = \mathcal{F}_{ext} \cdot v = (\mathcal{F}_g + \mathcal{F}_{vis}) \cdot v$.

action of the cyclist $\mathcal{F}_{cyc}$ increases to reach a new steady state. One can notice the two different equilibriums on the cycling characteristic showed in Fig. 3.31. The second equilibrium implies a higher pedalling power for the cyclist, which translate in a increase in respiratory gas exchanges.

To conclude, the use of the cyclist force - velocity characteristic is very useful in order to generate realistic behaviours for simulations. Such a simulator is crucial in order to design control laws for the electric bike, since in practice both the cyclist and the electrical assistance are interacting with each other as two independent closed-loop systems, and the outcome of this interaction is hard to predict before testing the control law on the real system.

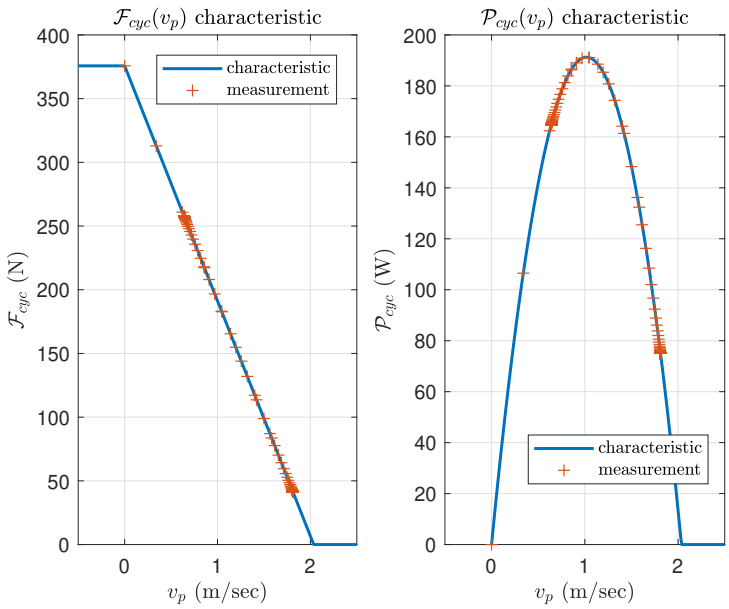

Figure 3.31: Superposition of the ($\mathcal{F}_{cyc}$,v_p) and ($\mathcal{P}_{cyc}$,v_p) pairs with the hypothesized force - velocity characteristic (on the left) and power - velocity characteristic (on the right). The power - velocity characteristic is obtained by multiplying the force - velocity characteristic by v_p.

3.4 Conclusion

In this chapter, the mechanical and physiological modeling of a cyclist is presented.

First, an overview of the existing control science methods used to model respiratory gas exchange and heart rate during exercise is given.

Then, the considered model for respiratory gas exchange used in this thesis is presented. It is showed that using experimental signals of power at the pedal level, oxygen consumption and carbon dioxide production during exercise, it is possible to identify a model for the respiratory gas exchange of a given individual. The identified is personal, and needs to be identified using a proposed protocol for any new considered individual. This model allows the prediction of both the oxygen consumption and the carbon dioxide production of an exercising cyclist.

In order to propose a model describing the behaviour of the system constituted of both the cyclist and the bike, a novel approach is proposed in order to model the pedalling force and velocity of a cyclist. This approach is based on a force-velocity characteristics that is identified using experimental data from an incremental torque cycling test.

Finally, together with a 2D dynamical model of the bike, the force-velocity characteristic of the cyclist is used to propose a new simulation strategy aiming at generating realistic cycling and

respiratory gas exchange signals for arbitrary biking scenarios in simulation. This contribution is interesting since it allows to integrate human-like behaviours in a simulated environment, which can then be used for cyclist performance prediction or control law design.

Bibliography

[1] Julian Alcazar, Robert Csapo, Ignacio Ara, and Luis M. Alegre.
On the Shape of the Force-Velocity Relationship in Skeletal Muscles: The Linear, the Hyperbolic, and the Double-Hyperbolic.
Frontiers in Physiology, 10:769, June 2019.

[2] Marco Altini, Julien Penders, and Oliver Amft.
Estimating Oxygen Uptake During Nonsteady-State Activities and Transitions Using Wearable Sensors.
IEEE Journal of Biomedical and Health Informatics, 20(2):469–475, March 2016.

[3] Robert Amelard, Eric T. Hedge, and Richard L. Hughson.
Temporal convolutional networks predict dynamic oxygen uptake response from wearable sensors across exercise intensities.
npj Digital Medicine, 4(1):156, December 2021.

[4] Alexander Artiga Gonzalez, Raphael Bertschinger, Fabian Brosda, Thorsten Dahmen, Patrick Thumm, and Dietmar Saupe.
Modeling Oxygen Dynamics under Variable Work Rate:.
In *Proceedings of the 3rd International Congress on Sport Sciences Research and Technology Support*, pages 198–207, Lisbon, Portugal, 2015. SCITEPRESS - Science and and Technology Publications.

[5] Alexander Artiga Gonzalez, Raphael Bertschinger, Fabian Brosda, Thorsten Dahmen, Patrick Thumm, and Dietmar Saupe.
Kinetic analysis of oxygen dynamics under a variable work rate.
Human Movement Science, 66:645–658, August 2019.

[6] Alexander Artiga Gonzalez, Raphael Bertschinger, and Dietmar Saupe.
Modeling VO2 and VCO2 with Hammerstein-Wiener Models:.
In *Proceedings of the 4th International Congress on Sport Sciences Research and Technology Support*, pages 134–140, Porto, Portugal, 2016. SCITEPRESS - Science and Technology Publications.

[7] Dur-e-Zehra Baig, Hao Su, T M Cheng, A V Savkin, S W Su, and B G Celler.
Modeling of human Heart Rate response during walking, cycling and rowing.
In *2010 Annual International Conference of the IEEE Engineering in Medicine and Biology*, pages 2553–2556, Buenos Aires, August 2010. IEEE.

[8] Dur-e-Zehra Baig, A. V. Savkin, and B. G. Celler.
Estimation of oxygen consumption during cycling and rowing.
In *2012 Annual International Conference of the IEEE Engineering in Medicine and Biology Society*, pages 711–714, San Diego, CA, August 2012. IEEE.

[9] Andrew Borror, Michael Mazzoleni, James Coppock, Brian C. Jensen, William A. Wood, Brian Mann, and Claudio L. Battaglini.
Predicting oxygen uptake responses during cycling at varied intensities using an artificial neural network.
Biomedical Human Kinetics, 11(1):60–68, January 2019.

[10] O. Buttelli, H. Vandewalle, and G. Prs.
The relationship between maximal power and maximal torque-velocity using an electronic ergometer.
European Journal of Applied Physiology and Occupational Physiology, 73(5):479–483, June 1996.

[11] T.M. Cheng, A.V. Savkin, B.G. Celler, S.W. Su, and Lu Wang.
Nonlinear Modeling and Control of Human Heart Rate Response During Exercise With Various Work Load Intensities.
IEEE Transactions on Biomedical Engineering, 55(11):2499–2508, November 2008.

[12] S. Dorel, C. A. Hautier, O. Rambaud, D. Rouffet, E. Van Praagh, J.-R. Lacour, and M. Bourdin.
Torque and Power-Velocity Relationships in Cycling: Relevance to Track Sprint Performance in World-Class Cyclists.
International Journal of Sports Medicine, 26(9):739–746, November 2005.

[13] Barry W. Fudge, John Wilson, Chris Easton, Laura Irwin, Jonathan Clark, Olivia Haddow, Bengt Kayser, and Yannis P. Pitsiladis.
Estimation of Oxygen Uptake during Fast Running Using Accelerometry and Heart Rate.
Medicine & Science in Sports & Exercise, 39(1):192–198, January 2007.

[14] A. Scott Gardner, James C. Martin, David T. Martin, Martin Barras, and David G. Jenkins.
Maximal torque- and power-pedaling rate relationships for elite sprint cyclists in laboratory and field tests.

European Journal of Applied Physiology, 101(3):287–292, September 2007.

[15] W Hartree and AV Hill.
The recovery heat-production in muscle.
The Journal of Physiology, 56(5):367, 1922.

[16] Archibald Vivian Hill.
The heat of shortening and the dynamic constants of muscle.
Proceedings of the Royal Society of London. Series B-Biological Sciences, 126(843):136–195, 1938.

[17] K. J. Hunt and D. B. Allan.
A stochastic Hammerstein model for control of oxygen uptake during robotics-assisted gait.
International Journal of Adaptive Control and Signal Processing, pages n/a–n/a, 2008.

[18] Nadia Rosero Ibarra.
Modeling and observation applied to physiology-aware control for cycling.
PhD thesis, Université Grenoble Alpes, 2018.

[19] Götz Kohler and Urs Boutellier.
The generalized force–velocity relationship explains why the preferred pedaling rate of cyclists exceeds the most efficient one.
European Journal of Applied Physiology, 94(1-2):188–195, May 2005.

[20] Joris Lefever, Daniel Berckmans, and Jean-Marie Aerts.
Time-variant modelling of heart rate responses to exercise intensity during road cycling.
European Journal of Sport Science, 14(sup1):S406–S412, January 2014.

[21] Perry Y. Li and Roberto Horowitz.
Control of Smart Exercise Machines Part I: Problem Formulation and Non-Adaptive Control.
IEEE/ASME Transactions onMechatronics, 2(4):237–247, December 1997.

[22] Perry Y Li and Roberto Horowitz.
Control of Smart Exercise Machines—Part II: Self-Optimizing Control.
IEEE/ASME Transactions on Mechatronics, 2(4):248–258, December 1997.

[23] Melanie Ludwig, Harald G. Grohganz, and Alexander Asteroth.
A Convolution Model for Prediction of Physiological Responses to Physical Exercises.
In Jan Cabri, Pedro Pezarat-Correia, and João Vilas-Boas, editors, *Sport Science Research and Technology Support*, volume 975, pages 18–35. Springer International Publishing, Cham, 2016.

Series Title: Communications in Computer and Information Science.

[24] Melanie Ludwig, Katrin Hoffmann, Stefan Endler, Alexander Asteroth, and Josef Wiemeyer.
Measurement, Prediction, and Control of Individual Heart Rate Responses to Exercise—Basics and Options for Wearable Devices.
Frontiers in Physiology, 9:778, June 2018.

[25] Melanie Ludwig, Ashok Meenakshi Sundaram, Matthias Füller, Alexander Asteroth, and Erwin Prassler.
On Modeling the Cardiovascular System and Predicting the Human Heart Rate under Strain:.
In *Proceedings of the 1st International Conference on Information and Communication Technologies for Ageing Well and e-Health*, pages 106–117, Lisbon, Portugal, 2015. SCITEPRESS - Science and and Technology Publications.

[26] Michael J. Mazzoleni, Claudio L. Battaglini, Kerry J. Martin, Erin M. Coffman, and Brian P. Mann.
Modeling and predicting heart rate dynamics across a broad range of transient exercise intensities during cycling.
Sports Engineering, 19(2):117–127, June 2016.

[27] N. McCartney, G. Obminski, and G. J. Heigenhauser.
Torque-velocity relationship in isokinetic cycling exercise.
Journal of Applied Physiology, 58(5):1459–1462, May 1985.

[28] Jean-Benoıt Morin, Frédérique Hintzy, Alain Belli, and Frédéric Grappe.
Relations force–vitesse et performances en sprint chez des athlètes entraınés.
Science & sports, 17(2):78–85, 2002.

[29] Gianluigi Pillonetto, Francesco Dinuzzo, Tianshi Chen, Giuseppe De Nicolao, and Lennart Ljung.
Kernel methods in system identification, machine learning and function estimation: A survey.
Automatica, 50(3):657–682, March 2014.

[30] Abderrehmane Rahmani, Fabrice Viale, Georges Dalleau, and Jean-René Lacour.
Force/velocity and power/velocity relationships in squat exercise.
European Journal of Applied Physiology, 84(3):227–232, March 2001.

[31] A. L. Schwab and J. P. Meijaard.
A review on bicycle dynamics and rider control.
Vehicle System Dynamics, 51(7):1059–1090, July 2013.

[32] D. Seck, H. Vandewalle, N. Decrops, and H. Monod.
Maximal power and torque-velocity relationship on a cycle ergometer during the acceleration phase of a single all-out exercise.
European Journal of Applied Physiology and Occupational Physiology, 70(2):161–168, 1995.

[33] Olivier Sename, Peter Gaspar, and József Bokor.
Robust control and linear parameter varying approaches: application to vehicle dynamics, volume 437.
Springer, 2013.

[34] Steven W. Su, Branko G. Celler, Andrey V. Savkin, Hung T. Nguyen, Teddy M. Cheng, Ying Guo, and Lu Wang.
Transient and steady state estimation of human oxygen uptake based on noninvasive portable sensor measurements.
Medical & Biological Engineering & Computing, 47(10):1111–1117, October 2009.

[35] Steven W. Su, Lu Wang, Branko G. Celler, and Andrey V. Savkin.
Oxygen Uptake Estimation in Humans During Exercise Using a Hammerstein Model.
Annals of Biomedical Engineering, 35(11):1898–1906, October 2007.

[36] Husni Thamrin.
Modelling the respiratory control system in human subjects for excercise conditions.
PhD thesis, University of Glasgow, 2008.

[37] J. Tihanyi, P. Apor, and Gy. Fekete.
Force-velocity-power characteristics and fiber composition in human knee extensor muscles.
European Journal of Applied Physiology and Occupational Physiology, 48(3):331–343, April 1982.

[38] H. Vandewalle, G. Peres, J. Heller, J. Panel, and H. Monod.
Force-velocity relationship and maximal power on a cycle ergometer: Correlation with the height of a vertical jump.
European Journal of Applied Physiology and Occupational Physiology, 56(6):650–656, September 1987.

[39] Lin Ye, Ahmadreza Argha, Branko G. Celler, Yi Zhang, Hung T. Nguyen, and Steven W. Su.
Nonparametric modelling of VO2 response to exercise.
In *2017 39th Annual International Conference of the IEEE Engineering in Medicine and Biology Society (EMBC)*, pages 1525–1528, Seogwipo, July 2017. IEEE.

[40] Lin Ye, Ahmadreza Argha, Hairong Yu, Branko G. Celler, Hung T. Nguyen, and Steven Su.

Dynamic characteristics of oxygen consumption.
BioMedical Engineering OnLine, 17(1):44, December 2018.

[41] Hairong Yu, Tian Xie, and Steven Su.
Oxygen Uptake Response to Switching Stairs Exercise by Non-parametric Modeling.
preprint, In Review, May 2022.

[42] Andrea Zignoli, Alessandro Fornasiero, Enrico Bertolazzi, Barbara Pellegrini, Federico Schena, Francesco Biral, and Paul B. Laursen.
State-of-the art concepts and future directions in modelling oxygen consumption and lactate concentration in cycling exercise.
Sport Sciences for Health, 15(2):295–310, August 2019.

[43] Andrea Zignoli, Alessandro Fornasiero, Matteo Ragni, Barbara Pellegrini, Federico Schena, Francesco Biral, and Paul B Laursen.
Estimating an individual's oxygen uptake during cycling exercise with a recurrent neural network trained from easy-to-obtain inputs: A pilot study.
PLoS One, 15(3):e0229466, 2020.

Chapter 4

Estimation of respiratory gas exchange during exercise

Contents

In control applications, more than often, the states of the system to be controlled are not directly accessible through measurements. However, many control strategies are based on the knowledge of the states, which is why the problem of estimating state variables is so crucial. Usually, state estimation strategies are based on the conjoint knowledge of a plant model and direct measurements of states or outputs like for the very classical Luenberger state observer [28].

For general setups, when the plant model is not known with full accuracy, or the measurements are corrupted by noise, different strategies have been developed. One of the main objective of such strategies is to derive uncertainty bounds on the state measurement based on design assumptions on the magnitude of the uncertainties and noises affecting the system. Such estimation strategies can be referred to as *bounded estimation approaches*.

The first section of this chapter is dedicated to give an overview of the different bounded estimation strategies, with a highlight of the set-membership estimation method proposed by Nassim Loukkas which inspired the work presented in the second section of this chapter. The second and third sections are dedicated to the online estimation of respiratory gas exchange during exercise, based respectively on a set-membership observer and a proportional-integral observer.

This chapter requires some understanding of Linear Matrix Inequalities (LMI) and their manipulation. As an introduction, the reader is referred to this guide by Caverly and Forbes [6]. In order to solve LMIs on Matlab, the CVX toolbox was used [18, 19]. This chapter also involves some ellipsoidal geometry concepts, which are partly presented in the documentation of the Ellipsoidal Toolbox by Kurzhanskiy [31]. This toolbox is used in order to plot ellipsoidal sets on Matlab.

4.1 Bounded state estimation approaches

Two main families of approaches have been proposed in order to estimate the states of a system with uncertainty bounds : the *stochastic* approaches and the *deterministic* approaches. In this section, an overview of these two families is given.

4.1.1 Stochastic approaches

The adjective *stochastic* refers to a phenomenon that is described by a random probability distribution. In the context of state estimation, stochastic approaches are based on the consideration that the system of interest is random in nature. This is justified by the fact that in practice any measurement is affected by a random noise which, if taken into accounts, affects the whole estimation strategy.

The main stochastic state estimation approach was proposed by Kalman in 1960 and was later named after him as the Kalman Filter (KF) [28]. Initially developed for linear systems, it

was later extended to nonlinear systems in [27]. The Kalman Filter is based on an iterative procedure in two steps. The first step is the *prediction* step : a prior estimate of the state variable and the model of the system are used to produce a prediction of the next state variable. The second step is the *update* step : using a measurement of the output of the system, the previous estimation is updated. To update the estimate of the state, the algorithm uses information on the accuracy of the model and of the measurement under the form of covariance matrices. The Kalman Filter produces a final estimate of the state as a weighted average between the model and the measurement with the most accurate of the two weighting more than the other. By design, the estimate produced by the Kalman Filter is proved to be optimal in the case of a linear system affected by white Gaussian noise.

Later, this estimation technique was extended to the case of uncertain linear systems. Two objectives arise in this setup : the gain of the Kalman Filter is chosen such that it takes into account all the possible values of the system's parameters, and, bounds on the estimation are computed to be as less conservative as possible. For the discrete-time case several approaches have been proposed. Xie and colleagues studied systems affected by norm bounded parameter uncertainties on the state and output matrices in [32], Chen and colleagues proposed the concept of Interval Kalman Filter (IKF) for interval systems where the system matrices belong to known intervals in [21]. In these two approaches, bounds on the estimation error *covariance* are computed based on the solution of two Riccati equations. New estimation bounds were proposed by Zhu and colleagues in [49]. All three approaches only considered additive noise in the design and Yang and colleagues extended the method to the case of multiplicative noises as well in [15].

Stochastic approaches, in particular the Kalman Filter, have proven to be efficient solutions for state estimation with many implementation examples along the years. However, the need for known statistical distributions of the disturbances affecting the model and the measurement beforehand is challenging in practice.

4.1.2 Deterministic approaches

Another set of approaches to bounded state estimation is the one of *deterministic* approaches. The adjective deterministic in control theory relates to methods that allow to formulate hard guarantees on the behavior of the system. In this sense, it is radically different from stochastic approaches. For example, while stochastic approaches are used to derive confidence intervals on the state estimate depending on a given likelihood (x *belongs to* $[-1; 1]$ *with a confidence level of* 95%), deterministic approaches are used to derive intervals, potentially more conservative, but true at all time (x *is guaranteed to belong to* $[-1.6; 1.6]$). To derive deterministic estimation strategies, a common approach is to suppose that the uncertainties and the noise affecting the system belong to known sets or intervals at the design stage itself. From these hypotheses, sets including the estimation error at all time can be derived and propagated along time.

A famous deterministic state estimation approach is the one of *interval observers*. It consists in framing the state estimate with lower and upper bounds at all time coming from two sub-observers. To do so, in addition to the stability constraint, the observer state matrix has to be positive definite in the discrete-time setup and Metzler in the continuous-time setup. These two constraints are difficult to satisfy at all time and strategies have been proposed based on constant or time-varying transformations to ensure it. Even when these conditions are fulfilled, they often conflict with the performances of the state observer, with for example observer gains implying a slow convergence rate of the estimation in order to fulfill the positivity and stability constraints. This kind of state observer is particularly applied to fault diagnosis or biological systems like in [17]. The observer gain satisfying the constraints can be computed as the solution of a Linear Matrix Inequality (LMI) like in [47] or [13]. Recent approaches are exploring solutions where the conditions on the observer matrices are relaxed like in [36]. For a review of interval state observer methods readers are referred to [29].

Another approach is the one of *set-membership observers*. It is based on the hypothesis that the uncertainties and noises affecting the system belong to known sets and that their influence can be propagated in time in order to define a set containing the estimation errors. In some cases, the propagation is *non conservative* and is based on the successive intersection of a reachable set defined by the dynamics of the system and a compatible set defined from measurements. In these cases, the estimation error set is computed by solving an optimization problem online, aiming at finding the least conservative set in adequation with the reachable and compatible sets. Here, a tradeof between the conservatism of the computed set and the computational burden of the solution has to be found. The complexity of the optimization problem to solve is directly related to the complexity of the shape used to define the estimation error set, and various shapes have been proposed in the literature. Initially, Schweppe proposed to use an ellipsoid in order to frame the estimation error in his seminal paper [41] but later other shapes were proposed like paralellotopes, polyhedrons or polytopes. An illustration of the differences in the conservatism of different set shapes is proposed in Fig. 4.2. Simple shapes like ellipsoids, which are defined by a positive matrix of the order of the system, are convenient in terms of computations but might introduce some conservativeness in the estimation. More complicated shapes like polyhedrons can provide a tighter estimation of the states of the system, but because they are defined by an arbitrary high number of elements (each vertex for example) they can introduce additional complexity in the computations. An illustration of the different shapes used in given in Fig. 4.1. A non exhaustive summary of different methods and shapes if given in Table 4.1, and readers are referred to the book from Blanchini and Miani [5] for a detailed review.

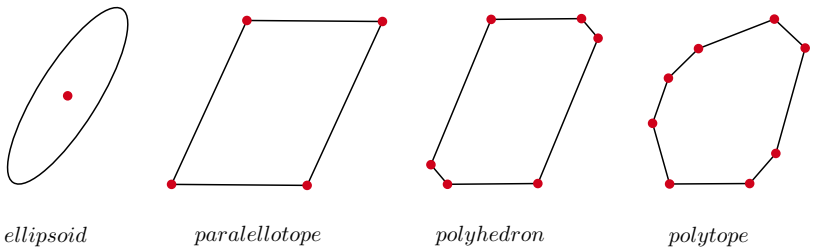

Figure 4.1: Different set shapes used in set-membership estimation.

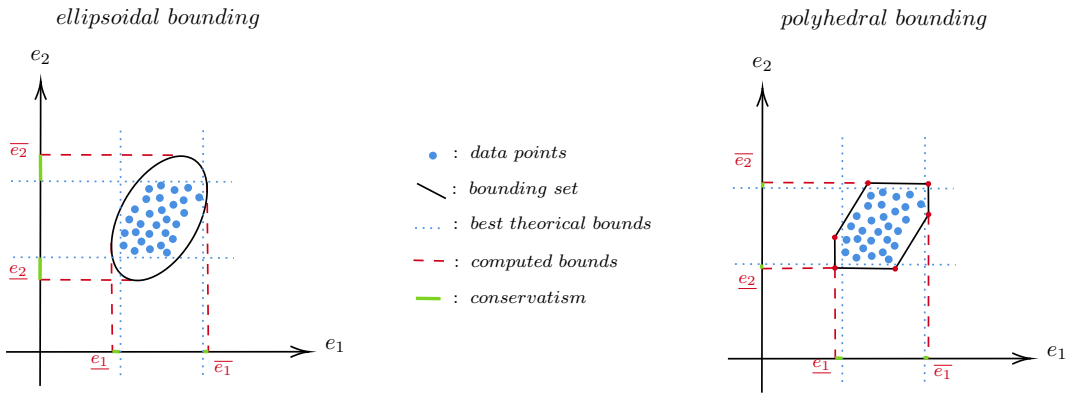

Figure 4.2: Conservatism of ellipsoidal and polyhedral bounding. Here the conservatism (in green) of the ellipsoidal bounding is larger than the one of the polyhedral bounding, especially on the e_2 axis.

4.1.3 Explicit Error Bounds Set-Membership observer

In 2018, a novel set-membership observer design approach was proposed as part of the Ph.D thesis work of Nassim Loukkas in Gipsa-lab. In this work, a method is proposed in order to design a robust set-membership observer for Linear Time Invariant (LTI) and Linear Parameter Varying (LPV) systems undergoing state and output disturbances. A robust gain for the state observer is computed using the Bounded Real Lemma (BRL) and bounds on the estimation error are derived from ellipsoidal invariant sets. Even though this method is part of the previously mentioned set-membership approaches, it stands out by the fact that it is based solely on the solution of an *offline* optimization problem and is implemented similarly to a classical Luenberger state observer, reducing greatly the computational burden compared to the classical set-membership approaches. In the following, an overview of the method is given as well as an illustration of its performances based on a numerical example. The proof of the theorems are omitted since they are found in the original manuscript.

4.1.3.1 Problem statement

The approach is designed for discrete time LTI and LPV systems of the following form :

Authors	Year	Set Shape
Schweppe et al. [41]	1968	Ellipsoids
Bertsekas et al. [4]	1971	Ellipsoids
Spathopoulos et al. [45]	1996	Polyhedrons
Chisci et al. [10]	1996	Paralellotopes
Savkin et al. [40]	1998	Ellipsoids
El Ghaoui et al. [14]	2001	Ellipsoids
Durieu et al. [12]	2001	Ellipsoids
Rakovic et al. [38]	2004	Polyhedrons
Alamo et al. [1]	2005	Zonotopes
Becis-Aubry et al. [3]	2008	Ellipsoids
Chabane et al. [7]	2014	Ellipsoids
Combastel et al. [11]	2015	Zonotopes
Shen et al. [44]	2018	Ellipsoids / Paralellotopes

Table 4.1: Set-membership approaches in the literature.

$$\left\{ \begin{array}{rcl} \mathbf{x}_{k+1} & = & \mathbf{A}(\boldsymbol{\rho}_k)\mathbf{x}_k + \mathbf{B}(\boldsymbol{\rho}_k)\mathbf{u}_k + \mathbf{F}(\boldsymbol{\rho}_k)\mathbf{d}_k \\ \mathbf{y}_k & = & \mathbf{C}\mathbf{x}_k + \mathbf{Z}\mathbf{v}_k \end{array} \right. \tag{4.1}$$

with $\mathbf{x}_k \in \mathbb{R}^n$ the state of the system at instant k, $\mathbf{u}_k \in \mathbb{R}^m$ the input of the system at instant k and $\mathbf{y}_k \in \mathbb{R}^p$ the output of the system at instant k. The system is affected by state and output disturbances $\mathbf{d}_k \in \mathbb{R}^{n_d}$ and $\mathbf{v}_k \in \mathbb{R}^{n_v}$ respectively. Matrices $\mathbf{A}$, $\mathbf{B}$ and $\mathbf{F}$ depend on a parameter vector $\boldsymbol{\rho}_k \in \mathbb{R}^L$ in an *affine fashion*, which is supposed to be known at all time. In the LTI case $\boldsymbol{\rho}_k$ is supposed constant, and in the LPV case it is supposed time-varying and perfectly measured. Matrices $\mathbf{A}$, $\mathbf{B}$, $\mathbf{F}$, $\mathbf{C}$ and $\mathbf{Z}$ have appropriate dimensions and the pair $(\mathbf{A}, \mathbf{C})$ is supposed observable for any values of the parameter $\boldsymbol{\rho}_k$.

The goal of the design strategy is to find a robust parameter observer gain $\mathbf{L}(\boldsymbol{\rho}_k) \in \mathbb{R}^{n \times p}$ in the LPV case (and $\mathbf{L}$ in the LTI case) and estimation error bounds $\bar{\mathbf{e}}$ so that the following state-observer is performed :

$$\hat{\mathbf{x}}_{k+1} = (\mathbf{A}(\boldsymbol{\rho}_k) - \mathbf{L}(\boldsymbol{\rho}_k)\mathbf{C})\hat{\mathbf{x}}_k + \mathbf{B}(\boldsymbol{\rho}_k)\mathbf{u}_k + \mathbf{L}(\boldsymbol{\rho}_k)\mathbf{y}_k \tag{4.2}$$

and such that $\mathbf{x}_k \in [\underline{\mathbf{x}}_k; \bar{\mathbf{x}}_k]$ for all k with $\underline{\mathbf{x}}_k = \hat{\mathbf{x}}_k - \bar{\mathbf{e}}$ and $\bar{\mathbf{x}}_k = \hat{\mathbf{x}}_k + \bar{\mathbf{e}}$.

In the following, the proposed design strategy is described in the general LPV case and illustrated using a numerical LTI system in simulation.

4.1.3.2 1-step design strategy

In this section, the design of the state observer, including the computation of an appropriate observer gain $\mathbf{L}(\boldsymbol{\rho}_k)$ and the computation of estimation error bounds based on ellipsoidal invariant sets, is presented.

The estimation error at time k is defined as follows :

$$\mathbf{e}_k = \mathbf{x}_k - \hat{\mathbf{x}}_k \tag{4.3}$$

Using (4.1) and (4.2), its dynamics are expressed as :

$$\mathbf{e}_{k+1} = \tilde{\mathbf{A}}(\boldsymbol{\rho}_k)\mathbf{e}_k + \mathbf{E}(\boldsymbol{\rho}_k)\mathbf{w}_k \tag{4.4}$$

with $\tilde{\mathbf{A}}(\boldsymbol{\rho}_k) = \mathbf{A}(\boldsymbol{\rho}_k) - \mathbf{L}(\boldsymbol{\rho}_k)\mathbf{C}$, $\mathbf{E}(\boldsymbol{\rho}_k) = \begin{bmatrix}\mathbf{F}(\boldsymbol{\rho}_k) & -\mathbf{L}(\boldsymbol{\rho}_k)\mathbf{Z}\end{bmatrix}$ and $\mathbf{w}_k = \begin{bmatrix}\mathbf{d}_k & \mathbf{v}_k\end{bmatrix}^T$.

In order to perform the state estimation, the dynamics (4.4) must be stable for all values of the scheduling parameter $\boldsymbol{\rho}_k$, and the observer gain $\mathbf{L}(\boldsymbol{\rho}_k)$ must ensure a good rejection of both state and output disturbances. To do so, some design hypotheses are proposed :

- *H1 - The scheduling parameter $\boldsymbol{\rho}_k$ is known at all time and takes values in a known polytopic set Ω_ρ.*
- *H2 - There is a known vector $\bar{\mathbf{w}}$ such that $\mathbf{w}_k^T\mathbf{w}_k \leq \bar{\mathbf{w}}^T\bar{\mathbf{w}}$ for all instant k.*

1) Computation of the punctual state observer robust gain

The hypothesis *H1* is useful in order to compute a valid observer $\mathbf{L}(\boldsymbol{\rho}_k)$ for all the possible values of the scheduling parameter. Indeed, it is known that for affine LPV systems (i.e. for LPV systems whose matrices depend affinely on the scheduling parameter) the following proposition holds [8] :

Proposition 4.1. *Consider the LPV system (4.1), for a given scheduling parameter $\boldsymbol{\rho} \in \Omega_\rho$, there exists a column vector $\boldsymbol{\alpha} \in \mathbb{R}^N$, formed by positive scalar elements $\alpha_i \geq 0$, $\{1, \ldots, N\}$ such that :*

$$\begin{bmatrix}\boldsymbol{\theta}_1^T & \boldsymbol{\theta}_2^T & \cdots & \boldsymbol{\theta}_N^T \\ 1 & 1 & \cdots & 1\end{bmatrix}\boldsymbol{\alpha} = \begin{bmatrix}\boldsymbol{\rho} \\ 1\end{bmatrix} \tag{4.5}$$

where the row vectors $\boldsymbol{\theta}_i \in \mathbb{R}^{1\times L}$, are the a priori known vertices of the polytopic set $\Omega_\rho \subset \mathbb{R}^L$. □

This proposition implies that the matrices of an LPV system can be expressed as a convex combination of the vertex matrices, which are computed at the vertex values $\boldsymbol{\theta}_i$ of the scheduling parameter. In other words, any matrix $\mathbf{M}(\boldsymbol{\rho})$ can be expressed as :

$$\mathbf{M}(\boldsymbol{\rho}) = \sum_{i=1}^{N} \alpha_i \mathbf{M}_i \tag{4.6}$$

with $\mathbf{M}_i = \mathbf{M}(\boldsymbol{\theta}_i)$.

The equation (4.6) is called the *polytopic decomposition* of the matrix $\mathbf{M}$. In this decomposition, the value of $\boldsymbol{\alpha}$ at instant k, $\boldsymbol{\alpha}_k$, depends on the value of the scheduling parameter $\boldsymbol{\rho}$ at instant k, $\boldsymbol{\rho}_k$. An illustration in the 2 dimensional case is presented in Fig. 4.3. This decomposition is very useful for the design of the observer since its convexity property implies that a state observer gain stabilizing each of the vertex dynamics will stabilize the LPV state observer on the whole set of variation of the scheduling parameter Ω_ρ. This property is called the *vertex property* and was defined by Apkarian and colleagues in [2].

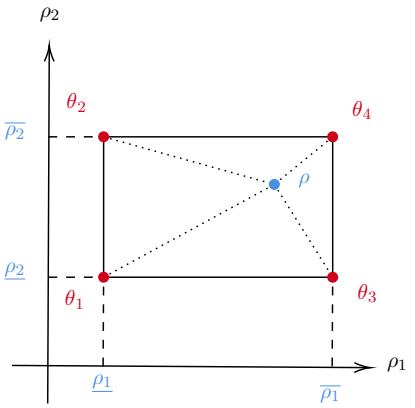

$$\alpha_1 = \left(\frac{\rho_1 - \overline{\rho_1}}{\underline{\rho_1} - \overline{\rho_1}}\right)\left(\frac{\rho_2 - \overline{\rho_2}}{\underline{\rho_2} - \overline{\rho_2}}\right)$$

$$\alpha_2 = \left(\frac{\rho_1 - \overline{\rho_1}}{\underline{\rho_1} - \overline{\rho_1}}\right)\left(\frac{-\rho_2 + \overline{\rho_2}}{\underline{\rho_2} - \overline{\rho_2}}\right)$$

$$\alpha_3 = \left(\frac{-\rho_1 + \rho_1}{\underline{\rho_1} - \overline{\rho_1}}\right)\left(\frac{\rho_2 - \overline{\rho_2}}{\underline{\rho_2} - \overline{\rho_2}}\right)$$

$$\alpha_4 = \left(\frac{-\rho_1 + \rho_1}{\underline{\rho_1} - \overline{\rho_1}}\right)\left(\frac{-\rho_2 - \rho_2}{\underline{\rho_2} - \overline{\rho_2}}\right)$$

$$\rho = \alpha_1 \times \theta_1 + \alpha_2 \times \theta_2 + \alpha_3 \times \theta_3 + \alpha_4 \times \theta_4$$

Figure 4.3: Polytopic decomposition, a 2 dimensional example.

Thus, in order to stabilize the estimation error dynamics (4.4), a parameter dependent observer gain $\mathbf{L}(\boldsymbol{\rho}_k)$ can be found by stabilizing each of the vertex dynamics. To do so, a design strategy based on the Bounded Real Lemma (BRL) is proposed. It consists in finding a quadratic Lyapunov function $\mathbf{V}(\mathbf{e}_k) = \mathbf{e}_k^T \mathbf{P} \mathbf{e}_k$ with matrix $\mathbf{P}$ symmetric positive definite, stabilizing each vertex of the polytopic decomposition of (4.4). Furthermore, this Lyapunov function is chosen so that the following *dissipation inequality* is ensured :

$$\mathbf{V}(\boldsymbol{e}_{k+1}) - \mathbf{V}(\boldsymbol{e}_k) \leq -\boldsymbol{e}_k^T \mathbf{Q} \boldsymbol{e}_k + \gamma^2 \mathbf{w}_k^T \mathbf{w}_k \tag{4.7}$$

Such Lyapunov function is computed by solving N Linear Matrix Inequalities (LMI), with N being the number of vertices of the polytopic decomposition.

The LMI to be solved is defined in the following theorem :

Theorem 1. *Consider the system (4.4) and a given matrix* $\mathbf{Q} \succ 0$. *The observer gains* $\mathbf{L}_i$ *which minimize the* $\mathcal{H}_\infty$ *norm of the system (4.4) are found if there exist a symmetric positive definite matrix* $\mathbf{P}$, *a positive scalar* $\gamma \geq 0$ *and matrices* $\mathbf{U}_i$ *satisfying the following condition :*

$$\begin{pmatrix} -\boldsymbol{P}+\boldsymbol{Q} & 0_{n\times m} & \boldsymbol{A}_i{}^T\boldsymbol{P}-\boldsymbol{C}^T\boldsymbol{U}_i{}^T \\ \star & -\gamma^2\boldsymbol{I}_m & \left[\boldsymbol{P}\boldsymbol{F}_i \quad -\boldsymbol{U}_i\boldsymbol{Z}\right]^T \\ \star & \star & -\boldsymbol{P} \end{pmatrix} \preceq 0 \tag{4.8}$$

for $i = \{1, \ldots, N\}$*. Moreover, the observer matrices can be obtained as :*

$$\mathbf{L}_i = \mathbf{P}^{-1}\mathbf{U}_i \tag{4.9}$$

and the observer gain matrix :

$$\mathbf{L}(\boldsymbol{\rho}_k) = \sum_{i=1}^{N} \alpha_i \mathbf{L}_i \tag{4.10}$$

□

In the previous theorem, the scalar γ corresponds to the $\mathcal{H}_\infty$ performance criterion which quantifies the disturbances rejection of the state observer and we have :

$$\frac{\|\mathbf{e}_k\|_2^2}{\|\mathbf{w}_k\|_2^2} \leq \gamma^2 \tag{4.11}$$

Solving an LMI is an optimization problem and in this case γ can be seen as the cost to be minimized in order to ensure the lowest gain possible between the disturbances and the estimation error.

One can notice that the matrix $\mathbf{P}$, matrices $\mathbf{U}_i$ and scalar γ, solutions of the previous LMI, all depend on the design choice of the symmetric definite positive matrix $\mathbf{Q}$. In practice such matrix can easily be defined as $\mathbf{Q} = \mathbf{G}\mathbf{G}^T$ with $\mathbf{G} \in \mathbb{R}^n$ an arbitrary vector. The relationship between the matrix $\mathbf{Q}$ and the definition of the invariant sets used to derive the estimation error bounds is explained later in the section and is illustrated in Section 4.1.3.4.

After this LMI is solved, the robust observer gain stabilizing the estimation error dynamics (4.4) is chosen, but the estimation error bounds $\bar{\mathbf{e}}$ still need to be defined.

2) Computation of the estimation error bounds

As mentioned previously, the estimation error bounds are derived from ellipsoidal invariant sets computed for the observer. Before defining such invariant sets, some basic definitions and properties of ellipsoidal geometry and invariant sets theory are recalled.

Definition 4.1.1 (Ellipsoidal set)**.** *Let* $\mathbf{P} \in \mathbb{R}^{n\times n}$ *be a symmetric positive definite matrix and* $r \in \mathbb{R}$ *a scalar, then the set*

$$\Psi_P = \left\{\mathbf{x} \in \mathbb{R}^n | \mathbf{x}^T \mathbf{P} \mathbf{x} \leq r\right\} \tag{4.12}$$

defines the interior of an ellipsoid centered on 0. *The matrix* $\mathbf{P}$ *is called the shape matrix of the ellipsoid. In the special case where* $\mathbf{P} = \lambda \mathbf{I}_n$ *with* $\lambda \in \mathbb{R}^*$ *the set* Ψ_P *is a centered ball.*

□

Definition 4.1.2 (Orthogonal Projection)**.** *Let* $\mathbf{P} \in \mathbb{R}^{n \times n}$ *be a symmetric positive definite matrix and* $r \in \mathbb{R}$ *a scalar and define the ellipsoid* Ψ_P *as described in Definition 4.1.1. Let* $y \in \Psi_P$ *a vector belonging to the ellipsoid* Ψ_P. *Define* $\bar{x} = diag\left(\left(\frac{\mathbf{P}}{r}\right)^{-1/2}\right)$. *Then we have*

$$-\bar{x}_i \leq y_i \leq \bar{x}_i \tag{4.13}$$

for $i = \{1, \ldots, n\}$.

The intervals defined by $\bar{x}$ *frame the ellipsoid* Ψ_P *and define lower and upper bounds on each coordinate of the space for any elements* y *in* Ψ_P.

Definition 4.1.3 (Ellipsoid Inclusion)**.** *Let* $r \in \mathbb{R}$ *a nonzero scalar. Let* $\mathbf{P} \in \mathbb{R}^{n \times n}$ *be a symmetric positive definite matrix. Let* $\mathcal{B}_r = \left\{\mathbf{x} \in \mathbb{R}^n | \mathbf{x}^T \mathbf{I}_n \mathbf{x} \leq r\right\}$ *be the centered ball of radius* $\sqrt{r}$. *Let* $\Psi_P = \left\{\mathbf{x} \in \mathbb{R}^n | \mathbf{x}^T \mathbf{P} \mathbf{x} \leq \lambda_{max}(\mathbf{P}) r\right\}$. *Then* Ψ_P *is the smallest centered ellipsoid with shape matrix* $\mathbf{P}$ *including the ball* $\mathcal{B}_r$.

Definition 4.1.4 (Positive Invariant Set)**.** *A set* $\mathcal{S}$ *is a positive invariant set for the dynamic system* $\mathbf{x}_{k+1} = f(\mathbf{x}_k)$ *if*

$$\forall \mathbf{x}_k \in \mathcal{S}, f(\mathbf{x}_k) \in \mathcal{S}$$

Definition 4.1.5 (Robustly Positive Invariant Set)**.** *A set* $\mathcal{S}$ *is a robustly positive invariant set for the dynamic system* $\mathbf{x}_{k+1} = f(\mathbf{x}_k, w_k)$ *with* $w \in \mathcal{W}$ *an exogenous signal, if*

$$\forall \mathbf{x}_k \in \mathcal{S} \text{ and } \forall \mathbf{w}_k \in \mathcal{W}, f(\mathbf{x}_k, \mathbf{w}_k) \in \mathcal{S}$$

In order to define an ellipsoidal invariant set for the estimation error of the observer, the variables $\mathbf{P}$, $\mathbf{Q}$, λ and γ obtained after the computation of the observer gain are used.

As mentioned previously the Lyapunov function solution of the LMI (4.8) respects the dissipation inequality (4.7), thus :

$$\mathbf{V}(\boldsymbol{e}_{k+1}) - \mathbf{V}(\boldsymbol{e}_k) \leq -\boldsymbol{e}_k^T \mathbf{Q} \boldsymbol{e}_k + \gamma^2 \mathbf{w}_k^T \mathbf{w}_k \tag{4.14}$$

By using hypothesis *H2*, we have :

$$\mathbf{V}(\boldsymbol{e}_{k+1}) - \mathbf{V}(\boldsymbol{e}_k) \leq -\boldsymbol{e}_k^T \mathbf{Q} \boldsymbol{e}_k + \gamma^2 \bar{\mathbf{w}}^T \bar{\mathbf{w}} \tag{4.15}$$

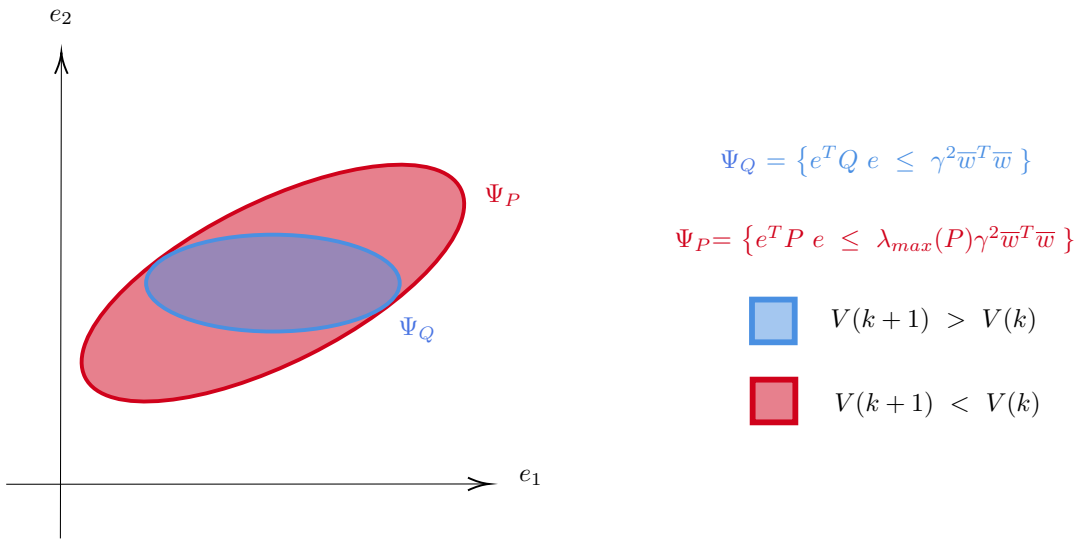

Figure 4.4: Evolution of the Lyapunov function in the state space.

From here, it is possible to define the following ellipsoid $\Psi_Q = \left\{\mathbf{e}_k \in \mathbb{R}^n | \mathbf{e}_k^T \mathbf{Q} \mathbf{e}_k \leq \gamma^2 \bar{w}^T \bar{w}\right\}$. One can notice that outside of Ψ_Q we have $-\mathbf{e}_k^T \mathbf{Q} \mathbf{e}_k + \gamma^2 \bar{w}^T \bar{w} \leq 0$ which implies a decrease in the Lyapunov function $\mathbf{V}$. Thus, any level set of the Lyapunov function $\mathbf{V}$ containing Ψ_Q is a robustly positive invariant set for the estimation errors of the state observer. An illustration is given in Fig. 4.4.

Based on this property, Loukkas proved the following theorem in order to derive a Robustly Positive Invariant (RPI) set for the state estimation error :

Theorem 2. *Consider the system (4.4) with bounded disturbances. If there exist a common symmetric positive definite matrix* $\mathbf{P}$ *and a scalar* $\gamma \geq 0$*, for a given matrix* $\mathbf{Q}$ *verifying the condition (4.8), then the following set* Ψ_P *is an RPI set for system (4.4) :*

$$\Psi_P = \left\{\mathbf{e}_k \in \mathbb{R}^n | \mathbf{e}_k^T \mathbf{P} \mathbf{e}_k \leq \frac{1}{\lambda} \gamma^2 \bar{w}^T \bar{w}\right\} \tag{4.16}$$

where, for a given non-zero vector $\mathbf{e}_k$*, the scalar* $\lambda \geq 0$ *satisfies :*

$$\lambda \leq \frac{\mathbf{e}_k^T \mathbf{Q} \mathbf{e}_k}{\mathbf{e}_k^T \mathbf{P} \mathbf{e}_k} \leq 1 \tag{4.17}$$

In practice, the scalar λ can be chosen as the minimum generalized eigenvalue of the pair $(\mathbf{Q}, \mathbf{P})$.

Theorem 2 shows that using the variables $\mathbf{Q}$, $\mathbf{P}$, γ and $\bar{\mathbf{w}}$ from the computation of the observer gain, it is possible to express an ellipsoidal invariant set Ψ_P for the state estimation errors. Then, using the projection property of ellipsoids of Definition 4.1.2, it is possible to define deterministic confidence intervals on the estimation error :

$$-\bar{\mathbf{e}} \leq \mathbf{e}_k \leq \bar{\mathbf{e}} \tag{4.18}$$

with $\bar{\mathbf{e}} = diag\left(\left(\frac{\mathbf{P}}{\frac{1}{\lambda}\gamma^2\bar{\mathbf{w}}^T\bar{\mathbf{w}}}\right)^{-1/2}\right)$.

A summary of the 1-step synthesis is given in Algorithm 1.

Algorithm 1 $\mathcal{H}_\infty$ set-membership observer design for LPV systems (1-step synthesis)

Require: Matrices $\mathbf{A}_i, \mathbf{B}_i, \mathbf{F}_i$, for $i = \{1, \ldots, N\}$, $\mathbf{C}$ and $\mathbf{Z}$ describing system (4.1).
  Initialize design matrix $\mathbf{Q}$.
  for `<i=1 to i=N>` **do**
    Find matrices $\mathbf{P}, \mathbf{U}_i$ and the minimum γ satisfying LMI (4.8).
    Compute $\mathbf{L}_i = \mathbf{P}^{-1}\mathbf{U}_i$.
    Compute $\tilde{\mathbf{A}}_i = \mathbf{A}_i - \mathbf{L}_i\mathbf{C}$.
    Compute $\mathbf{E}_i = \begin{bmatrix}\mathbf{F}_i & -\mathbf{L}_i\mathbf{Z}\end{bmatrix}$.
  end for
  Compute $\mathbf{L}_i = \mathbf{P}^{-1}\mathbf{U}_i$.
  Compute $\bar{\mathbf{e}} = diag\left(\left(\frac{\mathbf{P}}{\frac{1}{\lambda}\gamma^2\bar{\mathbf{w}}^T\bar{\mathbf{w}}}\right)^{-1/2}\right)$.

4.1.3.3 2-steps design strategy

In the previous section, we showed that for a given system and a *given matrix* $\mathbf{Q}$, a state observer gain and estimation error bounds can be computed by solving one or several Linear Matrix Inequalities (LMI). In this section, a heuristic proposed by Loukkas in order to choose a good candidate for the matrix $\mathbf{Q}$ is described.

The heuristic proposed by Loukkas is based on the *multivariate Chebyshev inequality*. Initially proposed in 1867 by Chebyshev for the monovariate case, this inequality was recently extended to the multivariate case in [46]. This inequality is stated as follows :

Theorem 3. *Let $\boldsymbol{\xi} \in \mathbb{R}^{n_\xi}$ be a random vector variable of covariance matrix $\boldsymbol{\Sigma}$ and mean $\boldsymbol{\mu}$. Let $\lambda \in \mathbb{R}^*$ a nonzero scalar. Then :*

$$\mathcal{P}\left((\boldsymbol{\xi} - \boldsymbol{\mu})^T\boldsymbol{\Sigma}^{-1}(\boldsymbol{\xi} - \boldsymbol{\mu}) \geq \lambda^2\right) \leq min\left\{1, \frac{n_\xi}{\lambda^2}\right\} \tag{4.19}$$

with $\mathcal{P}$ the probability measure on $\mathbb{R}^{n_\xi}$.

Theorem 3 states that, for a given random variable $\boldsymbol{\xi}$ and a given nonzero scalar λ, the probability that a realization $\boldsymbol{\xi}_k$ of $\boldsymbol{\xi}$ exits the ellipsoid $\Psi_\Sigma = \left\{\boldsymbol{\xi} \in \mathbb{R}^{n_\xi} | \boldsymbol{\xi}^T\boldsymbol{\Sigma}^{-1}\boldsymbol{\xi} \geq \lambda^2\right\}$ is bounded by $\frac{n_\xi}{\lambda^2}$. The shape of the ellipsoid Ψ_Σ is defined by the covariance matrix $\boldsymbol{\Sigma}$, and its size by the scalar λ. From Theorem 3 it can be noticed that the larger the value of λ, the smaller is the probability that the realization exits the ellipsoid Ψ_Σ.

As such, Ψ_Σ is not an invariant set for $\boldsymbol{\xi}$ but the idea of the heuristic proposed by Loukkas is to choose the design matrix $\mathbf{Q}$ equal to the inverse of the covariance matrix $\boldsymbol{\Sigma}^{-1}$ in order to take the distribution of the estimation error into account when shaping the ellipsoidal invariant set $\boldsymbol{\Psi}_P$.

In order to compute such covariance matrix for the estimation error dynamics (4.4), a result from [30] is used. This paper states that for a discrete-time system $\mathbf{x}_{k+1} = \mathbf{A}\mathbf{x}_k + \mathbf{w}_k$, affected by a zero-mean white random sequence $\mathbf{w}$ of covariance matrix $\boldsymbol{\Sigma}_w = \boldsymbol{\Sigma}_w^T \succ 0$, the covariance matrix of the state vector $\boldsymbol{\Sigma}_x$ can be recovered by solving the following Lyapunov equation :

$$\boldsymbol{\Sigma}_x = \mathbf{A}\boldsymbol{\Sigma}_x\mathbf{A}^T + \boldsymbol{\Sigma}_w \tag{4.20}$$

In the heuristic, Loukkas proposed to apply this method to the estimation error dynamics (4.4), by solving the following Lyapunov equation for each vertex of the polytopic decomposition :

$$\boldsymbol{\Sigma}_{ei} = \tilde{\mathbf{A}}_i\boldsymbol{\Sigma}_{ei}\tilde{\mathbf{A}}_i^T + \mathbf{E}_i\boldsymbol{\Sigma}_{wi}\mathbf{E}_i^T \tag{4.21}$$

Because $\tilde{\mathbf{A}} = \mathbf{A} - \mathbf{L}\mathbf{C}$, a first synthesis needs to be performed in order to compute a temporary observer gain $\mathbf{L}$ by solving LMI (4.8) using $\mathbf{Q} = \mathbf{I}_n$.

In the considered case, $\mathbf{w}$ is a uniform disturbance belonging to the interval $[-\bar{\mathbf{w}}; \bar{\mathbf{w}}]$, thus its covariance matrix is chosen as $\boldsymbol{\Sigma}_w = var(\mathbf{w}) = \frac{1}{12}(\bar{\mathbf{w}} - (-\bar{\mathbf{w}}))^2\mathbf{I}_n$. The covariance matrix of the estimation error is then computed as an average of the vertex covariance matrices :

$$\boldsymbol{\Sigma}_e = \frac{1}{N}\sum_{i=1}^{N}\boldsymbol{\Sigma}_{ei} \tag{4.22}$$

Finally, an observer synthesis is performed by solving LMI (4.8) using $\mathbf{Q} = \boldsymbol{\Sigma}_e^{-1}$.

A summary of the 2-steps synthesis is given in Algorithm 2.

4.1.3.4 Illustration using a numerical LTI system in simulation

In order to illustrate the observer design strategy, the following disturbed discrete-time LTI system is considered :

$$\left\{\begin{array}{rcl} \mathbf{x}_{k+1} & = & \mathbf{A}\mathbf{x}_k + \mathbf{B}\mathbf{u}_k + \mathbf{F}\mathbf{d}_k \\ \mathbf{y}_k & = & \mathbf{C}\mathbf{x}_k + \mathbf{Z}\mathbf{v}_k \end{array}\right. \tag{4.23}$$

with :

$$\mathbf{A} = \begin{pmatrix} 0.2 & 0.2 \\ 0 & 0.5 \end{pmatrix}, \mathbf{B} = \begin{pmatrix} 1 \\ 1 \end{pmatrix}, \mathbf{F} = \begin{pmatrix} 0 \\ 0.1 \end{pmatrix}, \mathbf{C} = \begin{pmatrix} 1 & 0 \end{pmatrix}, \mathbf{Z} = 0.1 \tag{4.24}$$

Algorithm 2 $\mathcal{H}_\infty$ set-membership observer design for LPV systems (2-steps synthesis)

Require: Matrices $\mathbf{A}_i, \mathbf{B}_i, \mathbf{F}_i$, for $i = \{1, \ldots, N\}$, $\mathbf{C}$ and $\mathbf{Z}$ describing system (4.1). Disturbance covariance matrix $\mathbf{\Sigma}_w$.
Initialize design matrix $\mathbf{Q}$ to $\mathbf{I}_n$.
for `<i=1 to i=N>` **do**
Find matrices $\mathbf{P}, \mathbf{U}_i$ and the minimum γ satisfying LMI (4.8).
Compute $\mathbf{L}_i = \mathbf{P}^{-1}\mathbf{U}_i$.
Compute $\tilde{\mathbf{A}}_i = \mathbf{A}_i - \mathbf{L}_i\mathbf{C}$.
Compute $\mathbf{E}_i = \begin{bmatrix}\mathbf{F}_i & -\mathbf{L}_i\mathbf{Z}\end{bmatrix}$.
end for
for `<i=1 to i=L>` **do**
Compute $\mathbf{\Sigma}_{ei}$ by solving (4.21).
end for
Compute the average covariance matrix $\mathbf{\Sigma}_e$ as in (4.22).
Define $\mathbf{Q} = \mathbf{\Sigma}_e^{-1}$.
for `<i=1 to i=N>` **do**
Find matrices $\mathbf{P}, \mathbf{U}_i$ and the minimum γ satisfying LMI (4.8).
Compute $\mathbf{L}_i = \mathbf{P}^{-1}\mathbf{U}_i$.
Compute $\bar{\mathbf{e}} = diag\left(\left(\frac{\mathbf{P}}{\frac{1}{\lambda}\gamma^2\bar{\mathbf{w}}^T\bar{\mathbf{w}}}\right)^{-1/2}\right)$.

The state and output disturbances vector $\mathbf{w}_k = \begin{pmatrix} d_k & v_k \end{pmatrix}^T$ is supposed to be bounded by $\bar{\mathbf{w}} = \begin{pmatrix} 1 & 1 \end{pmatrix}^T$ so that for all k we have :

$$\mathbf{w}_k^T\mathbf{w}_k \leq \bar{\mathbf{w}}^T\bar{\mathbf{w}} \tag{4.25}$$

1) Influence of the initialization of $\mathbf{Q}$

First, the influence of the choice of the design matrix $\mathbf{Q}$ is illustrated by comparing the shape of the sets Ψ_Q and Ψ_P for different matrices $\mathbf{Q}$ after applying the 1-step synthesis.

Three different matrices $\mathbf{Q}$ are considered :

$$\mathbf{Q}_I = \begin{pmatrix} 1 & 0 \\ 0 & 1 \end{pmatrix}, \mathbf{Q}_{10I} = \begin{pmatrix} 10 & 0 \\ 0 & 10 \end{pmatrix}, \mathbf{Q}_{101} = \begin{pmatrix} 10 & 0 \\ 0 & 1 \end{pmatrix}$$

A comparison between the sets Ψ_Q and Ψ_P is showed in Fig. 4.5. One can notice that the value chosen for the coefficients of $\mathbf{Q}$ have an influence on the size and the shape of the sets Ψ_Q and Ψ_P. It is thus important to choose $\mathbf{Q}$ so that the sets Ψ_Q and Ψ_P are adapted to the distribution of the estimation errors.

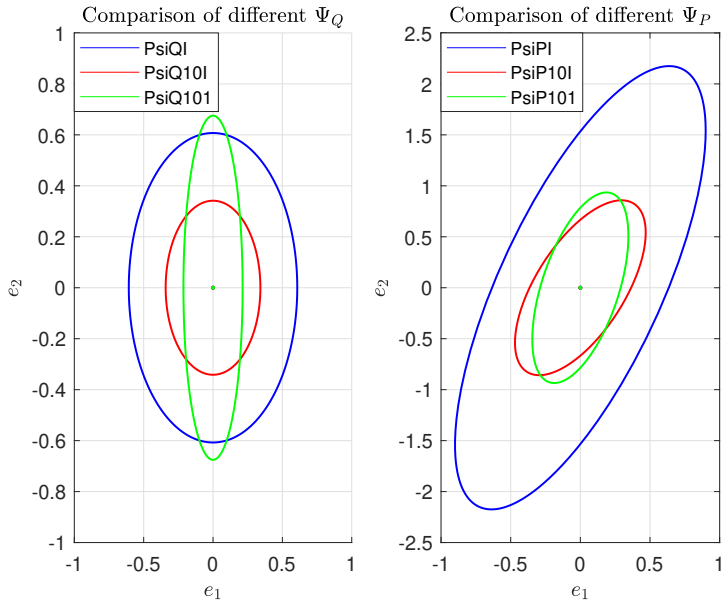

Figure 4.5: Comparison of different sets Ψ_Q and Ψ_P based on different matrices $\mathbf{Q}$ for the 1-step synthesis.

2) Comparison of the 1-step and 2-steps syntheses

Then, the utility of the 2-step synthesis is illustrated by comparing the performances of two observers : the *1-step* observer, computed using the 1-step algorithm, and the *2-step* observer, computed using the 2-step algorithm. In the following, matrices and vectors with sub index 1 relate to the 1-step synthesis, and matrices and vectors with sub index 2 relate to the 2-step synthesis.

The first synthesis is initialized with $\mathbf{Q} = \mathbf{I}_2$. After completing the 1-step algorithm, the following values are returned :

$$\mathbf{P}_1 = \begin{pmatrix} 17.36 & -5.09 \\ -5.09 & 2.97 \end{pmatrix}, \mathbf{L}_1 = \begin{pmatrix} 0.34 \\ 0.65 \end{pmatrix}, \bar{\mathbf{e}}_1 = \begin{pmatrix} 0.39 \\ 0.93 \end{pmatrix}, \gamma_1 = 0.18$$

Then, following the 2-step algorithm, the estimation error covariance matrix is computed :

$$\mathbf{\Sigma}_e = \begin{pmatrix} 0.0006 & 0.0011 \\ 0.0011 & 0.0057 \end{pmatrix}$$

and the following values are returned :

$$\mathbf{P}_2 = \begin{pmatrix} 3.8428 & -0.9585 \\ -0.9585 & 0.5342 \end{pmatrix} 10^3, \mathbf{L}_2 = \begin{pmatrix} 0.32 \\ 0.50 \end{pmatrix}, \bar{\mathbf{e}}_2 = \begin{pmatrix} 0.10 \\ 0.27 \end{pmatrix}, \gamma_2 = 2.43$$

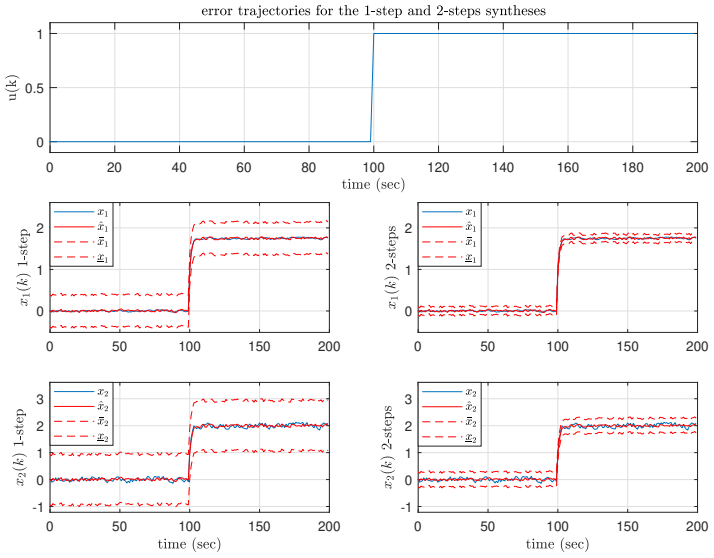

Figure 4.6: Evolution of the system's states, state estimates and estimation error bounds for the 1-step and 2-steps syntheses.

The responses of the two observers are showed in Fig. 4.6. In this simulation, the system is undergoing a step input from $u = 0$ to $u = 1$. The noise signals d and v are generated randomly according to a uniform distribution between -1 and 1 as chosen for the design. The estimation and the estimation error bounds of both the states of the system is showed for the 1-step synthesis and the 2-steps synthesis and are compared to the real state signals.

One can notice that the $\mathcal{H}_\infty$ factor γ is larger for the 2-steps synthesis than for the 1-step synthesis which implies a degradation in the noise to signal gain. However, the estimation bounds after the 2-steps are smaller and thus less conservative. A comparison between the sets Ψ_Q and Ψ_P obtained after the 1-step and 2-steps syntheses is showed in Fig. 4.7. One can notice that after the 2-steps synthesis, the invariant set Ψ_P is much more adapted to the actual distribution of the estimation error.

4.2 Robust Set-Membership observer for respiratory gas exchange estimation

In the previous section, the set-membership observer proposed by Loukkas was presented and illustrated. This observer is intended for discrete-time LTI and LPV systems affected by bounded disturbances. In this thesis, an attempt to adapt of the work of Loukkas is proposed in order to extend the usability of such set-membership observer to discrete-time LTI and LPV systems affected by bounded disturbances *with parameter dependent output matrix*.

In this section, the derivation of a new LMI condition to achieve state estimation in the

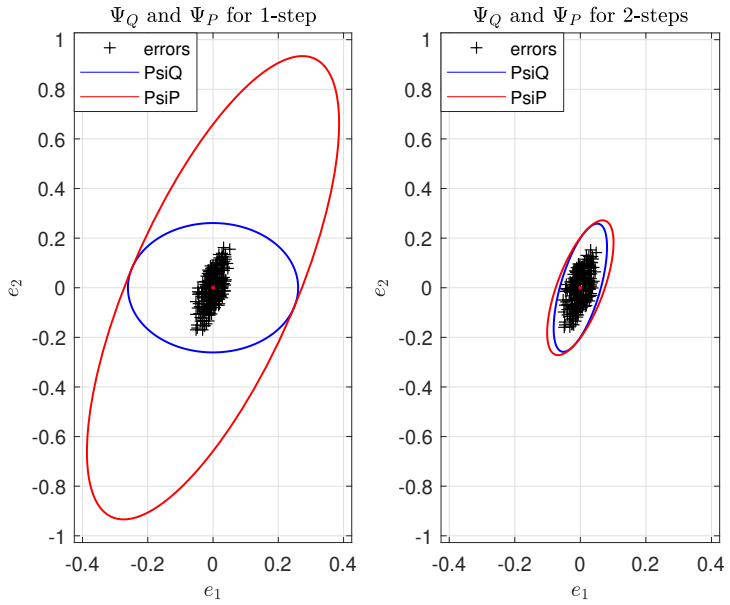

Figure 4.7: Comparison of different sets Ψ_Q and Ψ_P for the 1-step and 2-steps syntheses with an initial matrix based on different matrices $\mathbf{Q} = \mathbf{I}_2$.

context of parameter dependent output is presented. Then, this new design strategy is applied to the problem of estimating respiratory gas exchange during exercise.

4.2.1 Adaptation of the Explicit Error Bounds Set-Membership observer to the parameter dependent output case

4.2.1.1 Problem statement

We consider the following discrete-time disturbed LPV system with parameter-dependant output :

$$\left\{ \begin{array}{rcl} \mathbf{x}_{k+1} & = & \mathbf{A}(\boldsymbol{\rho}_k)\mathbf{x}_k + \mathbf{B}(\boldsymbol{\rho}_k)\mathbf{u}_k + \mathbf{F}(\boldsymbol{\rho}_k)\mathbf{d}_k \\ \mathbf{y}_k & = & \mathbf{C}(\boldsymbol{\rho}_k)\mathbf{x}_k + \mathbf{Z}\mathbf{v}_k \end{array} \right. \tag{4.26}$$

Vectors $\mathbf{x}_k$, $\mathbf{u}_k$, $\mathbf{y}_k$, $\mathbf{d}_k$ and $\mathbf{v}_k$ and matrices $\mathbf{A}(\boldsymbol{\rho}_k)$, $\mathbf{B}(\boldsymbol{\rho}_k)$, $\mathbf{F}(\boldsymbol{\rho}_k)$ and $\mathbf{Z}(\boldsymbol{\rho}_k)$ are defined as in (4.1). We suppose that the output matrix $\mathbf{C}(\boldsymbol{\rho}_k)$ depends on the scheduling parameter $\boldsymbol{\rho}_k$ in an affine fashion.

The goal of the design strategy is to find a *constant* robust parameter observer gain $\mathbf{L} \in \mathbb{R}^{n \times p}$ and estimation error bounds $\bar{\mathbf{e}}$ so that the following state-observer is performed :

$$\hat{\mathbf{x}}_{k+1} = (\mathbf{A}(\boldsymbol{\rho}_k) - \mathbf{L}\mathbf{C}(\boldsymbol{\rho}_k))\hat{\mathbf{x}}_k + \mathbf{B}(\boldsymbol{\rho}_k)\mathbf{u}_k + \mathbf{L}\mathbf{y}_k \tag{4.27}$$

and such that $\mathbf{x}_k \in [\underline{\mathbf{x}}_k; \bar{\mathbf{x}}_k]$ for all k with $\underline{\mathbf{x}}_k = \hat{\mathbf{x}}_k - \bar{\mathbf{e}}$ and $\bar{\mathbf{x}}_k = \hat{\mathbf{x}}_k + \bar{\mathbf{e}}$.

One can notice that compared to (4.2), the output matrix $\mathbf{C}(\boldsymbol{\rho}_k)$ is now depending on the scheduling parameter and the robust observer gain $\mathbf{L}$ is no longer depending on the scheduling parameter. This design choice is explained in the next section.

4.2.1.2 Computation of the punctual state observer robust gain

Similarly to the approach proposed by Loukkas, the punctual state observer robust gain $\mathbf{L}$ is computed by solving a finite number of LMIs corresponding to the stabilization of the vertex estimation error dynamics. However, the dependency of the output matrix $\mathbf{C}(\boldsymbol{\rho}_k)$ to the scheduling parameter does not allow to solve the exact same LMI problem.

Let us recall the LMI (4.8) proposed by Loukkas :

$$\begin{pmatrix} -\mathbf{P}+\mathbf{Q} & 0_{n\times m} & {\mathbf{A}_i}^T\mathbf{P}-\mathbf{C}^T{\mathbf{U}_i}^T \\ \star & -\gamma^2\mathbf{I}_m & \begin{bmatrix}\mathbf{P}\mathbf{F}_i & -\mathbf{U}_i\mathbf{Z}\end{bmatrix}^T \\ \star & \star & -\mathbf{P} \end{pmatrix} \preceq 0 \tag{4.28}$$

using equation (4.9), we can replace $\mathbf{U}_i$ by $\mathbf{P}\mathbf{L}_i$ and we have :

$$\begin{pmatrix} -\mathbf{P}+\mathbf{Q} & 0_{n\times m} & {\mathbf{A}_i}^T\mathbf{P}-\mathbf{C}^T{\mathbf{L}_i}^T\mathbf{P}^T \\ \star & -\gamma^2\mathbf{I}_m & \begin{bmatrix}\mathbf{P}\mathbf{F}_i & -\mathbf{P}\mathbf{L}_i\mathbf{Z}\end{bmatrix}^T \\ \star & \star & -\mathbf{P} \end{pmatrix} \preceq 0 \tag{4.29}$$

One can notice this LMI involves products between matrices $\mathbf{C}$ and $\mathbf{L}$, which implies that only one of them can be depending on the scheduling parameter $\boldsymbol{\rho}$ in order to use the vertex property. Because we are interested in designing a state observer for systems with parameter dependent output, we look for a robust constant observer gain $\mathbf{L}$. The problem to solve is the following :

Theorem 4. *Consider the system (4.4) and a given matrix $\mathbf{Q} \succ 0$. The observer gain $\mathbf{L}$ which minimizes the $\mathcal{H}_\infty$ norm of the system (4.4) is found if there exist a symmetric positive definite matrix $\mathbf{P}$, a positive scalar $\gamma \geq 0$ and matrix $\mathbf{U}$ satisfying the following condition :*

$$\begin{pmatrix} -\boldsymbol{P}+\boldsymbol{Q} & 0_{n\times m} & {\boldsymbol{A}_i}^T\boldsymbol{P}-\boldsymbol{C}_i^T\boldsymbol{U}^T \\ \star & -\gamma^2\boldsymbol{I}_m & \begin{bmatrix}\boldsymbol{P}\boldsymbol{F}_i & -\boldsymbol{U}\boldsymbol{Z}\end{bmatrix}^T \\ \star & \star & -\boldsymbol{P} \end{pmatrix} \preceq 0 \tag{4.30}$$

for $i = \{1, \ldots, N\}$. Moreover, the observer matrix can be obtained as :

$$\mathbf{L} = \mathbf{P}^{-1}\mathbf{U} \tag{4.31}$$

□

Proof. Suppose that there are a quadratic Lyapunov function $\mathbf{V}(\boldsymbol{e}_k) = \boldsymbol{e}_k^T \mathbf{P} \boldsymbol{e}_k$ with $\mathbf{P} = \mathbf{P}^T \succ 0$ a symmetric semi-definite positive matrix, and a positive scalar $\gamma \geq 0$ satisfying the dissipation inequality (4.32) :

$$\mathbf{V}(\boldsymbol{e}_{k+1}) - \mathbf{V}(\boldsymbol{e}_k) \leq -\boldsymbol{e}_k^T \mathbf{Q} \boldsymbol{e}_k + \gamma^2 \mathbf{w}_k^T \mathbf{w}_k \tag{4.32}$$

By definition of $\mathbf{V}$, we have :

$$\boldsymbol{e}_{k+1}^T \mathbf{P} \boldsymbol{e}_{k+1} + \boldsymbol{e}_k^T (-\mathbf{P} + \mathbf{Q}) \boldsymbol{e}_k - \gamma^2 \mathbf{w}_k^T \mathbf{w}_k \leq 0 \tag{4.33}$$

Using the estimation error dynamic equation (4.4), we have :

$$[\tilde{\mathbf{A}}(\boldsymbol{\rho}_k)\mathbf{e}_k + \mathbf{E}(\boldsymbol{\rho}_k)\mathbf{w}_k]^T \mathbf{P} [\tilde{\mathbf{A}}(\boldsymbol{\rho}_k)\mathbf{e}_k + \mathbf{E}(\boldsymbol{\rho}_k)\mathbf{w}_k] + \boldsymbol{e}_k^T (-\mathbf{P} + \mathbf{Q}) \boldsymbol{e}_k - \gamma^2 \mathbf{w}_k^T \mathbf{w}_k \leq 0 \tag{4.34}$$

By developing we have :

$$\begin{aligned} &\mathbf{e}_k^T [\tilde{\mathbf{A}}^T(\boldsymbol{\rho}_k) \mathbf{P} \tilde{\mathbf{A}}(\boldsymbol{\rho}_k) - \mathbf{P} + \mathbf{Q}] \mathbf{e}_k + \mathbf{e}_k^T \tilde{\mathbf{A}}^T(\boldsymbol{\rho}_k) \mathbf{P} \mathbf{E}(\boldsymbol{\rho}_k) \mathbf{w}_k + \\ &\mathbf{w}_k^T \mathbf{E}^T(\boldsymbol{\rho}_k) \mathbf{P} \tilde{\mathbf{A}} \mathbf{e}_k + \mathbf{w}_k^T \mathbf{E}^T(\boldsymbol{\rho}_k) \mathbf{P} \mathbf{E}(\boldsymbol{\rho}_k) \mathbf{w}_k - \gamma^2 \mathbf{w}_k^T \mathbf{w}_k \leq 0 \end{aligned} \tag{4.35}$$

Which is equivalent to :

$$\begin{pmatrix} \mathbf{e}_k^T & \mathbf{w}_k^T \end{pmatrix}^T \begin{pmatrix} \tilde{\mathbf{A}}^T(\boldsymbol{\rho}_k) \mathbf{P} \tilde{\mathbf{A}}(\boldsymbol{\rho}_k) - \mathbf{P} + \mathbf{Q} & \tilde{\mathbf{A}}^T(\boldsymbol{\rho}_k) \mathbf{P} \mathbf{E}(\boldsymbol{\rho}_k) \\ \star & \mathbf{E}^T(\boldsymbol{\rho}_k) \mathbf{P} \mathbf{E}(\boldsymbol{\rho}_k) - \gamma^2 \mathbf{I}_m \end{pmatrix} \begin{pmatrix} \mathbf{e}_k & \mathbf{w}_k \end{pmatrix} \leq 0 \tag{4.36}$$

$$\begin{pmatrix} \tilde{\mathbf{A}}^T(\boldsymbol{\rho}_k) \mathbf{P} \tilde{\mathbf{A}}(\boldsymbol{\rho}_k) - \mathbf{P} + \mathbf{Q} & \tilde{\mathbf{A}}^T(\boldsymbol{\rho}_k) \mathbf{P} \mathbf{E}(\boldsymbol{\rho}_k) \\ \star & \mathbf{E}^T(\boldsymbol{\rho}_k) \mathbf{P} \mathbf{E}(\boldsymbol{\rho}_k) - \gamma^2 \mathbf{I}_m \end{pmatrix} \preceq 0 \tag{4.37}$$

$$\begin{pmatrix} \tilde{\mathbf{A}}^T & \mathbf{E}^T \end{pmatrix}^T \mathbf{P} \begin{pmatrix} \tilde{\mathbf{A}} & \mathbf{E} \end{pmatrix} + \begin{pmatrix} -\mathbf{P} + \mathbf{Q} & 0_{n \times m} \\ \star & -\gamma^2 \mathbf{I}_m \end{pmatrix} \preceq 0 \tag{4.38}$$

Using the Schur complement, we have :

$$\begin{pmatrix} -\mathbf{P} + \mathbf{Q} & 0_{n \times m} & \tilde{\mathbf{A}}^T(\boldsymbol{\rho}_k) \mathbf{P} \\ \star & -\gamma^2 \mathbf{I}_m & \mathbf{E}^T(\boldsymbol{\rho}_k) \mathbf{P} \\ \star & \star & -\mathbf{P} \end{pmatrix} \preceq 0 \tag{4.39}$$

By definition of $\tilde{\mathbf{A}}(\boldsymbol{\rho}_k)$ and $\mathbf{E}(\boldsymbol{\rho}_k)$, we have :

$$\begin{pmatrix} -\mathbf{P} + \mathbf{Q} & 0_{n \times m} & (\mathbf{A}(\boldsymbol{\rho}_k) - \mathbf{L}\mathbf{C}(\boldsymbol{\rho}_k))^T \mathbf{P} \\ \star & -\gamma^2 \mathbf{I}_m & [\mathbf{F}(\boldsymbol{\rho}_k) \; -\mathbf{L}(\boldsymbol{\rho}_k)\mathbf{Z}]^T \mathbf{P} \\ \star & \star & -\mathbf{P} \end{pmatrix} \preceq 0 \tag{4.40}$$

By developing and posing $\mathbf{U} = \mathbf{P}\mathbf{L}$, we have :

$$\begin{pmatrix} -\mathbf{P}+\mathbf{Q} & 0_{n\times m} & \mathbf{A}^T(\boldsymbol{\rho}_k)\mathbf{P}-\mathbf{C}^T(\boldsymbol{\rho}_k)\mathbf{U}^T \\ \star & -\gamma^2\mathbf{I}_m & \begin{bmatrix}\mathbf{P}\mathbf{F}(\boldsymbol{\rho}_k) & -\mathbf{U}\mathbf{Z}\end{bmatrix}^T \\ \star & \star & -\mathbf{P} \end{pmatrix} \preceq 0 \tag{4.41}$$

And finally, using the vertex property, we have :

$$\begin{pmatrix} -\mathbf{P}+\mathbf{Q} & 0_{n\times m} & {\mathbf{A}_i}^T\mathbf{P}-\mathbf{C}_i^T\mathbf{U}^T \\ \star & -\gamma^2\mathbf{I}_m & \begin{bmatrix}\mathbf{P}\mathbf{F}_i & -\mathbf{U}\mathbf{Z}\end{bmatrix}^T \\ \star & \star & -\mathbf{P} \end{pmatrix} \preceq 0 \tag{4.42}$$

□

A similar 2-steps strategy can be used in order to reduce the conservatism of the solution.

The adapted design steps are presented in Algorithm 3.

Algorithm 3 $\mathcal{H}_\infty$ set-membership observer design for LPV systems with parameter dependant output (2-steps synthesis)

Require: Matrices $\mathbf{A}_i, \mathbf{B}_i, \mathbf{F}_i, \mathbf{C}_i$ for $i = \{1, \ldots, N\}$, and matrix $\mathbf{Z}$ describing system (4.26).
Disturbance covariance matrix $\boldsymbol{\Sigma}_w$.
Initialize design matrix $\mathbf{Q}$ to $\mathbf{I}_n$.
for `<i=1 to i=N>` **do**
Find matrices $\mathbf{P}, \mathbf{U}_i$ and the minimum γ satisfying LMI (4.30).
Compute $\mathbf{L} = \mathbf{P}^{-1}\mathbf{U}$.
Compute $\tilde{\mathbf{A}}_i = \mathbf{A}_i - \mathbf{L}\mathbf{C}_i$.
Compute $\mathbf{E}_i = \begin{bmatrix}\mathbf{F}_i & -\mathbf{L}\mathbf{Z}\end{bmatrix}$.
end for
for `<i=1 to i=L>` **do**
Compute $\boldsymbol{\Sigma}_{ei}$ by solving (4.21).
end for
Compute the average covariance matrix $\boldsymbol{\Sigma}_e$ as in (4.22).
Define $\mathbf{Q} = \boldsymbol{\Sigma}_e^{-1}$.
for `<i=1 to i=N>` **do**
Find matrices $\mathbf{P}, \mathbf{U}$ and the minimum γ satisfying LMI (4.30).
Compute $\mathbf{L} = \mathbf{P}^{-1}\mathbf{U}$.
Compute $\bar{\mathbf{e}} = diag\left(\left(\frac{\mathbf{P}}{\frac{1}{\lambda}\gamma^2\bar{\mathbf{w}}^T\bar{\mathbf{w}}}\right)^{-1/2}\right)$.

4.2.2 Estimation of respiratory gas exchange during exercise

4.2.2.1 Problem statement

In Chapter 3, the respiratory gas exchange model proposed by Rosero was introduced :

$$\begin{cases} \mathbf{x}_{k+1} &= \mathbf{A}\mathbf{x}_k + \mathbf{B}u_k + \mathbf{B}w_0 \\ \mathbf{y}_k &= \mathbf{C}(\rho_k)\mathbf{x}_k \end{cases} \tag{4.43}$$

In this section, we are interested in applying the observer design methodology proposed in Section 4.2.1 to the system (4.43) in order to estimate respiratory gas exchange during exercise. To do so, the following disturbed version of system (4.43) is considered :

$$\begin{cases} \mathbf{x}_{k+1} &= \mathbf{A}\mathbf{x}_k + \mathbf{B}u_k + \mathbf{B}w_0 + \mathbf{F}d_k \\ \mathbf{y}_k &= \mathbf{C}(\rho_k)\mathbf{x}_k + \mathbf{Z}v_k \end{cases} \tag{4.44}$$

In order to implement this state observer, several hypotheses are performed :

- *H1 - The respiratory gas exchange model of the exercising cyclist is available.*
- *H2 - The power developed at the pedal level u_k is available for measurements.*
- *H3 - The maximal amplitudes of the state and output disturbances affecting the gas exchange model are known.*
- *H4 - The total carbon dioxide exhaled by the cyclist $\mathbf{y}_k = mCO_{2k}$ is available for measurements.*

Because the control strategy to be implemented is tailored to the cyclist, the respiratory gas exchange dynamics of any new user has to be identified, which ensures *H1*.

Most electric bicycles are equipped with pedaling torque and pedaling speed sensors, thus the pedaling power can easily be computed, which ensures *H2*.

In order to satisfy *H3*, maximum values $\bar{d}$ for the state disturbance d_k and $\bar{v}$ for the output disturbance v_k must be chosen. In practice, information on the accuracy of the sensors is available and can be used to choose $\bar{v}$. The value of $\bar{d}$ is more of a design choice. In the following we propose to choose it in order to model the state disturbances as a bias on the basal power w_0.

Ensuring *H4* in practice can be more difficult. In fact, the same ergo-spirometer used for respiratory gas exchange measurements during the model identification process can be used. However, most of these ergo-spirometers measure either only the oxygen consumption mO_2 or both the oxygen consumption mO_2 and the the carbon dioxide production mCO_{2tot}. In both cases, using such technology implies a costly and cumbersome implementation. Thankfully, a relationship between the minute ventilation $\dot{V}_E$ is known for healthy subjects [48] and translates the need of a carbon dioxide measurement to a ventilation measurement, much simpler to achieve in practice :

$$\dot{V}_E = m\dot{V}_{CO2} + c \tag{4.45}$$

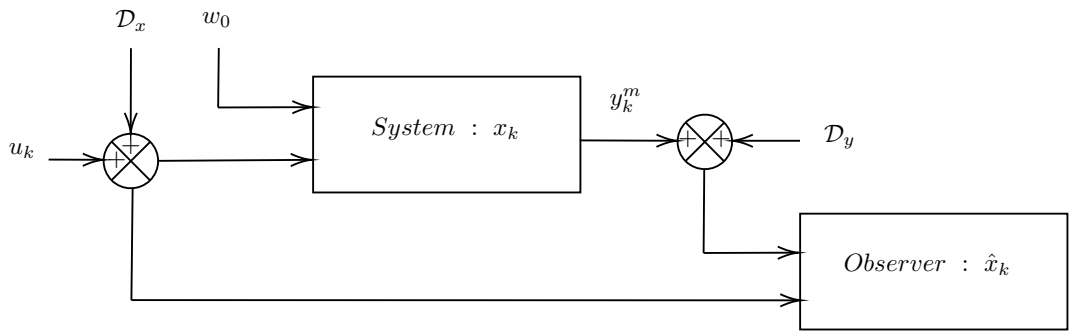

Figure 4.8: Simulation setup for design validation. The gas exchange model generates the current state $\mathbf{x}$ and the state observer the state estimation $\hat{\mathbf{x}}$ from input and output measurements. Here, the observer is the robust set-membership observer.

with $\dot{V}_E$ and $\dot{V}_{CO2}$ expressed in $L.min^{-1}$, $m = 25$ and $c = 4$ for healthy subjects. For this reason, in the following we assume that *H4* is fulfilled and consider a direct measurement of carbon dioxide for simplicity.

4.2.2.2 Illustration in simulation

In order to illustrate the observer design strategy, the following disturbed discrete-time respiratory gas exchange system is considered :

$$\begin{cases} \mathbf{x}_{k+1} &= \mathbf{A}\mathbf{x}_k + \mathbf{B}u_k + \mathbf{B}w_0 + \mathbf{F}d_k \\ \mathbf{y}_k &= \mathbf{C}(\rho_k)\mathbf{x}_k + \mathbf{Z}v_k \\ z_k &= x_{1k} - x_{2k} - \rho_{k-1}x_{3k} \\ \rho_k &= 0.5 + 0.5\tanh\left(\frac{z_T - z_k}{h}\right) \end{cases} \tag{4.46}$$

with :

$$\mathbf{A} = \begin{pmatrix} 0.34 & 0.54 & 0 \\ 0 & 0.93 & 0 \\ 0 & 0.16 & 0.35 \end{pmatrix}, \mathbf{B} = \begin{pmatrix} 1.5 \\ 1.5 \\ 0.9 \end{pmatrix} 10^{-3}, w_0 = 12.8, z_T = -0.22, h = 0.05 \tag{4.47}$$

The state disturbance $\mathcal{D}_x = \mathbf{F}d_k$ is supposed to be equal to 50% of the basal power w_0, thus we choose :

$$\mathbf{F} = \frac{1}{2}\mathbf{B}w_0, \bar{d} = 1 \tag{4.48}$$

The output disturbance $\mathcal{D}_y = \mathbf{Z}v_k$ is supposed to be at most equal to 0.5 g/min which is the typical accuracy of carbon dioxide sensors. In simulation, the output disturbance $\mathcal{D}_y$ is generated as a uniform noise between $-\bar{v}$ and $\bar{v}$. Thus we choose :

$$\mathbf{Z} = 0.5, \bar{v} = 1 \tag{4.49}$$

A description of the simulation setup is given in Fig. 4.8. As mentionned in hypothesis *H4*, the measured output y^m is the total carbon dioxide exhaled by the cyclist. Thus we have :

$$y_k^m = \mathbf{C}^m(\rho_k)\mathbf{x}_k + \mathbf{Z}v_k = \begin{pmatrix} 0 & 1 & \rho_k \end{pmatrix} \mathbf{x}_k + \mathbf{Z}v_k \tag{4.50}$$

The scheduling parameter ρ_k, which corresponds to the fraction of excess of carbon dioxide measured by the carbon dioxide sensor, is not measured in practice. Thus, in order to compute it, the estimated state vector $\hat{\mathbf{x}}_k$ is used.

After applying Algorithm 3 to the system (4.46), the following values are returned :

$$\mathbf{P} = \begin{pmatrix} 8.24 & -7.73 & 0.79 \\ -7.73 & 7.26 & -0.75 \\ 0.79 & -0.75 & 0.17 \end{pmatrix}, \mathbf{L} = \begin{pmatrix} 4.1 \\ 4.5 \\ 1.3 \end{pmatrix} 10^{-3}, \bar{\mathbf{e}} = \begin{pmatrix} 0.22 \\ 0.24 \\ 0.08 \end{pmatrix}, \gamma = 9.2$$

The estimation of the states of the system in simulation is shown in Fig. 4.9. The power input profile is constituted of steps of random magnitude. One can notice that the scheduling parameter ρ takes values in its full range of variation. The real states of the system belong to the uncertainty interval which ensures the robustness of the observer.

The estimation of the outputs of the system in simulation is shown in Fig. 4.10. The state observer is able to provide a good estimation of both the oxygen consumption $y_1 = mO_2$ and the total carbon dioxide production $y_2 = mCO_2$.

These results are obtained when the model used for the state observer is completely accurate and the only differences with the nominal system are due to the state disturbance $\mathcal{D}_x$ and output disturbance $\mathcal{D}_y$. Fig. 4.11 shows the estimated states when parametric uncertainties are added to the real respiratory gas exchange system. In this case, the parameters of the matrix $\mathbf{A}$ differ to up to 10% from their nominal value. One can notice that in this case the estimation error bounds are not satisfied anymore.

Thus, we conclude that, as such, the adapted observer synthesis proposed in Section 4.2.1 provides a good estimation of respiratory gas exchanges but is not robust to parametric uncertainties. In the next section, an attempt to improve the robustness of the state observer to parametric uncertainties is presented.

4.3 Robust Proportional Integral observer for respiratory gas exchange estimation

In the previous section, a method to estimate respiratory gas exchange during exercise was presented based on a set-membership observer. It was showed that this estimation method

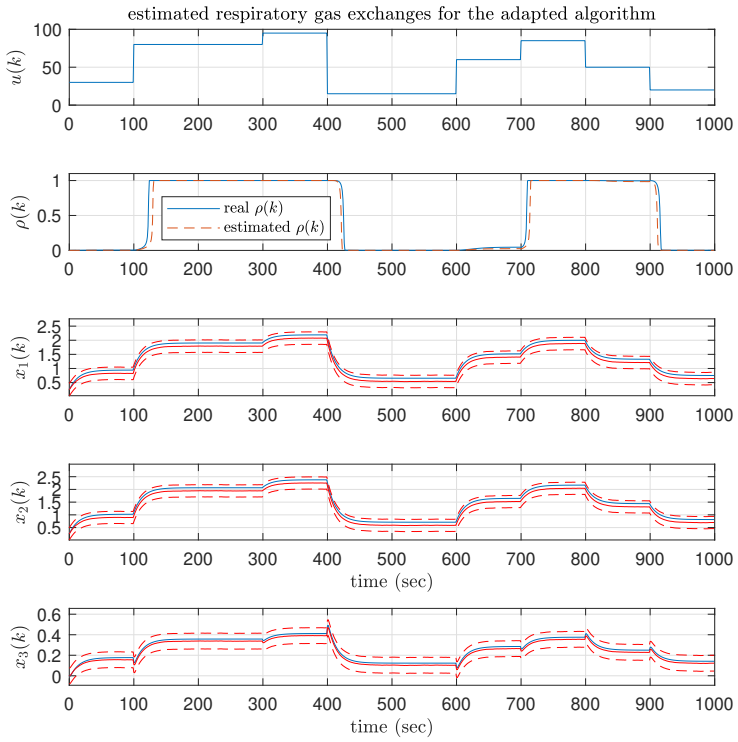

Figure 4.9: Evolution of the system's states, state estimates and estimation error bounds for the adapted synthesis. The states of the real system are shown in full blue lines, their estimate in full red lines and the error bounds in dashed red lines.

performs well in simulation but fails in the case where the parameters of the system are affected by uncertainties. In this section, we propose to use a robust proportional integral (RPI) observer in order to estimate respiratory gas exchanges during exercise. The objective of this approach is to make the estimation more robust to parametric uncertainties. First, the design of the observer is presented and then its behavior is illustrated in simulations.

This work was submitted and accepted at the *SAFE 2022* conference in Cyprus.

4.3.1 The basal metabolic rate

The basal metabolic rate (BMR) is a physiological quantity characterizing the energy consumption of the human body at rest and can be expressed in Watts. It comprises the minimum functions the body requires such as breathing, regulating the body temperature or ensuring the brain activity. The BMR is closely connected to the oxygen consumption and the carbon dioxide production of the individual. Methods exploiting this connection are known under the name of indirect-calorimetry.

It has been shown that the BMR varies between individual based on parameters like age,

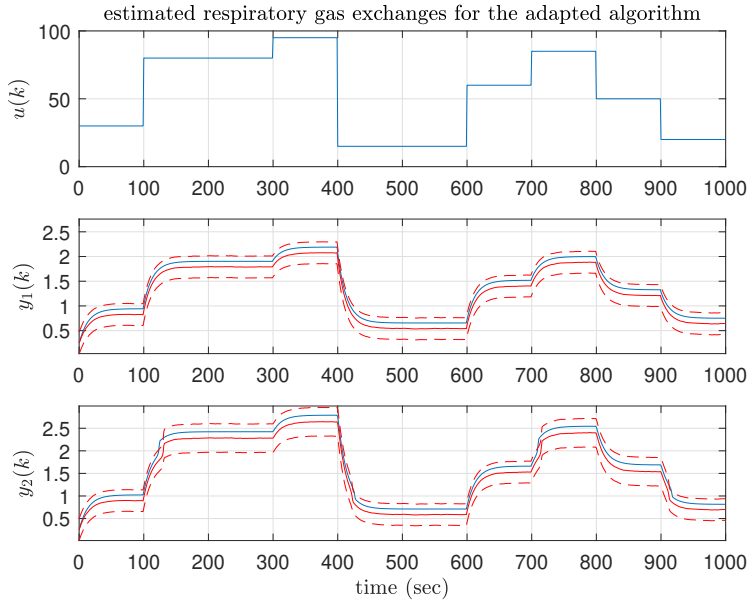

Figure 4.10: Evolution of the system's outputs, output estimates and estimation error bounds for the adapted synthesis. The outputs of the real system are shown in full blue lines, their estimate in full red lines and the error bounds in dashed red lines.

gender and weight [23, 24, 34, 35]. Also, the BMR can vary for a given individual depending on temperature [33], altitude [20] or training level [16].

In order to develop control laws allowing the regulation of physiological variables such as the respiratory gas exchanges or the energy expenditure, the variability of the BMR has to be taken into account. Thus, in this section, we propose to estimate its value in real-time.

4.3.2 Problem statement

Here, we explore the use of a Proportional Integral (PI) observer for estimating both the respiratory gas exchange variables (the amounts of O_2 intake and CO_2 output) and the basal metabolic rate (BMR). Several methods for designing PI observers have been proposed in the literature, some of them are known under the name of disturbance observer based control (DOBC) and are aiming at estimating and compensating the influence of disturbances and uncertainties on a closed-loop system. For continuous-time linear and non-linear frameworks, an extensive review of these methods can be found in [9] and a chronological overview in [39]. DOBC can be found under different forms, in [37] the disturbance is reconstructed using a filter with appropriate bandwidth, in [22] an extended state observer (ESO) is proposed, [25, 26] developed the idea of unknown input observers (UIO) and [42, 43] of equivalent input disturbances (EID).

The considered gas exchange dynamics is the following uncertain discrete-time linear system with a linear parameter varying matrix output matrix :

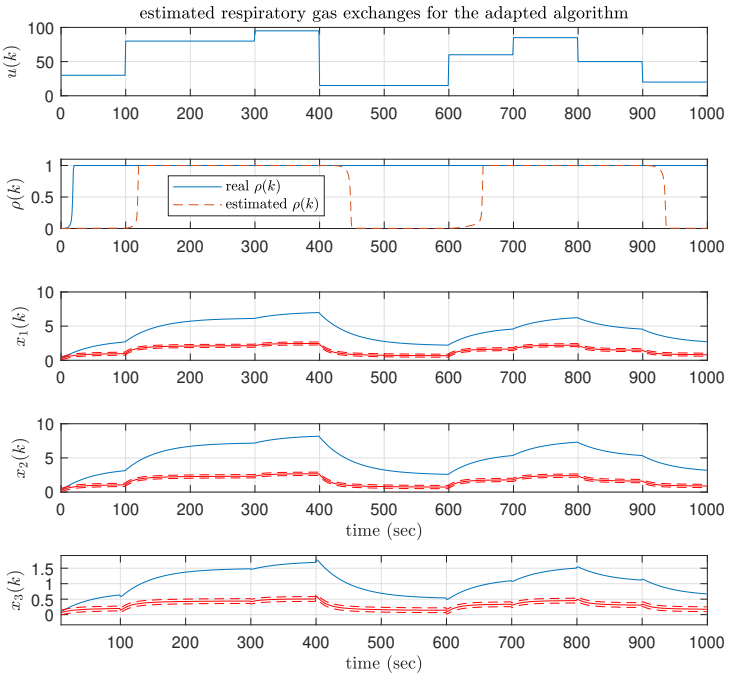

Figure 4.11: Evolution of the system's states, state estimates and estimation error bounds for the adapted synthesis. The states of the real system are shown in full blue lines, their estimate in full red lines and the error bounds in dashed red lines. In this case, the coefficients of the real system differ to up to 10% of their nominal value.

$$\begin{cases} \mathbf{x}(k+1) &= \mathbf{A}\mathbf{x}(k) + \mathbf{B}u(k) + \mathbf{B}(w_0 + p(k)) + \mathbf{F}d(k) \\ \mathbf{y}(k) &= \mathbf{C}(\rho(k))\mathbf{x}(k) + \mathbf{Z}v(k) \end{cases} \tag{4.51}$$

where $p(k) \in \mathbb{R}$ is a piece-wise constant disturbance signal modelling unknown variations of the basal power with respect to the nominal one w_0.

In order to recover the value of the unknown basal disturbance $p(k)$, we propose to use a proportional integral (PI) observer. To design such observer, we first extend the states of system (4.51) as follows :

$$\mathbf{x}_e(k) = \begin{bmatrix} \mathbf{x}(k) \\ p(k) \end{bmatrix} \tag{4.52}$$

We can now re-write (4.51) as :

$$\begin{cases} \mathbf{x}_e(k+1) &= \mathbf{A}_e\mathbf{x}_e(k) + \mathbf{B}_e(u(k) + w_0) + \mathbf{F}_e d(k) \\ \mathbf{y}(k) &= \mathbf{C}_e(\rho(k))\mathbf{x}_e(k) + \mathbf{Z}v(k) \end{cases} \tag{4.53}$$

with $\mathbf{A}_e = \begin{bmatrix} \mathbf{A} & \mathbf{B} \\ 0 & 1 \end{bmatrix}$, $\mathbf{B}_e = \begin{bmatrix} \mathbf{B} \\ 0 \end{bmatrix}$, $\mathbf{F}_e = \begin{bmatrix} \mathbf{F} \\ \theta \end{bmatrix}$ and $\mathbf{C}_e = \begin{bmatrix} \mathbf{C} & 0 \end{bmatrix}$.

The coefficient $\theta > 0$, in matrix $\mathbf{F}_e$, is a constant parameter used during the observer design process. This coefficient is necessary to establish a non-zero transfer function between disturbances $d(k)$ and the extended state $p(k)$, allowing an $\mathcal{H}_\infty$ observer synthesis. The value of that parameter θ can be considered as a degree of freedom to design an observer with suitable speed convergence and noise attenuation.

Here, we assume that there exists a constant observer gain $\mathbf{L} \in \mathbb{R}^4$ such that the following parameter-dependent state observer can be performed for any value of $\rho(k)$:

$$\begin{cases} \hat{\mathbf{x}}_e(k+1) &= \tilde{\mathbf{A}}_e(\rho(k))\hat{\mathbf{x}}_e(k) + \mathbf{B}_e(u(k) + w_0) + \mathbf{L}y(k) \\ \hat{\mathbf{y}}(k) &= \mathbf{C}(\rho(k))\hat{\mathbf{x}}_e(k) \end{cases} \tag{4.54}$$

with $\tilde{\mathbf{A}}_e(\rho(k)) = \mathbf{A}_e - \mathbf{L}\mathbf{C}_e(\rho(k))$.

Now, defining the state estimation error at instant k as follows:

$$\mathbf{e}(k) = \mathbf{x}_e(k) - \hat{\mathbf{x}}_e(k) \tag{4.55}$$

we can write its dynamics as:

$$\mathbf{e}(k+1) = \tilde{\mathbf{A}}(\rho(k))\mathbf{e}(k) + \mathbf{E}\mathbf{w}(k) \tag{4.56}$$

with $\mathbf{E} = \begin{bmatrix} \mathbf{F} & -\mathbf{L}\mathbf{Z} \end{bmatrix}$ and $\mathbf{w}(k) = \begin{bmatrix} d(k) & v(k) \end{bmatrix}^T$.

Thus, the problem is to find a constant observer gain $\mathbf{L} \in \mathbb{R}^{n \times p}$ for the parameter dependent state-observer (4.54) such that for all $\boldsymbol{\rho}(k)$ the dynamics (4.56) are stable with a quadratic $\mathcal{H}_\infty$ performance γ, i.e. such that the ratio between the estimation error and the disturbance $\mathbf{w}(k)$ is bounded in the sense of the $\mathcal{L}_2$ norm: $\|\mathbf{e}(k)\|_2 < \gamma \|\mathbf{w}(k)\|_2$.

Matrix $\mathbf{C}_e$ is depending on the varying parameter $\rho(k)$. Because $\rho(k)$ belongs to the known interval $[0; 1]$ we perform the following polytopic decomposition for $\mathbf{C}_e$:

$$\mathbf{C}_e(\rho(k)) = \alpha_0(k)\mathbf{C}_{e0} + \alpha_1(k)\mathbf{C}_{e1} \tag{4.57}$$

where for all k $\alpha_0(k) \geq 0$, $\alpha_1(k) \geq 0$ and

$$\alpha_0(k) + \alpha_1(k) = 1 \tag{4.58}$$

Matrices $\mathbf{C}_{e0}$ and $\mathbf{C}_{e1}$ are the vertex matrices of the decomposition and are computed by evaluating $\mathbf{C}_e(\rho(k))$ its extreme values, respectively $\mathbf{C}_e(0)$ and $\mathbf{C}_e(1)$. A similar decomposition is applied to the system matrix $\tilde{\mathbf{A}}_e(\rho(k))$:

$$\tilde{\mathbf{A}}_e(\rho(k)) = \alpha_0(k)\tilde{\mathbf{A}}_{e0} + \alpha_1(k)\tilde{\mathbf{A}}_{e1} \tag{4.59}$$

with $\tilde{\mathbf{A}}_{e0} = \mathbf{A}_e - \mathbf{L}\mathbf{C}_{e0}$ and $\tilde{\mathbf{A}}_{e1} = \mathbf{A}_e - \mathbf{L}\mathbf{C}_{e1}$.

In order to design the state observer, we solve an Linear Matrix Inequality (LMI) problem, formulated in the following theorem :

Theorem 5. *Consider the system (4.56) and a given matrix* $\mathbf{Q} \succ 0$. *The observer gain* $\mathbf{L}$ *which minimizes the* $\mathcal{H}_\infty$ *norm of the system (4.56) is found if there exist a symmetric positive definite matrix* $\mathbf{P}$, *a positive scalar* $\gamma \geq 0$ *and matrix* $\mathbf{U}$ *satisfying the following condition :*

$$\begin{pmatrix} -\boldsymbol{P} + \boldsymbol{Q} & 0 & \boldsymbol{A}_{ej}^T\boldsymbol{P} - \boldsymbol{C}_{ej}^T\boldsymbol{U}^T \\ \star & -\gamma^2 & [\boldsymbol{P}\boldsymbol{F} - \boldsymbol{U}\boldsymbol{Z}]^T \\ \star & \star & -\boldsymbol{P} \end{pmatrix} \preceq 0 \tag{4.60}$$

for every vertex of the polytopic decomposition, $j = \{0,1\}$. *Moreover, the observer matrix can be obtained as :*

$$\mathbf{L} = \mathbf{P}^{-1}\mathbf{U} \tag{4.61}$$

□

4.3.3 Illustration in simulation

To validate the observer design methodology, we compute a state observer for system (4.53) undergoing state and output disturbances (d and v), as well as a constant disturbance p on w_0. Here, we choose $\theta = 0.25$.

The measured output y^m is the total carbon dioxide exhaled by the cyclist. Thus we have :

$$y_k^m = \mathbf{C}^m(\rho_k)\mathbf{x}_k + \mathbf{Z}v_k = \begin{pmatrix} 0 & 1 & \rho_k \end{pmatrix}\mathbf{x}_k + \mathbf{Z}v_k \tag{4.62}$$

The scheduling parameter ρ_k, which corresponds to the fraction of excess of carbon dioxide measured by the carbon dioxide sensor, is not measured in practice. Thus, in order to compute it, the estimated state vector $\hat{\mathbf{x}}_k$ is used.

We suppose that the model mismatch can be split into two contributions. First, a constant disturbance p, modelling a low bandwidth component due to the uncertainty on the value of w_0 and taking up to 100% of the hypothesized value for w_0. Then, a random component d following a uniform distribution, modelling a high bandwidth component and taking up to 10% of the hypothesized value for w_0. Thus we choose :

$$\mathbf{F} = \mathbf{F}w_0, \bar{d} = 1 \tag{4.63}$$

The output disturbance $\mathcal{D}_y = \mathbf{Z}v_k$ is supposed to be at most equal to $0.1\, g/min$. In simulation, the output disturbance $\mathcal{D}_y$ is generated as a uniform noise between $-\bar{v}$ and $\bar{v}$. Thus we choose :

$$\mathbf{Z} = 0.1, \bar{v} = 1 \tag{4.64}$$

After applying Theorem 4.60 to the system (4.53), the following values are returned :

$$\mathbf{P} = \begin{pmatrix} 0.7530 & -0.1680 & -0.0530 & -0.0005 \\ -0.1680 & 0.8933 & -0.0896 & -0.0097 \\ -0.0530 & -0.0896 & 2.2650 & -0.0003 \\ -0.0005 & -0.0097 & -0.0003 & 0.0010 \end{pmatrix} 10^5, \mathbf{L} = \begin{pmatrix} 0.27 \\ 0.38 \\ 0.15 \\ 4.0 \end{pmatrix}, \gamma = 24.16$$

For comparison purposes, a simple robust state observer was designed by applying Theorem 4.30 on system (4.51), thus removing the integral action. The following values are returned :

$$\mathbf{P}_r = \begin{pmatrix} 47.9067 & -41.7438 & -5.7833 \\ -41.7438 & 63.6976 & -7.4568 \\ -5.7833 & -7.4568 & 75.2937 \end{pmatrix}, \mathbf{L}_r = \begin{pmatrix} 0.0041 \\ 0.0049 \\ 0.0023 \end{pmatrix}, \gamma_r = 0.0352,$$

We run a simulation under which the ideal system (4.51) is affected by the exact same disturbances and uncertainties as the ones chosen for the design and estimate the states using both the robust PI observer and the simple robust observer.

Fig. 4.12 shows the evolution of the states and output of the real system and the states estimated by the designed robust PI observer and by the same robust observer but without the estimation of d. Three simulations were performed using the same power profile but different disturbance and noise signals. The power profile was generated using piece-wise constant power levels of random magnitude such that the parameter ρ takes values in its full range of variation. The evolution of the varying parameter ρ and of its estimation are shown, the mismatch between them can be explained by the estimation errors on the state and the tendency of ρ to vary abruptly.

Fig. 4.13 shows the evolution of the estimation error for each state of the system, in each simulation and for both the robust PI observer and the robust observer. It shows that for every scenario, the estimation error of the robust PI observer tends to 0, while the estimation of the robust observer is not. Thus, the proposed observer is robust to piece-wise constant disturbances affecting the basal power of the system.

Fig. 4.14 shows that for each simulation the robust PI observer is able to reconstruct the value of p.

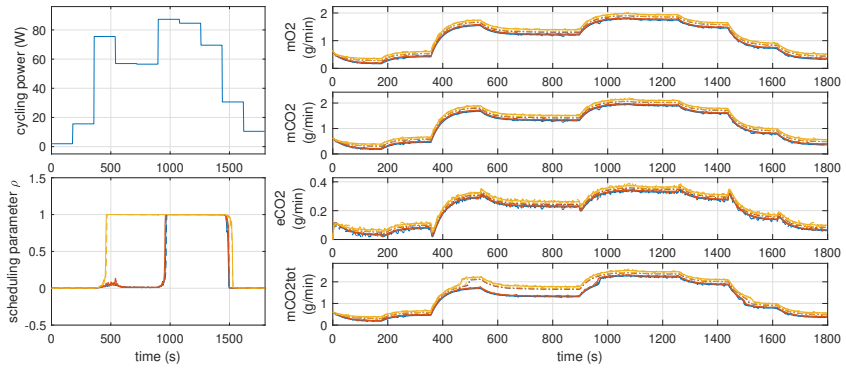

Figure 4.12: Evolution of the states and output of the real system, in full lines, and of their estimation by the PI observer, in dashed lines, and by the robust observer, in dotted lines, to a step input function.

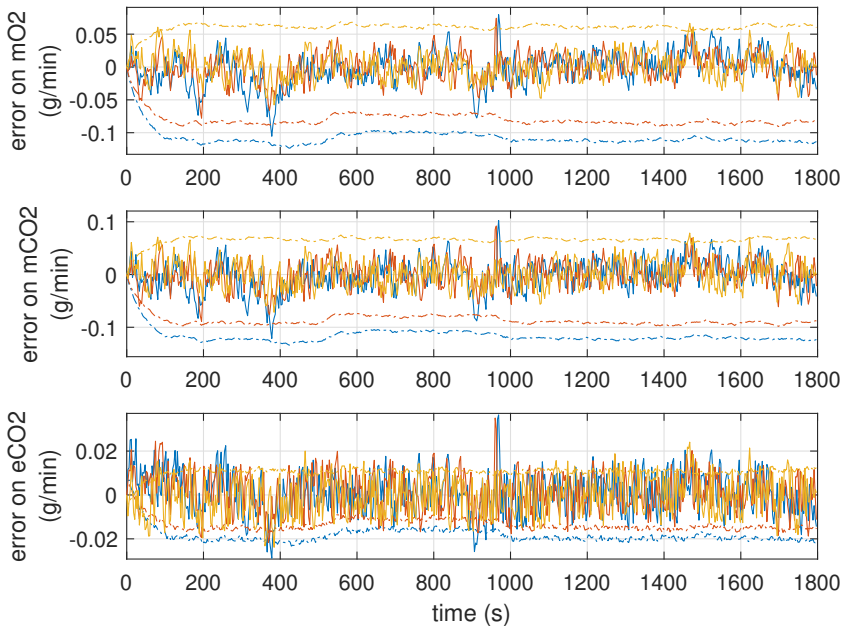

Figure 4.13: State estimation errors after simulating 3 times the system for the same power profile but different noises and disturbances affecting the system. The errors of the PI observer are shown in full lines, the errors of the robust observer in dotted lines.

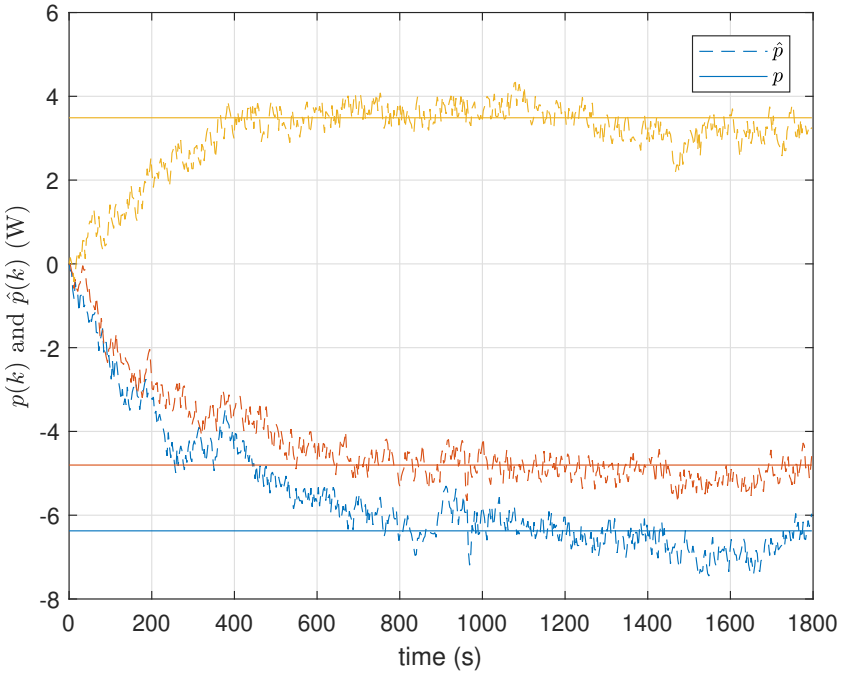

Figure 4.14: Estimation of the constant disturbance p after simulating 3 times the system for the same power profile but different noises and disturbances affecting the system.

Fig. 4.15 shows the influence of the parameter θ in the quality of the disturbance estimation. Multiple simulations were ran using different observer gains $\mathbf{L}$ based on different values of θ chosen for the design. We can see that higher values for θ allow a faster but noisier convergence of the estimation. Lower values for θ allow a smoother but slower convergence of the estimation. Parameter θ can then be used as a tuning parameter for the observer taking into account the noise levels affecting the state and output of the considered system. In our example $\theta = 0.25$ appeared to be a good trade-off.

In practice, estimated values of gas exchange variables and basal power are used by practitioners to characterize the effort performed. For example, the respiratory quotient (RQ) allows to estimate the contribution of carbohydrates and fats oxidized during the exercise and is defined as follows :

$$RQ = VCO_2/VO_2 = \delta_1 mCO_2/\delta_2 mO_2 \tag{4.65}$$

With VCO_2, the volume of CO_2 produced per unit of time, VO_2, the volume of O_2 consumed per unit of time, $\delta_1 = 1.429kg/m^3$, the density of O_2 at $20°C$, $\delta_2 = 1.842kg/m^3$, the density of CO_2 at $20°C$. It is known that values of RQ around 1 suggest that carbohydrates are oxidized and values of RQ around 0.7 suggest that fats are oxidized.

Fig. 4.16 shows the values of RQ computed for each simulation and their estimated values using the robust PI observer and the robust observer. We can see that the estimation provided by the robust PI observer are accurate and that the estimation of RQ provided by the robust observer can show significant mismatch. For example, in $RQ1$ and $RQ2$, the robust observer

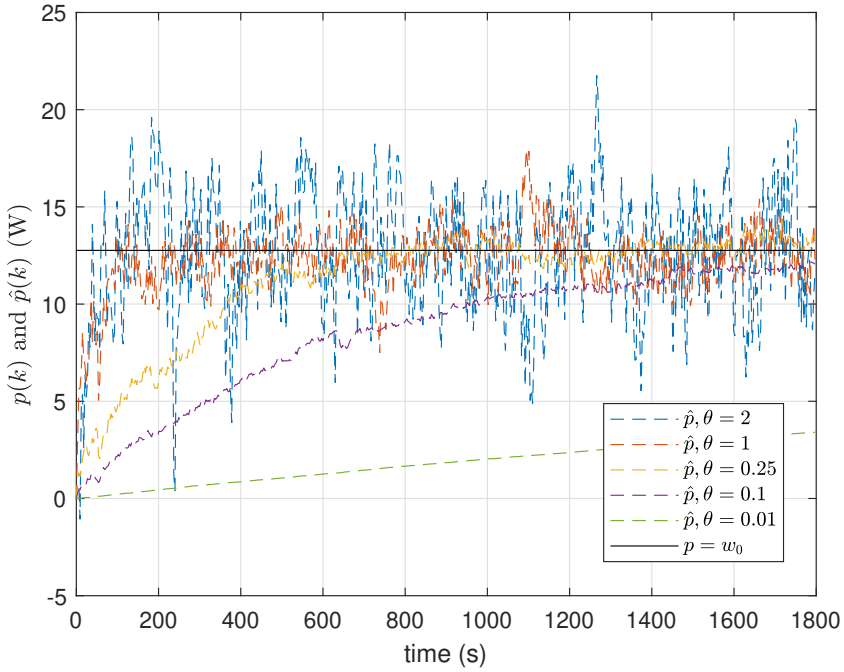

Figure 4.15: Estimation of the constant disturbance $p = w_0$ after simulating 5 times the system with different gains for the observer based on a different value for θ in the design process.

fails to recover the real RQ between $t = 500$ sec and $t = 950$ sec. This shows that even if the estimation errors are slightly higher with the robust observer for the chosen levels of disturbance p, the consequences in the interpretation of the results can be significant.

To conclude, we saw in this section that the proposed robust proportional observer was able to estimate the value of the disturbance affecting the basal metabolic rate. This observer is performing better than the observer proposed in Section 4.2.2 when the basal power is not known accurately. The robust proportional observer can be used in practice to estimate respiratory gas exchanges more accurately and recover the value of the basal metabolic rate in real time.

4.4 Conclusion

In this chapter, two methods are proposed in order to estimate the respiratory gas exchange of a cyclist during exercise.

First, an adaptation of the Explicit Error Bounds Set-Membership observer proposed by Loukkas to the case of parameter dependent output LPV systems is presented. The synthesis of this observer is based on the solution of multiple Linear Matrix Inequality problems in order to compute the observer gain and uncertainty bounds on the estimation. This observer can

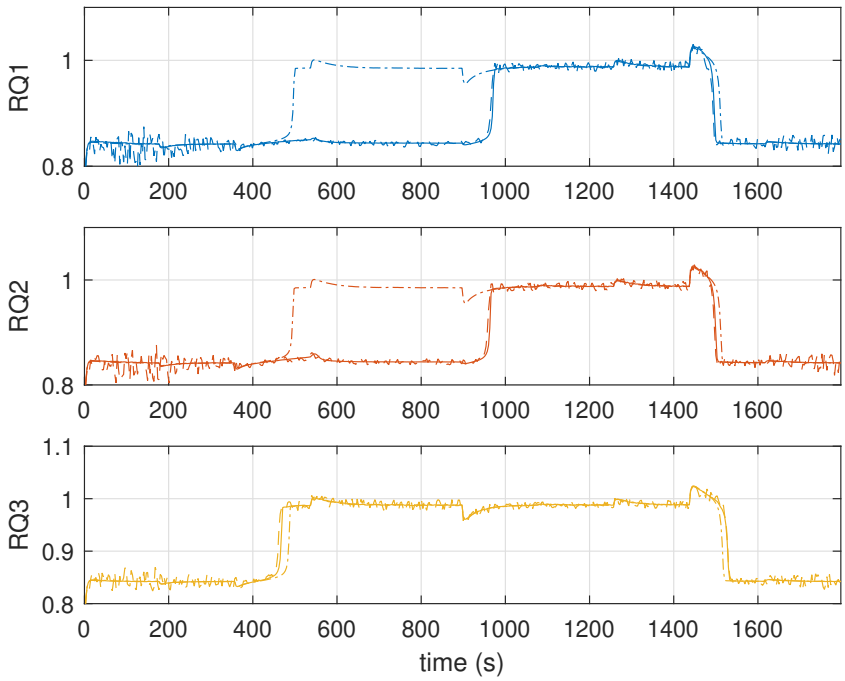

Figure 4.16: Respiratory quotient (RQ) for each of the simulations. The RQ of the real system is shown in full lines, its estimation by the robust PI observer is shown in dashed lines and its estimation by the robust observer is shown in pointed lines.

be used in practice to estimate the oxygen consumption and carbon dioxide production of the cyclist. However, this observer requires the respiratory gas exchange model of the cyclist to be perfectly known and is not robust to parametric uncertainties.

In order to propose an estimation strategy that is robust to parametric uncertainties, a robust proportional integral observer was designed. For this observer, the assumption is made that the basal metabolic rate of the cyclist is susceptible to vary. The robust proportional integral observer is designed so that both the oxygen consumption, the carbon dioxide production and the variation of the basal power are estimated during exercise.

Bibliography

[1] T. Alamo, J.M. Bravo, and E.F. Camacho.
Guaranteed state estimation by zonotopes.
Automatica, 41(6):1035–1043, June 2005.

[2] Pierre Apkarian, Pascal Gahinet, and Greg Becker.
Self-scheduled h control of linear parameter-varying systems: a design example.
Automatica, 31(9):1251–1261, 1995.

[3] Y. Becis-Aubry, M. Boutayeb, and M. Darouach.
State estimation in the presence of bounded disturbances.
Automatica, 44(7):1867–1873, July 2008.

[4] D. Bertsekas and I. Rhodes.
Recursive state estimation for a set-membership description of uncertainty.
IEEE Transactions on Automatic Control, 16(2):117–128, April 1971.

[5] Franco Blanchini and Stefano Miani.
Set-Theoretic Methods in Control.
Systems & Control: Foundations & Applications. Springer International Publishing, Cham, 2015.

[6] Ryan James Caverly and James Richard Forbes.
LMI properties and applications in systems, stability, and control theory.
CoRR, abs/1903.08599, 2019.

[7] S. Ben Chabane, C. Stoica Maniu, T. Alamo, E.F. Camacho, and D. Dumur.
A New Approach for Guaranteed Ellipsoidal State Estimation.
IFAC Proceedings Volumes, 47(3):6533–6538, 2014.

[8] Mohammed Chadli, Mohamed Darouach, and Jamal Daafouz.
Static output stabilisation of singular lpv systems: Lmi formulation.
In *2008 47th IEEE Conference on Decision and Control*, pages 4793–4796. IEEE, 2008.

[9] Wen-Hua Chen, Jun Yang, Lei Guo, and Shihua Li.
Disturbance-observer-based control and related methods—an overview.
IEEE Transactions on industrial electronics, 63(2):1083–1095, 2015.

[10] L. Chisci, A. Garulli, and G. Zappa.
Recursive state bounding by parallelotopes.
Automatica, 32(7):1049–1055, July 1996.

[11] Christophe Combastel.
Zonotopes and Kalman observers: Gain optimality under distinct uncertainty paradigms and robust convergence.
Automatica, 55:265–273, May 2015.

[12] C. Durieu, É. Walter, and B. Polyak.
Multi-Input Multi-Output Ellipsoidal State Bounding.
Journal of Optimization Theory and Applications, 111(2):273–303, November 2001.

[13] Denis Efimov, Wilfrid Perruquetti, Tarek Raissi, and Ali Zolghadri.
On interval observer design for time-invariant discrete-time systems.
In *2013 European Control Conference (ECC)*, pages 2651–2656, Zurich, July 2013. IEEE.

[14] L. El Ghaoui and G. Calafiore.
Robust filtering for discrete-time systems with bounded noise and parametric uncertainty.
IEEE Transactions on Automatic Control, 46(7):1084–1089, July 2001.

[15] Fuwen Yang, Zidong Wang, and Y.S. Hung.
Robust Kalman filtering for discrete time-varying uncertain systems with multiplicative noises.
IEEE Transactions on Automatic Control, 47(7):1179–1183, July 2002.

[16] Meredith Gilliat-Wimberly, Melinda M Manore, Kathleen Woolf, PAMELA D SWAN, and Steven S Carroll.
Effects of habitual physical activity on the resting metabolic rates and body compositions of women aged 35 to 50 years.
Journal of the American Dietetic Association, 101(10):1181–1188, 2001.

[17] J.L. Gouzé, A. Rapaport, and M.Z. Hadj-Sadok.
Interval observers for uncertain biological systems.
Ecological Modelling, 133(1-2):45–56, August 2000.

[18] Michael Grant and Stephen Boyd.
Graph implementations for nonsmooth convex programs.

In V. Blondel, S. Boyd, and H. Kimura, editors, *Recent Advances in Learning and Control*, Lecture Notes in Control and Information Sciences, pages 95–110. Springer-Verlag Limited, 2008.
`http://stanford.edu/~boyd/graph_dcp.html`.

[19] Michael Grant and Stephen Boyd.
CVX: Matlab software for disciplined convex programming, version 2.1.
`http://cvxr.com/cvx`, March 2014.

[20] Robert F Grover.
Basal oxygen uptake of man at high altitude.
Journal of applied Physiology, 18(5):909–912, 1963.

[21] Guanrong Chen, Jianrong Wang, and L.S. Shieh.
Interval Kalman filtering.
IEEE Transactions on Aerospace and Electronic Systems, 33(1):250–259, January 1997.

[22] Jingqing Han.
From pid to active disturbance rejection control.
IEEE transactions on Industrial Electronics, 56(3):900–906, 2009.

[23] J Arthur Harris and Francis G Benedict.
A biometric study of human basal metabolism.
Proceedings of the National Academy of Sciences, 4(12):370–373, 1918.

[24] CJK Henry.
Basal metabolic rate studies in humans: measurement and development of new equations.
Public health nutrition, 8(7a):1133–1152, 2005.

[25] C Johnson.
Optimal control of the linear regulator with constant disturbances.
IEEE Transactions on Automatic Control, 13(4):416–421, 1968.

[26] CD Johnson.
Real-time disturbance-observers; origin and evolution of the idea part 1: The early years.
In *2008 40th Southeastern Symposium on System Theory (SSST)*, pages 88–91. IEEE, 2008.

[27] Simon J Julier and Jeffrey K Uhlmann.
New extension of the kalman filter to nonlinear systems.
In *Signal processing, sensor fusion, and target recognition VI*, volume 3068, pages 182–193. Spie, 1997.

[28] Rudolph Emil Kalman.
A new approach to linear filtering and prediction problems.
1960.

[29] Awais Khan, Wei Xie, Bo Zhang, and Long-Wen Liu.
A survey of interval observers design methods and implementation for uncertain systems.
Journal of the Franklin Institute, 358(6):3077–3126, April 2021.

[30] Ernesto Kofman, José A. De Doná, and Maria M. Seron.
Probabilistic set invariance and ultimate boundedness.
Automatica, 48(10):2670–2676, October 2012.

[31] Alex A. Kurzhanskiy and Pravin Varaiya.
Ellipsoidal toolbox.
Technical Report UCB/EECS-2006-46, EECS Department, University of California, Berkeley, May 2006.

[32] Lihua Xie, Yeng Chai Soh, and C.E. de Souza.
Robust Kalman filtering for uncertain discrete-time systems.
IEEE Transactions on Automatic Control, 39(6):1310–1314, June 1994.

[33] WJ McConnell and CP Yagloglou.
Basal metabolism as affected by atmospheric conditions.
Archives of Internal Medicine, 36(3):382–396, 1925.

[34] Robert G McMurray, Jesus Soares, Carl J Caspersen, and Thomas McCurdy.
Examining variations of resting metabolic rate of adults: a public health perspective.
Medicine and science in sports and exercise, 46(7):1352, 2014.

[35] Katarina Melzer, Juliane Heydenreich, Yves Schutz, Anne Renaud, Bengt Kayser, and Urs Mäder.
Metabolic equivalent in adolescents, active adults and pregnant women.
Nutrients, 8(7):438, 2016.

[36] Nacim Meslem, John Martinez, Nacim Ramdani, and Gildas Besançon.
An interval observer for uncertain continuous-time linear systems.
International Journal of Robust and Nonlinear Control, 30(5):1886–1902, March 2020.

[37] Kiyoshi Ohishi, Masato Nakao, Kouhei Ohnishi, and Kunio Miyachi.
Microprocessor-controlled dc motor for load-insensitive position servo system.
IEEE transactions on industrial electronics, (1):44–49, 1987.

[38] S.V. Rakovic and D.Q. Mayne.

State estimation for piecewise affine, discrete time systems with bounded disturbances.
In *2004 43rd IEEE Conference on Decision and Control (CDC) (IEEE Cat. No.04CH37601)*, pages 3557–3562 Vol.4, Nassau, Bahamas, 2004. IEEE.

[39] Emre Sariyildiz, Roberto Oboe, and Kouhei Ohnishi.
Disturbance observer-based robust control and its applications: 35th anniversary overview.
IEEE Transactions on Industrial Electronics, 67(3):2042–2053, 2019.

[40] Andrey V. Savkin and Ian R. Petersen.
Robust state estimation and model validation for discrete-time uncertain systems with a deterministic description of noise and uncertainty.
Automatica, 34(2):271–274, February 1998.

[41] F. Schweppe.
Recursive state estimation: Unknown but bounded errors and system inputs.
IEEE Transactions on Automatic Control, 13(1):22–28, February 1968.

[42] Jin-Hua She, Mingxing Fang, Yasuhiro Ohyama, Hiroshi Hashimoto, and Min Wu.
Improving disturbance-rejection performance based on an equivalent-input-disturbance approach.
IEEE Transactions on Industrial Electronics, 55(1):380–389, 2008.

[43] Jin-Hua She, Xin Xin, and Yaodong Pan.
Equivalent-input-disturbance approach—analysis and application to disturbance rejection in dual-stage feed drive control system.
IEEE/ASME Transactions on Mechatronics, 16(2):330–340, 2010.

[44] Qiang Shen, Jieyu Liu, Xiaogang Zhou, Qian Zhao, and Qi Wang.
Low-complexity ISS state estimation approach with bounded disturbances: Low-complexity ISS state estimation approach with bounded disturbances.
International Journal of Adaptive Control and Signal Processing, 32(10):1473–1488, October 2018.

[45] M. P. Spathopoulos and I. D. Grobov.
A state-set estimation algorithm for linear systems in the presence of bounded disturbances.
International Journal of Control, 63(4):799–811, March 1996.

[46] Bartolomeo Stellato, Bart P. G. Van Parys, and Paul J. Goulart.
Multivariate Chebyshev Inequality With Estimated Mean and Variance.
The American Statistician, 71(2):123–127, April 2017.

[47] Zhenhua Wang, Cheng-Chew Lim, and Yi Shen.
Interval observer design for uncertain discrete-time linear systems.

Systems & Control Letters, 116:41–46, June 2018.

[48] Susan A. Ward.
Ventilation/carbon dioxide output relationships during exercise in health.
European Respiratory Review, 30(160):200160, April 2021.

[49] Xing Zhu, Yeng Chai Soh, and Lihua Xie.
Design and analysis of discrete-time robust kalman filters.
Automatica, 38(6):1069–1077, 2002.

Chapter 5

Control of physiological quantities during cycling

Contents

5.1 Control of physiological variables

5.1.1 Exercise prescription

Exercise physiology practitioners are often expected to prescribe exercise sessions as part of therapy or training programs. To trigger specific physiological responses the exercise sessions are adapted to the considered individual. The exercise sessions vary depending on the considered type of activity, their duration, their frequency and on their *intensity*. This last parameter is the hardest to handle and there is no consensus regarding the way to ensure it. For example, the intensity of the exercise can be defined based on mechanical variables, based on the heart rate or based on the respiratory gas exchanges. An overview of these different approaches is given in the next paragraphs. For a complete review of these approaches the reader is referred to [23, 24].

The mechanical variables used to quantify the intensity of exercise are related to the rate of exercise and often depends on the type of activity considered. For example, during weight-lifting exercise, fractions of the one-repetition maximum (1-RM), corresponding to the maximal weight that a subject can lift, drag or push one time, are used. In aqua-running, the walking cadence can be chosen. These variables relate to the mechanical power developed in a given activity, which is why for cycling tests on cycle-ergometer, the mechanical power developed on the pedal can be used directly as an index for exercise prescription. These indexes have the advantage to be directly manipulated and/or measured during the physical activity. However, because of their mechanical nature, they are likely to produce different physiological responses depending on the considered individual and require the expertise of the practitioner to be tuned properly.

The intensity of exercise can also be defined using the maximal heart rate. Two main approaches are used. The first one is a percentage of the maximal heart rate HR_{max}, and is labeled $\%HR_{max}$. This method is convenient in the sense that based on a maximal effort test, the exercise range is defined using on the maximal heart rate reached, which makes it convenient to use. However, this method does not take into account the differences in basal heart rate. The second one is a percentage of the *reserve* heart rate of the individual $\%HRR$, corresponding to a fraction of the heart rate above the basal level. These indexes have the advantage to be based on heart rate measurements which are usually non-invasive and inexpensive but because the heart rate is sensibly affected by external factors like fatigue, stress, temperature, and because of its variability during exercise, these indexes can be hard to manage.

Finally, indexes based on respiratory gas exchanges are also formulated. Similarly to $\%HR_{max}$ and $\%HRR$, a fraction of the maximal oxygen consumption $\%VO_{2max}$ or a fraction of the reserve oxygen consumption $\%VO_2R$ can be used. Physiological thresholds, identified using respiratory gas exchanges, can also be used like the aerobic threshold $AerT$ or the anaerobic threshold AnT. While the thresholds indexes are reputed to reflect the physiological response of the individual more accurately, they also are more difficult to measure and implement.

In order to ensure that the prescriptions are respected by the training individual, automated control strategies have been developed. An overview of these methods is given in the following sections.

5.1.2 Control of the developed mechanical work

Several examples of automatic exercise systems controlling the intensity of the exercise can be found in the literature. Some of them regard the exercise on treadmills using robot assisted gait. In these systems, the body weight of the training individual is supported and the walking movement is assisted using robotic limb actuators. These systems are used for the rehabilitation of neurologically impaired patients, amputees or patient with spinal cord injuries. One of such applications is the work of Pennycott and colleagues [30], in which they proposed a strategy aiming at estimating and controlling the work rate of the exercising individual by changing the level of assistance at the legs level. In their approach, both the target work rate and the estimated work rate are showed to the exercising individual, which then chooses the level of assistance in order to follow the reference. A similar human-in-the-loop strategy was later developed by Hunt and colleagues [21]. In their approach, the work rate was estimated using direct measurements of inhaled oxygen and exhaled carbon dioxide.

Some applications were based on the use of the electrical assistance of an e-bike. For example, Mayr and colleagues developed a prototype of what they call a *health e-bike* [3]. This electrical bike was designed as a rehabilitation tool aiming at controlling the power developed by the cyclist and avoid over-exercising. The strategy implemented was based on a bike equipped with an electric motor, a speed sensor and a torque sensor and the power regulation was ensured by a PI controller. A similar approach was proposed by Afonso and colleagues : using a rule-based controller they could regulate either the cycling torque [1] or the power output of the cyclist [2]. Instead of avoiding over exercising, the purpose of the application proposed by De la Iglesia and colleagues [11] was to use the commuting time spent on an electrical bicycle in order to train. Based on information such as the height and weight of the user, as well as knowledge of the route to be taken, their algorithm chooses the assistance level for different bouts of the path. The assistance level is derived algebraically from an estimation of the forces applied on the bike. Their application is coupled with an app aiming at promoting exercise by tracking the user's progression and comparing it with the one of other users. Wan and colleagues proposed a cycling power management strategy to optimally assist the cyclist based on a fatigue model, the status of the battery and the inclination of the road [39]. Finally, Mayerhofer and colleagues proposed a model between the cycling cadence and the power output on flat surfaces [25]. They used this model in order to develop a power output control strategy based on a PI controller. In this strategy, the output of the controller is a periodic sound signal played to the cyclist and whose frequency is used to adjust the pedaling frequency to meet the reference power output.

5.1.3 Control of heart rate during exercise

Many applications have been proposed in order to regulate the heart rate during exercise. These applications often use cycle-ergometers, e-bikes or treadmills. In this section, we focus on the solutions involving cycle-ergometers and e-bikes. Additional references are given in Table 5.1 regarding other kinds of systems.

For indoor training and rehabilitation, heart rate control solutions have been developed using cycle-ergometers. For example, Paradiso and colleagues proposed a nonlinear controller in order to regulate both the heart rate and heart rate variability during exercise [29]. Leitner and colleagues proposed to use a linear quadratic regulator (LQR) coupled with heart rate and ventilation measurement in order to regulate heart rate during exercise. However, the linear model they proposed supposed an aerobic regime of effort. More recently, Verrelli and colleagues made theoretical contributions to the problem of control heart rate based on a specific second order nonlinear model [38]. The solution they proposed could ensure the regulation of heart rate without taking into account stability and global attractivity constraints, common for this kind of system.

To make outdoor training possible and to ensure the autonomy of the user, applications involving e-bikes were also proposed. Meyer and colleagues proposed a nonlinear controller in order to regulate heart rate during cycling using the electrical assistance of the bike [27]. The controller is constituted of a feedback component based on a heart rate measurement and a feedforward component based on an estimation of the cycling torque applied by the cyclist at the desired heart rate. The controller is designed to reject disturbances such as the wind or the road slope. The bike is equipped with sensors monitoring the cycling speed and torque and the heart rate of the cyclist is measured by a chest strap. Corno and colleagues proposed to regulate the heart rate during exercise by piloting a continuously varying transmission system on the bike [10]. To do so, they modeled both the bike and the cyclist and proposed two different controllers : a proportional integral controller and a second-order sliding mode controller. Both controllers were compared experimentally and were successful in regulating the heart rate. Finally, Neuber and colleagues developed an e-bike to train safely. They tested both a PI and a PID controller which were calibrated heuristically to different users [28]. The controllers were tested for heart rate values ranging between 60% and 100% of the maximal heart rate.

5.1.4 Control of respiratory gas exchange during exercise

Regarding the control of respiratory gas exchange, all the applications found in the literature are dedicated to the control of the oxygen consumption during exercise. Most of these applications are designed for treadmill exercise. Hunt and colleagues were involved in multiple studies aiming at modelling and controlling the oxygen consumption of a training individual during robotic gait treadmill exercises. In [14], a dynamic output feedback was designed and tested in simulation in order to produce a linear increase in oxygen uptake during exercise by controlling the work

Authors	Year	Activity	Strategy
Su et al. [37]	2007	Treadmill	$\mathcal{H}_\infty$ controller
Cheng et al. [9]	2008	Treadmill	Switched LQ controller
Su et al. [36]	2010	Treadmill	MPC
Mazenc et al. [26]	2010	Treadmill	Nonlinear controller
Zhang et al. [40]	2012	Treadmill	Switched MPC
Scalzi et al. [34]	2012	Treadmill	Nonlinear controller
Sarabadami et al. [33]	2015	Rehabilitation	Self learning fuzzy controller
Argha et al. [4]	2015	Ergometer	Adaptive integral sliding-mode controller
Asheghan et al. [6]	2016	Treadmill	Nonlinear controller
Hunt et al. [18]	2016	Treadmill	Nonlinear controller
Girard et al. [13]	2016	Treadmill	Robust PID
Hunt et al. [15]	2016	Treadmill	Nonlinear controller
Ibeas et al. [22]	2016	Treadmill	Linear state feedback
Argha et al. [5]	2016	Ergometer	PID controller
Hunt et al. [16]	2017	Treadmill	Stochastic optimal controller
Hunt et al. [17]	2018	Treadmill	Optimal controller
Esmaeili et al. [12]	2019	Treadmill	Robust controller
Hunt et al. [19]	2019	Treadmill / ergometer	Nonlinear controller

Table 5.1: Heart rate control strategies in the literature.

rate of the individual. In [20], two dynamic output feedback controllers were used to control the oxygen consumption and the speed of a treadmill in order to produce a step response in the oxygen consumption. The method was validated experimentally. In [31], two dynamic output feedback controller were used to control the oxygen consumption and the work rate during treadmill exercise. The method was validated experimentally. In [35], a linear model of consumed oxygen during exercise was used to control the oxygen consumption during treadmill exercise. A dynamic output feedback was used to control the oxygen consumption while a human-in-the-loop controller was used to control the work rate of exercise. This approach was used to track oxygen consumption ramps experimentally. Finally, in [32], a similar approach was adapted to the control of oxygen consumption during stair climbing exercises.

Very few examples of control of oxygen during biking exercise can be found in the literature. One can mention the PhD work of Baig [7] dedicated to the modelling and control of oxygen consumption during rythmic exercises. As part of this PhD work, one paper was published describing a human-in-the-loop solution to control oxygen consumption. This strategy is based on a *self bio-feedback* controller, consisting in a flashing indicator used to require the user to increase, decrease or stabilize the exercise rate (corresponding to the pedaling cadence in biking) [8]. The objective of this controller was to keep the oxygen consumption between a 5% range of a reference oxygen consumption. The method was validated experimentally.

5.1.5 Contribution of the thesis

In the next Section, the contribution of the thesis regarding the control of physiological variables during cycling is presented. Two different control strategies are proposed and compared in simulation and experimentally. The first approach is based on a proportional integral (PI) controller and the second on a linear quadratic regulator (LQR) with integral action. The two control strategies are used in order to regulate the respiratory gas exchanges of the cyclist during exercise, more precisely the oxygen consumption or the carbon dioxide production.

5.2 Regulation of respiratory gas exchange using a proportional integral controller

The first approach to control respiratory gas exchange presented in this thesis is based on a Proportional Integral (PI) controller. It is applicable to the control of the oxygen consumption or of the carbon dioxide production during exercise. In this section, the formulation of the controller is presented and then its performances are assessed in simulation.

5.2.1 Problem Statement

In order to regulate respiratory gas exchange during biking exercise, the strategy proposed in this thesis is to control the electrical assistance level the e-bike automatically. This strategy is fairly intuitive : because it is not possible to control the biking conditions (slope, wind, etc.) at all time, the electrical assistance is used to *adjust* the mechanical load undergone by the cyclist. When the load is too large, the assistance level increases, and when it is too small, the assistance level decreases.

This intuition can be put in equations. In Chapter 3, the fundamental principle of dynamics applied to the contact point C between the rear wheel and the ground gives :

$$M_{tot} \cdot \frac{d\vec{v}}{dt} = \vec{\mathcal{F}}_{ext\{C\}} + \vec{\mathcal{F}}_{cyc\{C\}} + \vec{\mathcal{F}}_{mot\{C\}} \tag{5.1}$$

By computing the scalar product with the bike speed vector $\vec{v}$ on both sides of the equation we have :

$$M_{tot} \cdot \frac{d\vec{v}}{dt} \cdot \vec{v} = \vec{\mathcal{F}}_{ext\{C\}} \cdot \vec{v} + \vec{\mathcal{F}}_{cyc\{C\}} \cdot \vec{v} + \vec{\mathcal{F}}_{mot\{C\}} \cdot \vec{v} \tag{5.2}$$

This allows to formulate a relationship between the powers applied to the bike and the derivative of the kinetic energy $\mathcal{E}_c = \frac{1}{2} \cdot M_{tot} \cdot v^2$:

$$\frac{d\mathcal{E}_c}{dt} = \mathcal{P}_{ext} + \mathcal{P}_{cyc} + \mathcal{P}_{mot} \tag{5.3}$$

which can be used to express the power developed by the cyclist :

$$\mathcal{P}_{cyc} = \frac{d\mathcal{E}_c}{dt} - \mathcal{P}_{ext} - \mathcal{P}_{mot} \tag{5.4}$$

We can then replace the input of the respiratory gas exchange model presented in Chapter 3 to obtain :

$$\begin{cases} \mathbf{x}_{k+1} &= \mathbf{A}\mathbf{x}_k + \mathbf{B}(\frac{d\mathcal{E}_c}{dt} - \mathcal{P}_{ext} - \mathcal{P}_{mot}) + \mathbf{B}w_0 \\ \mathbf{y}_k &= \mathbf{C}(\rho_k)\mathbf{x}_k \end{cases} \tag{5.5}$$

which can then be expressed as :

$$\begin{cases} \mathbf{x}_{k+1} &= \mathbf{A}\mathbf{x}_k - \mathbf{B}u_k + \mathbf{B}d_k + \mathbf{B}w_0 \\ \mathbf{y}_k &= \mathbf{C}(\rho_k)\mathbf{x}_k \end{cases} \tag{5.6}$$

Here, the new input of the system is $u = \mathcal{P}_{mot}$ and the term $d = \frac{d\mathcal{E}_c}{dt} - \mathcal{P}_{ext}$ is a state disturbance. One can notice that because u and d are affecting the states $\mathbf{x}$ of the system in the same way (through matrix $\mathbf{B}$), u can be used to cancel the influence of d. In other words, the *influence of the external actions* can be cancelled by choosing the *power of the electrical assistance* appropriately.

In this section, we propose to use a proportional integral controller in order to adapt $\mathcal{P}_{mot}$ in real time. Because the regulation of either the oxygen consumption mO_2 or the carbon dioxide production mCO_{2tot} can be performed, in the following we denote z the regulated output, which is expressed as :

$$z_k = \mathbf{H}\mathbf{C}(\rho_k)\mathbf{x}_k \tag{5.7}$$

with $\mathbf{H}$ a constant matrix. In the case of the oxygen consumption regulation, we have $\mathbf{H}_{O2} = \begin{pmatrix} 1 & 0 \end{pmatrix}$ and in the case of the carbon dioxide production, we have $\mathbf{H}_{CO2} = \begin{pmatrix} 0 & 1 \end{pmatrix}$.

Here, we assume that z is known (by measurement or estimation) at all time and is used to compute successively the tracking error e, the cumulative sum of the errors s and the control input u as follows :

$$e_k = z_k - z_{ref} \tag{5.8}$$

$$s_{k+1} = s_k + e_k \tag{5.9}$$

$$u_k = K_p e_k + K_i s_k \tag{5.10}$$

with K_p the proportional gain and K_i the integral gain. The methodology used to tune K_p and K_i is described in the next section. The implementation scheme of the PI controller for respiratory gas exchange estimation is given in Fig. 5.1.

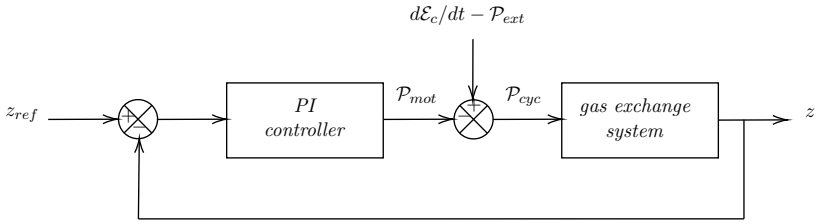

Figure 5.1: Implementation scheme of the PI controller.

5.2.2 Tuning of the proportional integral controller gains

Depending on the value chosen for the PI gains K_p and K_i, the behaviour of the closed loop system can change dramatically. For the safety of the e-bike user, the gains of the controller are calibrated in simulation prior the practical implementation on the bike prototype. To do so, the simulation strategy presented in Chapter 3 is used.

The scenario is the following, a cyclist described by a fixed force-velocity characteristic is riding the bike on a flat surface. The bike is subject to two external forces : the friction of the air and the action of the electrical assistance. The electrical assistance level is piloted by the PI controller, whose gains K_p and K_i are chosen beforehand, in order to ensure the regulation of the oxygen consumption of the cyclist to $z_{ref} = 1.8\ g/min$. Different sets of gains are compared in terms of settling time, control effort and overshoot.

Four different controllers C_1, C_2, C_3 and C_4 are presented. The value of their respective gains K_p and K_i are given in Table 5.2. The evolution of the regulated variable as well as the control effort for the different controllers is described in Fig. 5.2.

Controller	K_p	K_i
C_1	10	0
C_2	10	2
C_3	30	1.5
C_4	10	0.15

Table 5.2: Gain sets of the different controller.

From Fig. 5.2 one can notice that for each controller, the control effort settles at a negative value. This can be explained by the fact that the reference oxygen consumption to track $z_{ref} = 1.8\ g/min$ implies an energy expenditure higher than the basal power w_0, thus the cyclist has to perform an additional effort in order to reach it. This additional effort is ensured by a *load* imposed by the electrical assistance to the cyclist, which explains its negative value. The first controller to be proposed is the controller C_1. This controller is a fully proportional controller with no integral component. One can notice that such controller fails in regulating the oxygen consumption to the reference value due to the classical steady state error associated with proportional controllers. The second and third controllers C_2 and C_3 are proportional integral controllers with different proportional and integral gains. One can notice that both

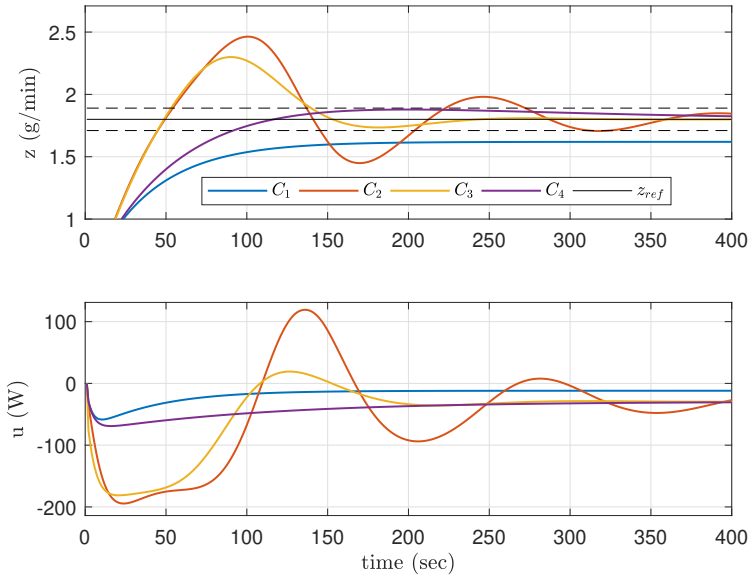

Figure 5.2: Comparison of four different controllers C_1, C_2, C_3 and C_4 in terms of time response *(first figure)* and in terms of control effort *(second figure)*. In the first figure, the reference $z_{ref} = 1.8\ g/min$ is plotted in black full line, the black dashed lines are drawn to assess $st_{5\%}$ the settling time at 5%.

controllers succeed in regulating z to the reference value. However, the time response of both controllers contains one or multiple overshoots and the control effort required is dramatically increased, especially at the start of the simulation when z is far from the reference. In practice, overshoot would imply periods of time when the cyclist is unable to exert mechanical power to the bike, since its velocity is entirely ensured by the electric motor. This should be avoided to guarantee a smooth ride to the user. Finally, a last proportional integral controller C_4 is considered. The integral gain chosen for this controller is significantly lower than the of one of C_2 and C_3. One can notice that the time response of z presents very little overshoot and that the control effort is significantly smoother than the ones of C_2 and C_3. Also, the settling time achieved by C_4 is significantly lower than the one of C_2 and C_3. However, since a strong integral term also ensure a better tracking of the reference controller C_3 is also a good candidate controller.

In the following section, controllers C_3 and C_4 are chosen and tested in simulation in a realistic scenario.

5.2.3 Validation of the proportional integral controller in simulation

In order to validate controllers C_3 and C_4, a new simulation scenario is considered. In real life applications, the cyclist and the e-bike are subject to external forces which need to be compensated by the electrical assistance. Here, we consider a scenario in which the slope of the

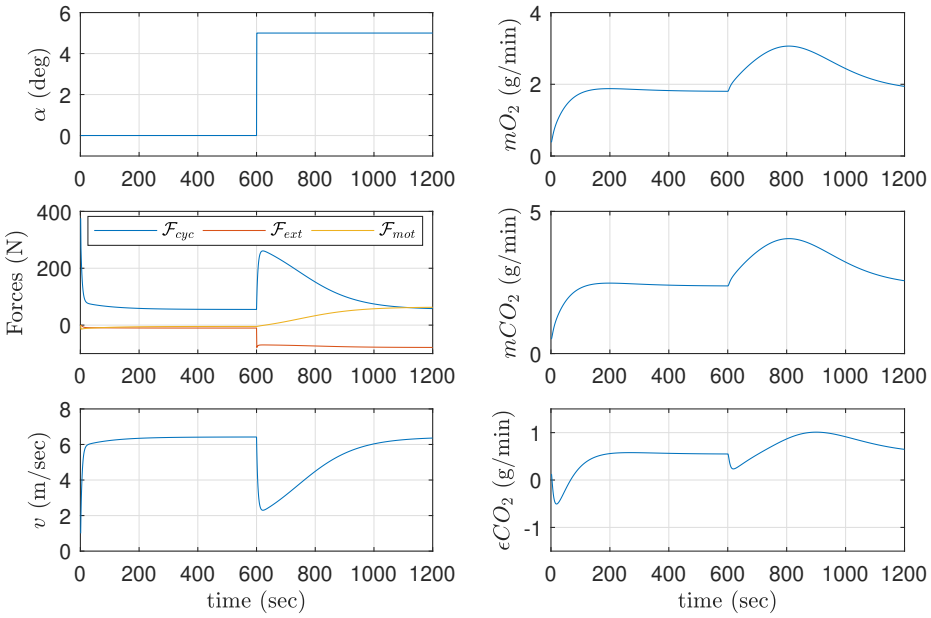

Figure 5.3: Evolution of the mechanical and physiological variables of the cyclist for the C_4 controller. The left column corresponds to the evolution of the mechanical variables, with first the slope of the road in degrees, then the forces applied on the bike and last the the speed of the bike. The right column corresponds to the evolution of the respiratory gas exchange variables, with first the oxygen consumption, then the aerobic carbon dioxide production and last the excess of carbon dioxide production.

road varies during the simulation. More precisely, in the first half of the simulation, the road is flat, and in the other half the the slope increases to $\alpha = 5°$.

First, controller C_4 is considered. Fig. 5.3 shows the evolution of the mechanical variables (slope of the road, forces affecting the bike, speed of the bike) and the physiological variables (oxygen consumption, carbon dioxide production and excess of carbon dioxide) of the system. One can notice that for each of the variables, two steady states are reached : a first one for the flat road portion and a second one for the positive slope road portion. For the C_4 controller, the first steady state is reached quickly on flat road, as it was designed for in the previous section. However, in the slope portion, this controller is much slower in regulating gas exchange variables to the reference value.

This slow convergence clearly appears is Fig. 5.4 which represents the evolution of the powers applied by the cyclist, exteriors forces and the electrical motor along time. The slope of the road changes at instant $t = 600sec$, which implies a dramatic increase in the power applied by the exterior forces due to the added contribution of gravity. This increase in $\mathcal{P}_{ext}$ implies an increase in the power developed by the cyclist $\mathcal{P}_{cyc}$, which has to be compensated by the electrical assistance which takes around $600sec$ to happen.

By looking at Fig. 5.5, one can notice that the slow compensation of $\mathcal{P}_{ext}$ by the electrical

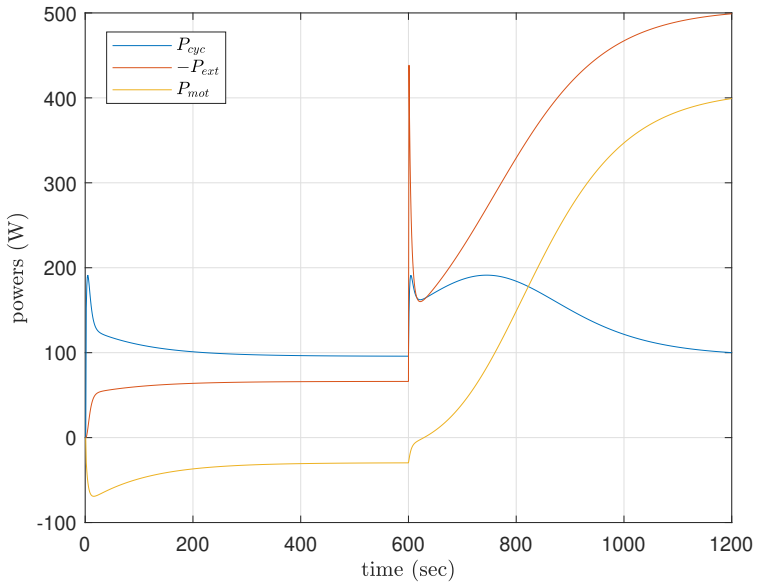

Figure 5.4: Evolution of the powers applied on the bike for the C_4 controller, with the power applied by the cyclist *(in blue)*, the power applied by the external forces *(in red)* and the power applied by the motor *(in yellow)*.

assistance implies a slow convergence of z to z_{ref}.

Then, we assess the performances of controller C_3 over the same scenario. By looking at Fig. 5.6 one can notice that both steady states are reached quickly. However, both responses contain an overshoot.

The fast convergence to steady state is explained by Fig. 5.7. Compared to controller C_4, controller C_3 is much quicker in compensating the external actions.

Finally, Fig. 5.8 shows that for both the flat portion and the slope portion the system reaches steady state in around $120sec$.

In conclusion, even though controller C_3 implies a higher control effort and an overshoot in the time response of the regulated z, it is still the best solution given that in a real scenario, the bike and the cyclist undergo external disturbances which have to be compensated quickly by the electrical assistance. In the following, we choose controller C_3 as the validated PI control solution.

5.3 Regulation of respiratory gas exchange using a linear quadratic regulator

In the previous section, the use of a proportional integral controller was proposed in order to regulate respiratory gas exchange during exercise. In this section, a different strategy based on

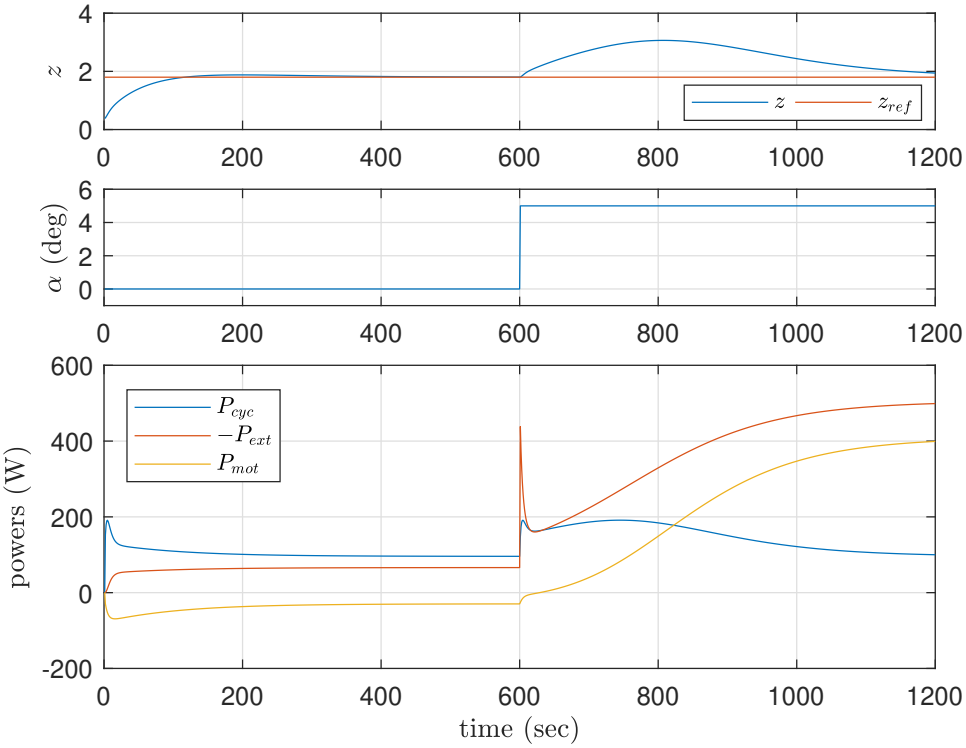

Figure 5.5: Evolution of the controlled output for the C_4 controller compared to the reference z_{ref} *(first figure)*, of the slope of the road in degrees *(second figure)*, and of the powers applied to the bike *(last figure)*.

a robust integral linear quadratic controller is proposed. First, the formulation of the controller is presented and then its performances are assessed in simulation.

5.3.1 Problem statement

The LQR is defined by a constant gain $\mathbf{K}$, which is used to compute the control action u as follows :

$$\mathbf{u}_k = -\mathbf{K}\mathbf{x}_k \tag{5.11}$$

The LQR is an optimal controller in the sense that the gain $\mathbf{K}$ is computed so that the following cost J is minimized :

$$J = \sum_{k=0}^{\infty} (\mathbf{x}_k^T \mathbf{Q} \mathbf{x}_k + \mathbf{u}_k^T \mathbf{R} \mathbf{u}_k) \tag{5.12}$$

with $\mathbf{Q}$ and $\mathbf{R}$ symmetric positive matrices. The idea is to use these matrices as design parameters in order to find a trade-off between the performances of the controller and the

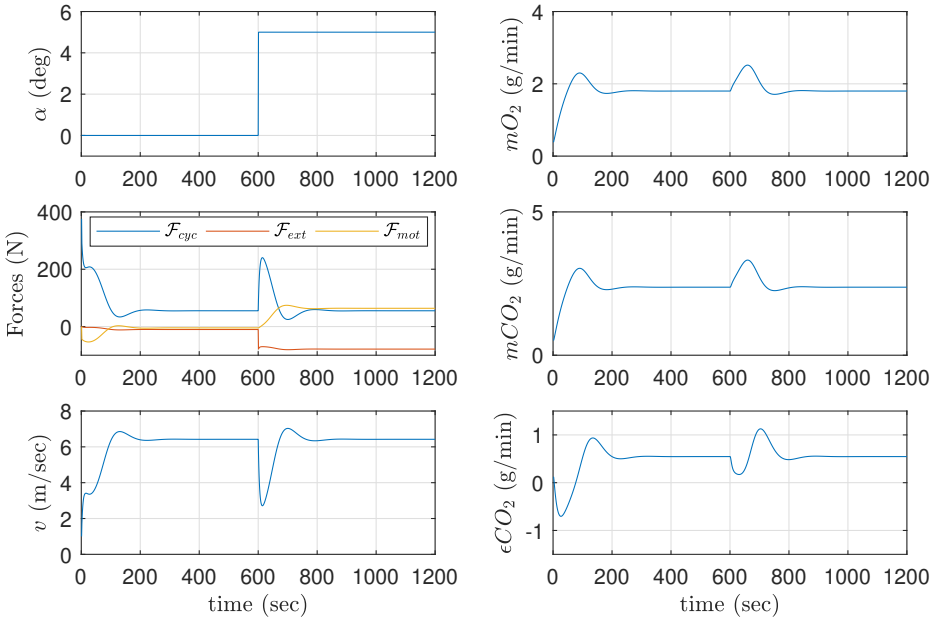

Figure 5.6: Evolution of the mechanical and physiological variables of the cyclist for the C_3 controller. The left column corresponds to the evolution of the mechanical variables, with first the slope of the road in degrees, then the forces applied on the bike and last the the speed of the bike. The right column corresponds to the evolution of the respiratory gas exchange variables, with first the oxygen consumption, then the aerobic carbon dioxide production and last the excess of carbon dioxide production.

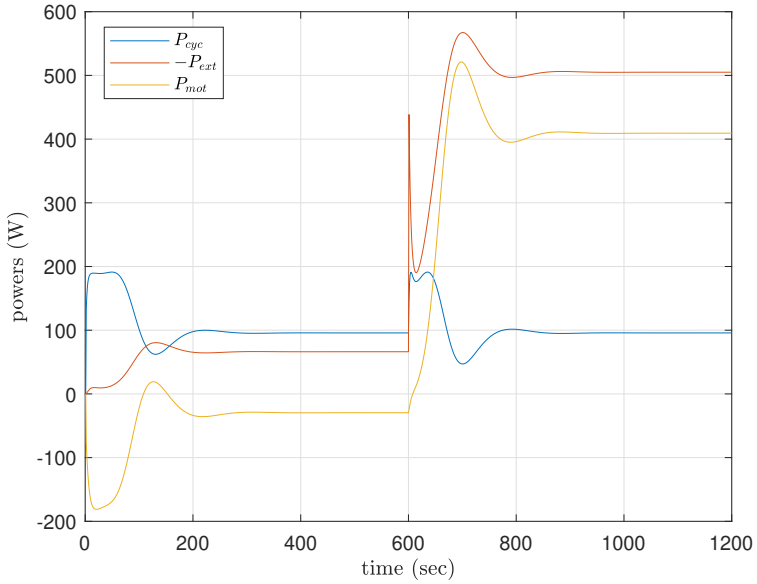

Figure 5.7: Evolution of the powers applied on the bike for the C_3 controller, with the power applied by the cyclist *(in blue)*, the power applied by the external forces *(in red)* and the power applied by the motor *(in yellow)*.

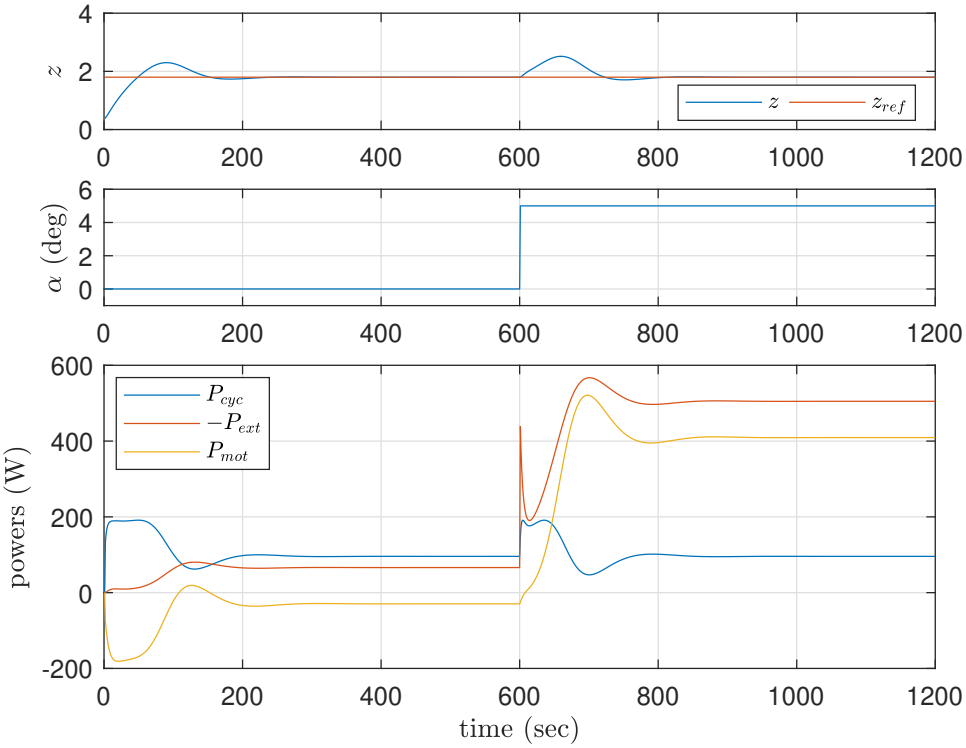

Figure 5.8: Evolution of the controlled output for the C_3 controller compared to the reference z_{ref} *(first figure)*, of the slope of the road in degrees *(second figure)*, and of the powers applied to the bike *(last figure)*.

control cost. For example, comparatively large coefficients in matrix $\mathbf{Q}$ compared to matrix $\mathbf{R}$ will produce a more aggressive controller with high convergence speed and tracking accuracy but at the cost of a large control effort. Similarly, comparatively large coefficients in matrix $\mathbf{R}$ compared to matrix $\mathbf{Q}$ will produce an economical controller but at the expense of the convergence speed and tracking accuracy. Because $\mathbf{Q}$ and $\mathbf{R}$ are matrices, this is also true component-wise, it is then possible to favor the aggressivity or the economy of some of the states compared to some others.

In order to design the linear quadratic regulator (LQR), the formulation of the respiratory gas exchanges model (5.6) proposed in the previous section is used. However, because an integral action is added, the dynamics of the system are extended in the following way :

$$\begin{cases} \tilde{\mathbf{x}}_{k+1} &= \tilde{\mathbf{A}}\tilde{\mathbf{x}}_k - \tilde{\mathbf{B}}u_k + \tilde{\mathbf{B}}d_k + \tilde{\mathbf{B}}\tilde{\mathbf{w}} \\ \tilde{\mathbf{y}}_k &= \tilde{\mathbf{C}}(\rho_k)\tilde{\mathbf{x}}_k \end{cases} \tag{5.13}$$

Here $\tilde{\mathbf{x}}_k = \begin{pmatrix} \mathbf{x}_k & s_k \end{pmatrix}^T$ with s_k the cumulative sum of the tracking error at instant k defined as in (5.8), $\tilde{\mathbf{w}} = \begin{pmatrix} w_0 & -z_{ref} \end{pmatrix}^T$ and :

$$\tilde{\mathbf{A}} = \begin{pmatrix} \mathbf{A} & 0 \\ \mathbf{HC}(\rho_k) & 1 \end{pmatrix}, \tilde{\mathbf{B}} = \begin{pmatrix} \mathbf{B} \\ 0 \end{pmatrix}, \tilde{\mathbf{C}}(\rho_k) = \begin{pmatrix} \mathbf{C}(\rho_k) & 0 \end{pmatrix}$$

In this thesis, the design of the LQR is based on the solution of a Linear Matrix Inequality (LMI) problem. The problem is expressed as follows :

Theorem 6. *Consider the system (5.13) and given symmetric definite positive matrices* $\mathbf{Q}$ *and* $\mathbf{R}$*. The robust LQR gain* $\mathbf{K}$ *which minimizes the cost* J *as defined in (5.12) is found if there exist a symmetric positive definite matrix* $\mathbf{P}$ *and matrices* $\mathbf{Y}$ *and* $\mathbf{W}$ *satisfying the following conditions :*

$$\begin{pmatrix} -\boldsymbol{P} + \boldsymbol{Q} & \tilde{\mathbf{A}}_0 \boldsymbol{P} - \tilde{\mathbf{B}} \boldsymbol{Y} \\ \star & -\boldsymbol{P} \end{pmatrix} \preceq 0 \tag{5.14}$$

$$\begin{pmatrix} -\boldsymbol{P} + \boldsymbol{Q} & \tilde{\mathbf{A}}_1 \boldsymbol{P} - \boldsymbol{Y} \\ \star & -\boldsymbol{P} \end{pmatrix} \preceq 0 \tag{5.15}$$

$$\begin{pmatrix} \boldsymbol{W} & \boldsymbol{C}_{lqr} \boldsymbol{P} + \boldsymbol{D}_{lqr} \boldsymbol{Y} \\ \star & \boldsymbol{P} \end{pmatrix} \succeq 0 \tag{5.16}$$

with $\boldsymbol{C}_{lqr} = \begin{pmatrix} \boldsymbol{Q}^{1/2} & 0 \end{pmatrix}$, $\boldsymbol{D}_{lqr} = \begin{pmatrix} 0 & \boldsymbol{R}^{1/2} \end{pmatrix}$ *and* $\mathbf{K} = \mathbf{Y}\mathbf{P}^{-1}$*. Matrices* $\tilde{\mathbf{A}}_0$ *and* $\tilde{\mathbf{A}}_1$ *correspond to the vertex matrices computed for* $\rho = 0$ *and* $\rho = 1$ *respectively.*

□

Unfortunately, this result was not be proved in the scope of this thesis. However, since Theorem 6 still led to interesting practical results the latter are presented in the following sections.

5.3.2 Validation of the linear quadratic regulator in simulation

In this section, the performances of the LQR are assessed in simulation and compared to the ones of the previous PI controller. As for the validation of the PI controller, the regulated output is the oxygen consumption and the scenario contains a flat road portion and a positive slope portion.

In order to compute a valid candidate for the LQR gain K, a similar tuning strategy as the one described in Section 5.2.2 is used. Here the following values for the design matrices are considered :

$$\mathbf{Q} = \begin{pmatrix} 1 & 0 & 0 & 0 \\ 0 & 0.01 & 0 & 0 \\ 0 & 0 & 0.01 & 0 \\ 0 & 0 & 0 & 1 \end{pmatrix}, \mathbf{R} = 0.0125$$

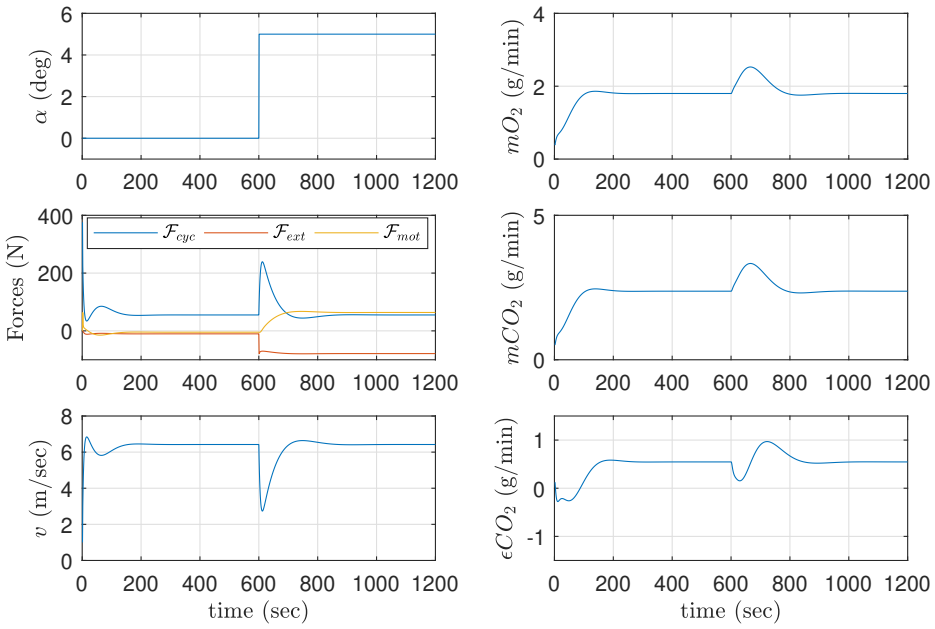

Figure 5.9: Evolution of the mechanical and physiological variables of the cyclist for the linear quadratic regulator (LQR). The left column corresponds to the evolution of the mechanical variables, with first the slope of the road in degrees, then the forces applied on the bike and last the the speed of the bike. The right column corresponds to the evolution of the respiratory gas exchange variables, with first the oxygen consumption, then the aerobic carbon dioxide production and last the excess of carbon dioxide production.

One can notice that larger values are given to the coefficients related the controlled output $z = x_1$ and the integral term $s = x_4$ in order to favor the states involved in the control. A smaller value is chosen for $\mathbf{R}$ in order to ensure a short settling time and a fast rejection the external disturbances.

Similarly to Section 5.2.3, the evolution of the physiological and mechanical variables of the system are shown in Fig. 5.9 and the evolution of the powers affecting the system in Fig. 5.10.

In Fig. 5.11, the evolution of the regulated variable is shown. It can be seen that the oxygen consumption is regulated to the reference value. Also, in comparison with the PI controller, the LQR ensures a tracking of the reference on flat road without overshoot. A comparison between the performances of the LQR with controllers C_3 and C_4 is shown in Fig. 5.12. This figure shows that the LQR ensures a fast convergence without overshoot on flat road similarly to the C_3 PI controller. However, on the slope portion, the LQR converges quickly to the reference similarly to the C_4 PI controller.

In conclusion, the LQR appears to be a good compromise between the previously proposed PI controllers C_3 and C_4, ensuring good performances on both flat roads and slopes.

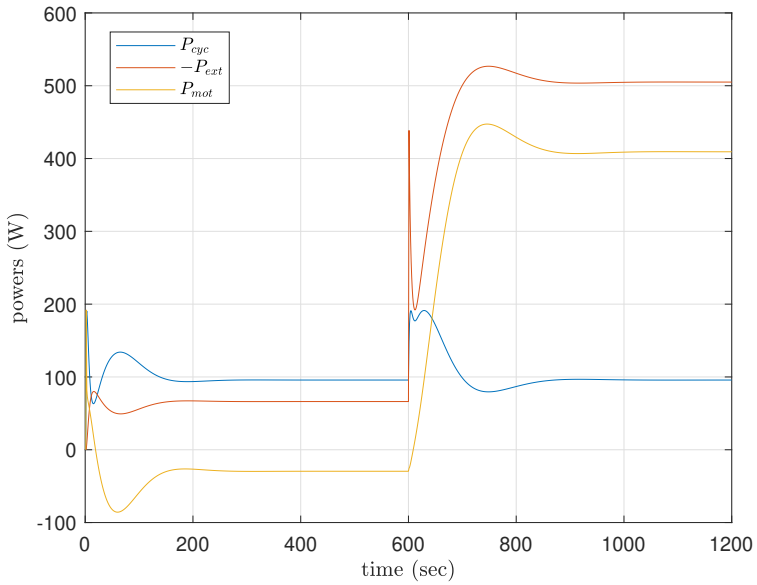

Figure 5.10: Evolution of the powers applied on the bike for the linear quadratic regulator (LQR), with the power applied by the cyclist *(in blue)*, the power applied by the external forces *(in red)* and the power applied by the motor *(in yellow)*.

5.4 Contribution of physiological control strategies

In the previous sections, control laws were proposed in order to control respiratory gas exchange during exercise. However, one can wonder about the practical interest of such strategy. In this section, we study the differences in terms of oxygen consumption for the rider between a bike without electrical assistance, a bike equipped with an amplifying assistance and a bike equipped with the proposed LQR strategy.

One of the most common control approach for the electrical assistance of e-bikes is the *amplifying* strategy. Based on an estimation or a measure of the force to torque applied by the cyclist to the bike, this strategy uses the electric assistance of the bike to amplify the action of the cyclist on the bike. It is formulated in the following way :

$$\mathcal{F}_{mot} = K_{amp}\mathcal{F}_{cyc} \tag{5.17}$$

with K_{amp} a nonzero positive scalar. Such control law artificially makes the rider stronger, and thus alleviate the perceived load.

The comparison between the different electrical assistance strategies is shown in Fig. 5.13. The simulation scenario is the same as the one used for the validation of the PI controller and the LQR, with a flat road during the first half of the simulation and a positive slope in the second half. The oxygen consumption z and the power of the electrical assistance u are shown in blue lines for the bike without electrical assistance. Here, the power developed by

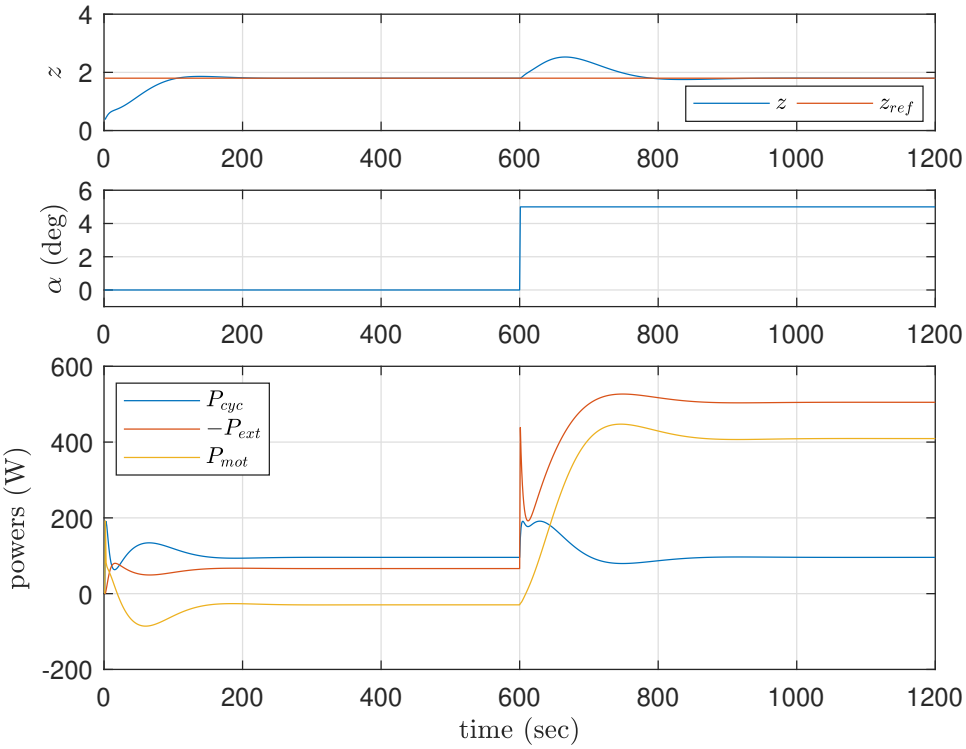

Figure 5.11: Evolution of the controlled output for the linear quadratic regulator (LQR) compared to the reference z_{ref} *(first figure)*, of the slope of the road in degrees *(second figure)*, and of the powers applied to the bike *(last figure)*.

the cyclist depends directly on the road slope since no assistance is provided to the cyclist. In this simulation, the amplifying strategy is defined with a gain $K_{amp} = 2$. Using this control strategy reduces the load perceived by the cyclist and, compared to the scenario without assistance, the oxygen consumption of the cyclist stabilizes at lower values, which is explained by a reduced physiological stress for the cyclist. However, even with the amplifying strategy, the power developed by the cyclist depends on the road slope. Finally, with the LQR the electrical assistance adapts to the road condition and ensures a steady oxygen consumption during the ride as shown in the previous section.

Thus, we showed that a dedicated control strategy is the only way to truly regulate the physiological response of the cyclist to exercise.

5.5 Experimental validation of the linear quadratic regulator and proportional integral controller

In the previous sections, two strategies for the regulation of respiratory gas exchanges during exercise, based respectively on a PI controller and a LQR, were formulated and validated in

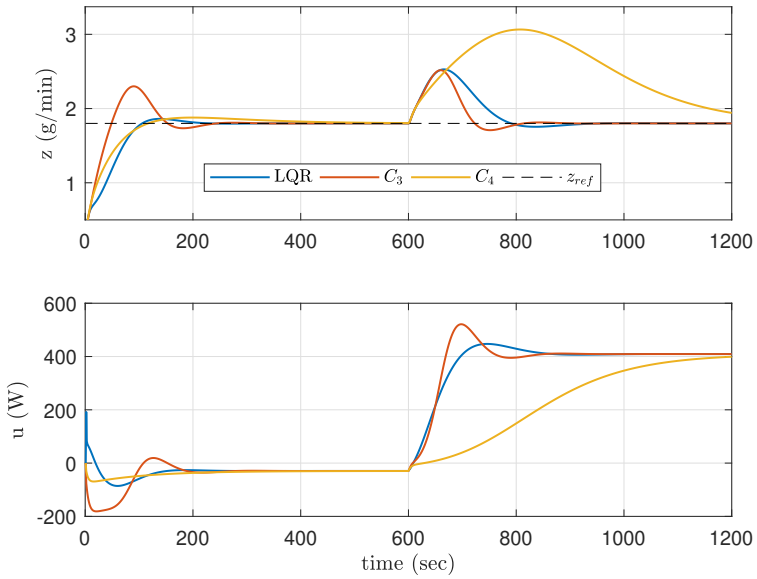

Figure 5.12: Comparison of the linear quadratic regulator (LQR) with the proportional integral (PI) controllers C_3 and C_4 in terms of time response *(first figure)* and in terms of control effort *(second figure)*.

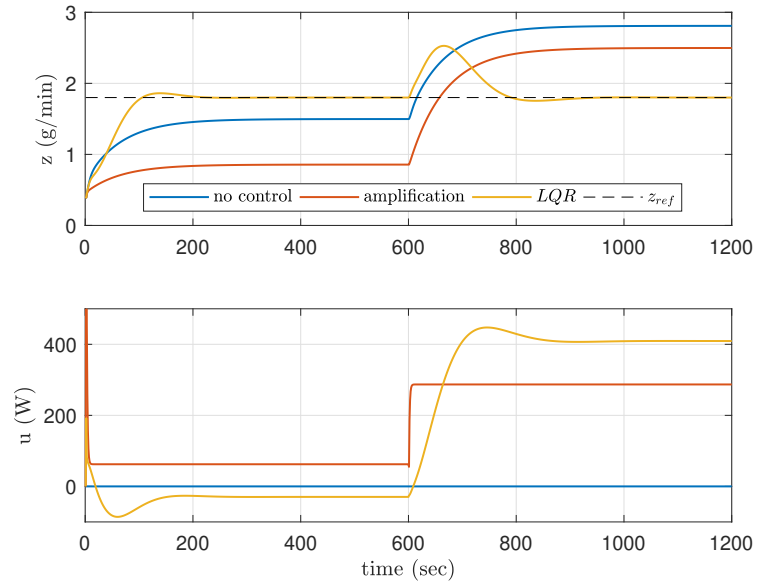

Figure 5.13: Evolution of the oxygen consumption of the cyclist without electrical assistance *(in blue)*, with the amplifying controller *(in red)* and with the linear quadratic regulator (LQR) *(in yellow)*. The oxygen consumption of the cyclist is shown in the first figure and the power applied by the motor is shown in the second figure.

Figure 5.14: SPIRO E-bike prototype developed at Gipsa-lab.

simulations. In this section, experimental results obtained using both control strategies are presented.

5.5.1 Experimental setup and scenario

In order to validate the respiratory gas exchanges control strategies, the control laws are coded and implemented on an e-bike prototype developed in Gipsa-lab. A picture of the e-bike prototype is showed in Fig. 5.14. The control laws are used in order to control the electrical assistance of the bike.

To implement the control laws, some knowledge about the states of the system are required. For the PI controller the regulated variable z is supposed known at all times in order to compute the tracking error e. For the LQR, the full states of the respiratory gas exchanges model $\mathbf{x}$ are supposed to be known. Because a full implementation of the control strategies using direct measurement of respiratory gas exchanges and/or a state observer could not be performed, a non-invasive approach was used. Instead of measuring directly respiratory gas exchanges and estimating the state variables, the gas exchanges model was used to predict respiratory gas exchanges in *open-loop* based on the computation of the mechanical power developed by the cyclist on the pedal. The implementation scheme is given in Fig. 5.15.

Different scenarios are considered to assess the performances of the control laws. First, the control laws are validated *indoor*. To do so, the electrical motor of the bike is used to generate the road profile as well as the assistance. The road profile is generated as a torque load step profile with $\mathcal{C}_{ext} = 5\ Nm$ between $t = 0\ sec$ and $t = 300\ sec$, with $\mathcal{C}_{ext} = 10\ Nm$ between

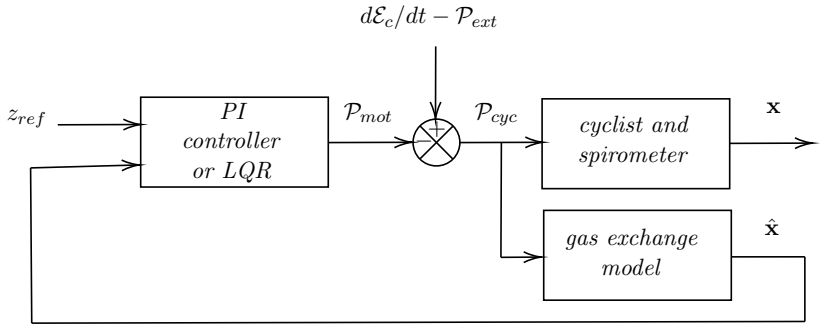

Figure 5.15: Implementation scheme of the control strategies for the experimental validation scenarios.

$t = 300\ sec$ and $t = 600\ sec$ and with $\mathcal{C}_{ext} = 5\ Nm$ between $t = 600\ sec$ and $t = 900\ sec$. Then, the control laws are validated *outdoor*. To do so, a path was defined and biked through using each control strategy. When a control law was used, the goal was to regulate the oxygen consumption of the cyclist to a reference $z_{ref} = 1.2\ g/min$. A summary of the different scenarios is given in Table 5.3.

Name	Location	Controller
In0	Indoor	No assistance
In1	Indoor	PI controller
In2	Indoor	LQR
Out0	Outdoor	No assistance
Out1	Outdoor	PI controller
Out2	Outdoor	LQR

Table 5.3: Experimental scenarios.

For the indoor and the outdoor tests the respiratory gas exchanges data were collected using the portable ergospirometer *Cortex Metamax 3B*. The mechanical variables of pedalling torque and pedalling cadence were measured directly on the e-bike prototype. Since the signals are affected by a fair amount a noise, filtered versions are sometimes included in the next sections and are labeled with $(\mathcal{F}_n)$ with n the size of the moving average window used for filtering. The measured ones are labeled with $(\mathcal{M})$. An example of an original oxygen consumption signal and its filtered version is presented in Fig. 5.16.

For the sake of comparison, the scenarios *In0* and *Out0* are performed with using the electrical assistance. The results of scenario *In0* are showed in Fig. 5.17 and the results of scenario *Out0* are show in Fig. 5.18. The reference oxygen consumption $z_{ref} = 1.2\ g/min$ was chosen so that it is exceeded by the cyclist without using a control strategy. The power profiles of the indoor and outdoor tests are very different, which allows to draw different conclusions from each test.

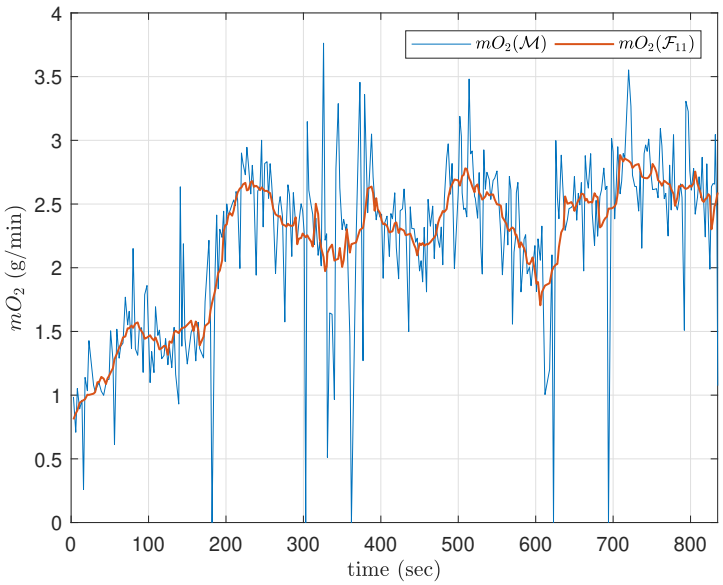

Figure 5.16: Comparison of the oxygen consumption signal mO_2 before and after filtering for the *In0* scenario. Here the filter applied is a moving average filter with a window size of $n = 11$ samples.

5.5.2 Validation of the proportional integral controller

In this section the results obtained with the PI controller are presented. The controller C_3, with gains $K_p = 30$ and $K_i = 1.5$, is used.

The results of the indoor test *In1* are showed in Fig. 5.19. In this test, both the estimated oxygen consumption from the model and the real oxygen consumption are regulated to the desired value $z_{ref} = 1.2\ g/min$. However, since the model estimation of mO_2 is fed to the PI controller, mO_2 *model* is regulated more accurately. In the first minute of the simulation, the PI controller increases the load perceived by the cyclist in order to fasten the convergence of mO_2 to the reference and an overshoot occurs for both the measured and estimated mO_2. When the step in $\mathcal{C}_{ext}$ occurs at $t = 300\ sec$, the controller increases the assistance provided to the cyclist in order to reject the disturbance.

The results of the outdoor test *Out1* are showed in Fig. 5.20. In this test, the external forces profile is not as steady as for the indoor scenario. The variations of the road slope and cycling conditions make it harder for the controller to regulate the oxygen consumption. Both the estimated and the measured oxygen consumption show oscillations around the reference value z_{ref}. In this scenario, because the value chosen for the reference oxygen consumption z_{ref} is low, the control effort applied by the electrical assistance to maintain it is pretty high, up to 300 $Watts$.

In both scenarios, the control law successfully regulated the real oxygen consumption of the cyclist around the reference value. However, oscillations and overshoots occur, especially in the

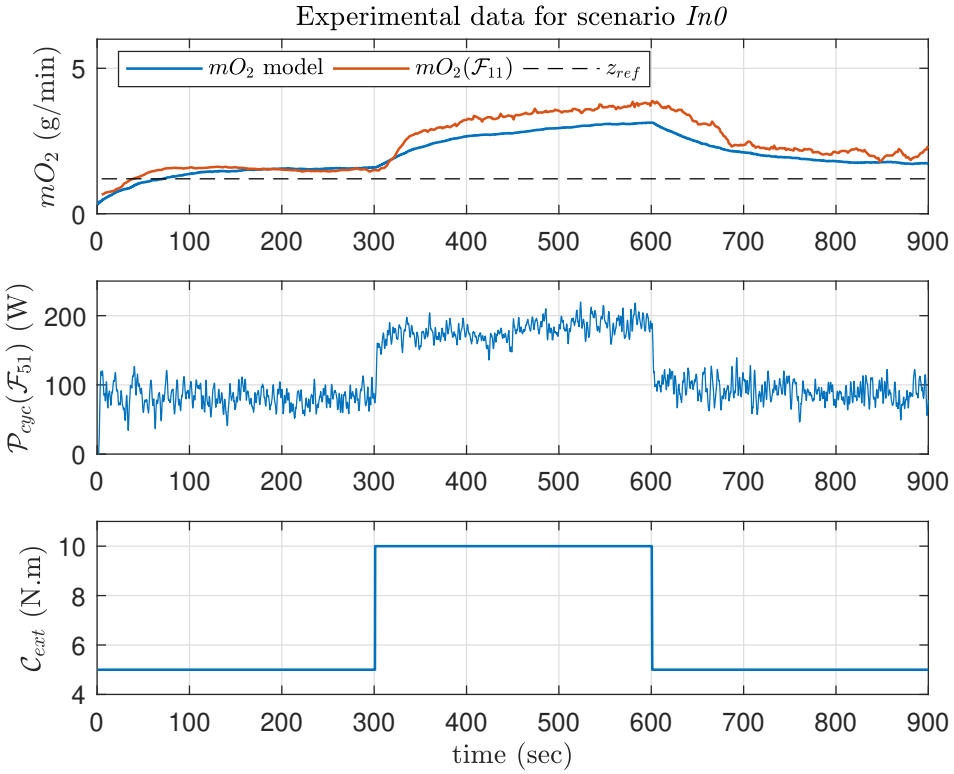

Figure 5.17: Evolution of the cyclist oxygen consumption *(first figure)*, of the power developed by the cyclist *(second figure)* and of the external torque profile *(last figure)* for scenario *In0*. No control strategy is used. The test is performed indoor.

outdoor scenario, which need to be reduced to improve the performances of the control strategy.

5.5.3 Validation of the linear quadratic regulator

In this section the results obtained with the LQR are presented. The controller is defined as in Section 5.3.2.

The results of the indoor test *In1* are showed in Fig. 5.21. The intended scenario was the same as for tests *In0* and *In1*, however, due to a technical defect, the torque load $\mathcal{C}_{ext}$ was not applied during the test. Thus, instead of 3 different external torque steps, no external torque was applied. In these conditions, the electrical assistance had to provide the load applied to the cyclist in order to regulate the oxygen consumption to the reference z_{ref}. Fig. 5.21 shows that after a transient of around 2 min the oxygen consumption stabilizes around the reference thanks to the action of the electrical assistance which stabilizes around -40 Watts. This test questions the choice of a low reference for the oxygen consumption, since a 40 Watts exercise intensity is not realistic to ensure in an open road scenario.

The results of the outdoor test *Out1* are showed in Fig. 5.22. In this scenario, the estimated oxygen consumption from the model was properly regulated around the reference, however

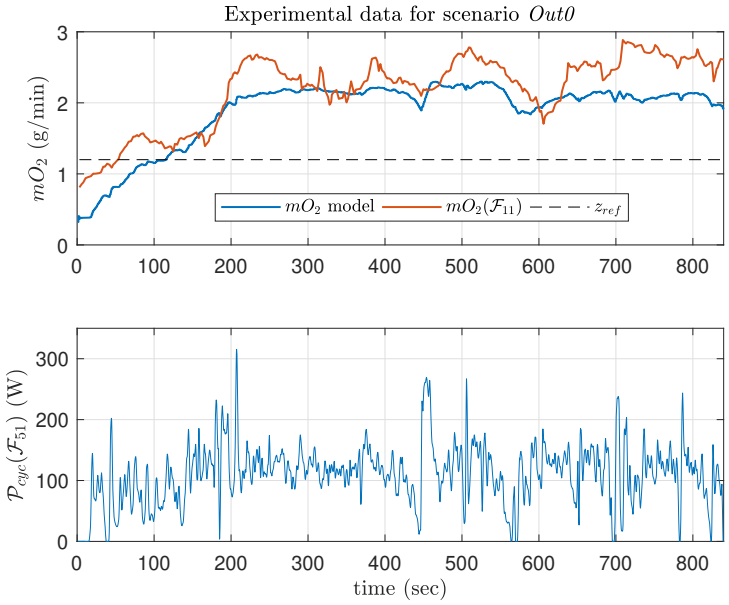

Figure 5.18: Evolution of the cyclist oxygen consumption *(first figure)* and of the power developed by the cyclist *(second figure)* for scenario *Out0*. No control strategy is used. The test is performed outdoor.

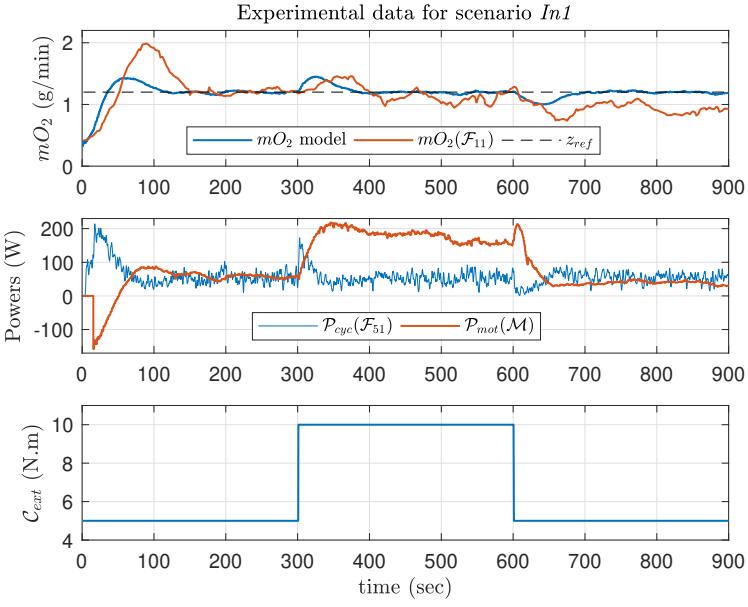

Figure 5.19: Evolution of the cyclist oxygen consumption *(first figure)*, of the power developed by the cyclist and the motor *(second figure)* and of the external torque profile *(last figure)* for scenario *In1*. The PI control strategy is used. The test is performed indoor.

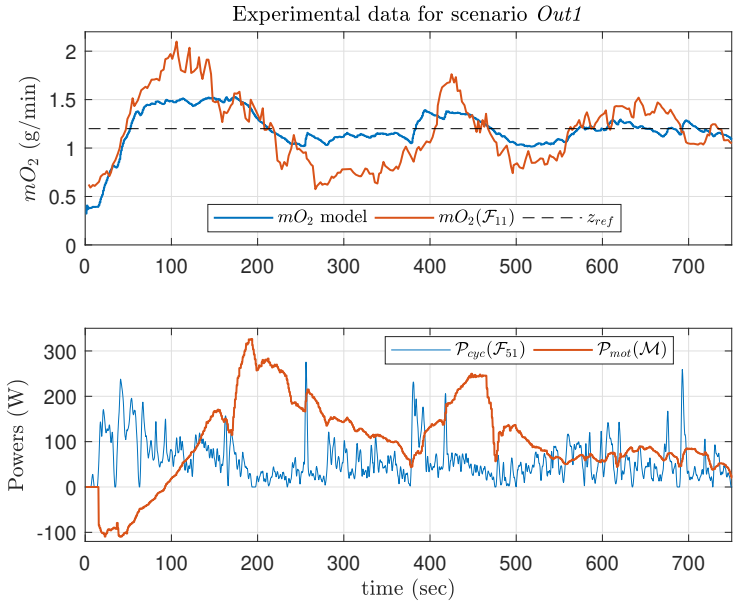

Figure 5.20: Evolution of the cyclist oxygen consumption *(first figure)* and of the power developed by the cyclist and the motor *(second figure)*, for scenario *Out1*. The PI control strategy is used. The test is performed outdoor.

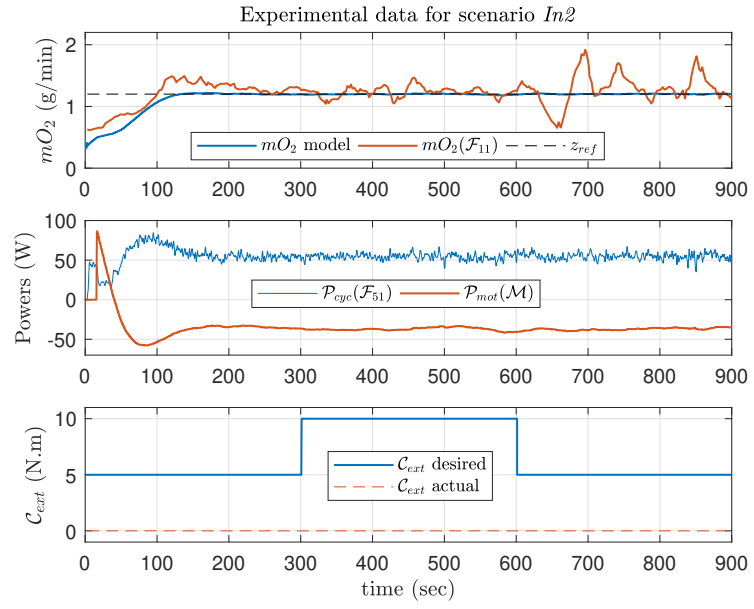

Figure 5.21: Evolution of the cyclist oxygen consumption *(first figure)*, of the power developed by the cyclist and the motor *(second figure)* and of the external torque profile *(last figure)* for scenario *In2*. The LQR strategy is used. The test is performed indoor.

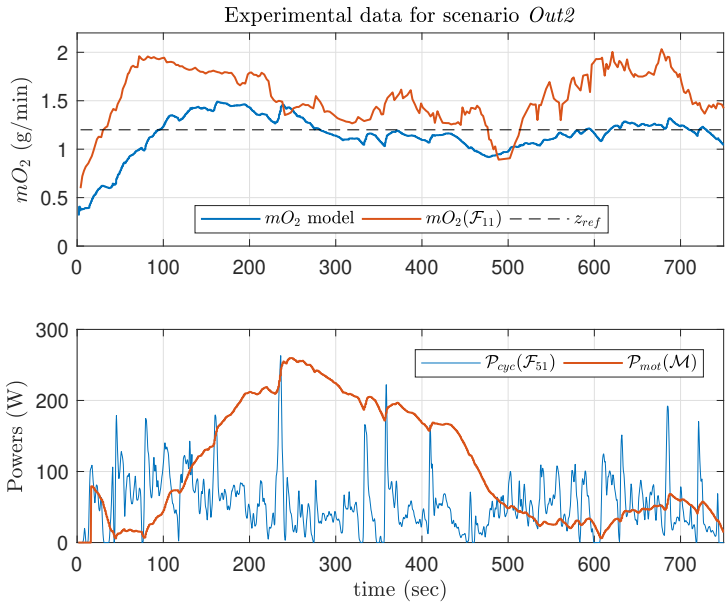

Figure 5.22: Evolution of the cyclist oxygen consumption *(first figure)* and of the power developed by the cyclist and the motor *(second figure)*, for scenario *Out2*. The LQR strategy is used. The test is performed indoor.

the measured oxygen consumption did not follow the same trajectory. The fact that the performances of the LQR appear worse than the performances of the PI controller for the outdoor test can be explained that in order to be implemented, the PI controller solely depends on an oxygen consumption estimation (which is usually well provided by the gas exchanges model) while the LQR requires a full knowledge of the system, which is harder to ensure. During this test, the electrical assistance exclusively assisted the cyclist, to up to 250 $Watts$.

5.5.4 Conclusion

Several conclusions can be drawn from the experimental results previously presented :

- *C1 - Both control strategies showed a significant effect on the oxygen consumption of the cyclist during exercise compared to a ride without electrical assistance.*
- *C2 - Both control strategies managed to regulate the estimated oxygen consumption of the model around the reference value which is very encouraging. The PI controller showed more oscillations compared to the LQR.*
- *C3 - The ability of the control strategies to regulate the real oxygen consumption is less clear however. Here the implementation scheme chosen makes it so that the controllers are not aware on a measured value of the regulated signal z and solely depends on its estimation provided by the gas exchange model. To conclude on the ability of the control*

strategies to regulate the real oxygen consumption of the cyclist, further tests are needed with a more accurate estimation and/or a direct measurement of the respiratory gas exchanges.

5.6 Experimental validation of the simulation strategy

In the previous section, experimental results obtained using the two control strategies were presented. The availability of experimental data represented the opportunity to validate the simulation strategy proposed in Chapter 3 and used for the tuning of the controllers. In order to do so, the indoor scenarios *In0* and *In1* are reproduced in simulation and the simulation results are compared to the experimental results. This is particularly interesting because, in order to perform the simulations, the behaviour of the cyclist is modeled under the form of a cyclist force-velocity characteristic identified using experimental data. Thus it is not obvious *a priori* that such model is valid and produces a realistic cycling behaviour.

5.6.1 Validation on scenario *In0*

First, the indoor scenario *In0*, with no electrical assistance, is reproduced in simulation. The evolution of the respiratory gas exchanges and the power developed by the cyclist is presented in Fig. 5.23. From this figure, it can be seen that the respiratory gas exchanges are reproduced accurately in the aerobic region (low intensity effort) but show a slight mismatch in high intensity effort. The power developed by the cyclist however is very accurately estimated in simulation, which is a very important feature since the estimation of the respiratory gas exchanges directly depends on it.

The evolution of the power developed by the cyclist in simulation is associated with the choice made for the cycling force-velocity characteristic. This characteristic is defined as a rigid relationship between the pedaling force and the pedaling speed, and was chosen linear in this thesis. In Fig. 5.25, the evolution of the measured pedalling speed and torque as well as their simulated equivalents are shown. From this figure, it can be seen that for the low intensity segments of the scenario, the pedalling speed and the pedalling torque are predicted accurately. However, in the high intensity segment, the simulation predicts a decrease in pedalling speed coupled with an increase in pedalling torque, that does not happen in practice. Here, it seems that the cyclist is regulating the pedalling speed to a fixed value throughout the session, which is not reproduced by the characteristic.

Finally in Fig. 5.25, the force-velocity and the power-velocity characteristics are compared to the simulated and measured data. It is interesting to see that initially, the experimental data points lie on both characteristics. However, in the high intensity segment of the scenario, the experimental data points translate vertically instead of following the characteristics because of the fixed pedalling velocity chosen by the cyclist. When the power-velocity is considered,

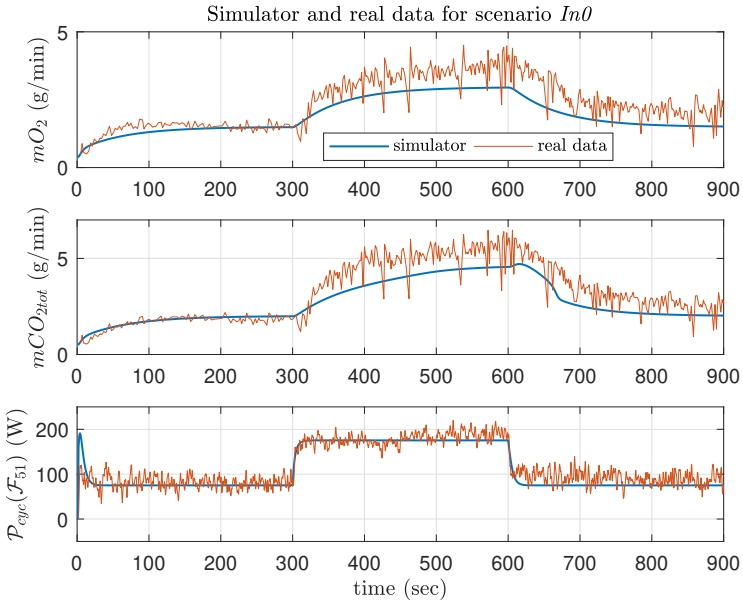

Figure 5.23: Evolution of the real and simulated cyclist oxygen consumption *(first figure)*, total carbon dioxide production *(second figure)*, and power developed by the cyclist *(last figure)* for scenario *In0*.

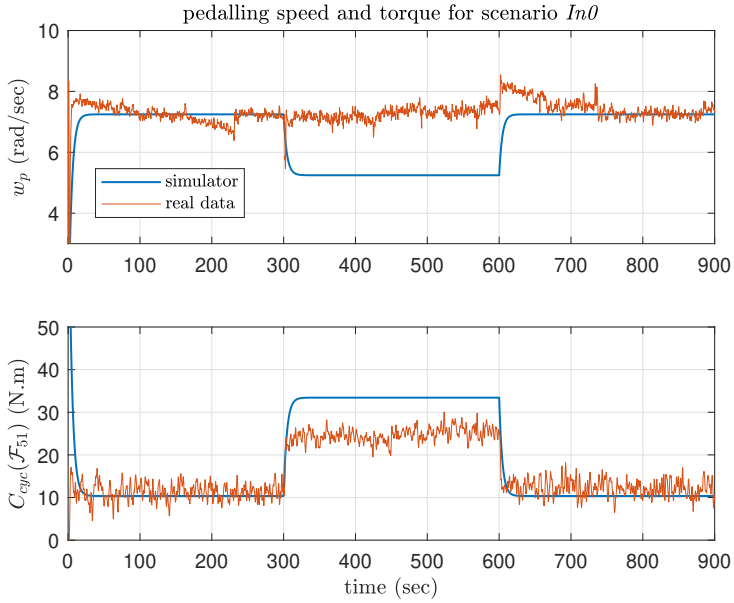

Figure 5.24: Evolution of the real and simulated pedalling speed *(first figure)* and pedalling torque *(second figure)* for scenario *In0*.

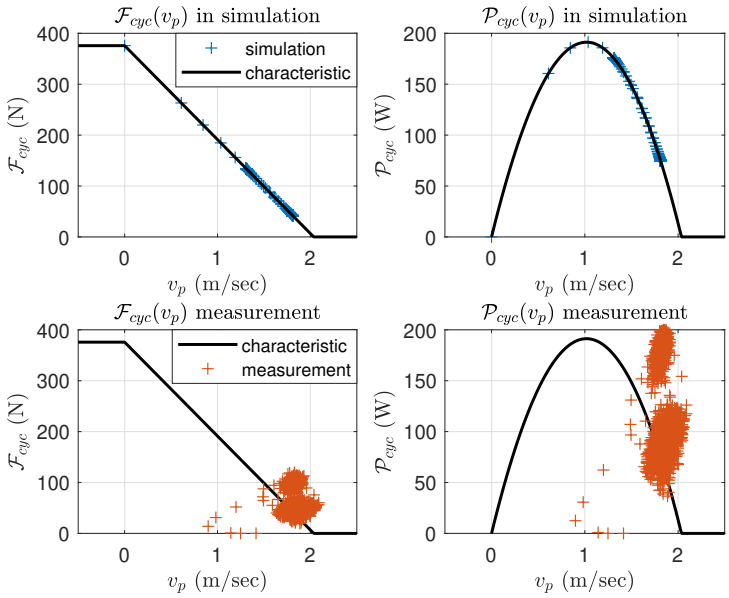

Figure 5.25: Comparison of the simulation and experimental data to the identified characteristics of the cyclist for scenario *In0*. The left column corresponds to the *force-velocity* characteristic and the right column to the *power-velocity* characteristic.

it can be seen that the experimental data points gather at the same $\mathcal{P}_{cyc}$ than the simulated characteristic, which is coherent with the observations in Fig. 5.23.

5.6.2 Validation on scenario *In1*

Then, the indoor scenario *In1*, with the PI controller, is reproduced in simulation. The evolution of the respiratory gas exchanges and the power developed by the cyclist and the electrical assistance is presented in Fig. 5.26. Similarly to the previous scenario, the power developed by the cyclist and the power developed by the electrical assistance are very well predicted in simulation. It is especially true during transients, where the spikes in $\mathcal{P}_{cyc}$ and $\mathcal{P}_{mot}$ are well reproduced. This is interesting because it makes the reading of the experimental respiratory gas exchange data easier to interpret, especially the variations in oxygen consumption during transients.

In Fig. 5.28, the evolution of the measured pedalling speed and torque as well as their simulated equivalents are shown. In this scenario, the simulated pedalling torque is very well predicted in simulation, but as for scenario *In0*, the cycling speed remains almost constant around the same value during the experimental scenario, which is not predicted by the characteristic.

Finally in Fig. 5.25, the force-velocity and the power-velocity characteristics are compared to the simulated and measured data. The same conclusions can be drawn for this scenario and the previous one. Initially, the experimental data points are located on the characteristics but because the pedalling speed remains constant during the exercise session, the experimental

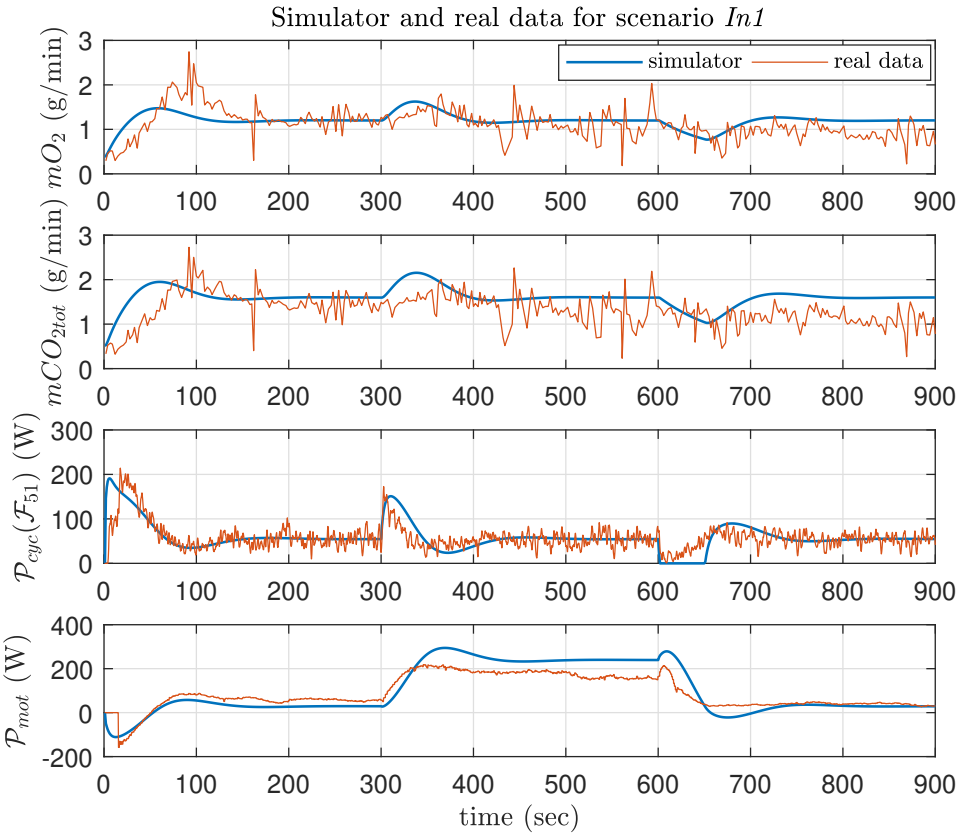

Figure 5.26: Evolution of the real and simulated cyclist oxygen consumption *(first figure)*, total carbon dioxide production *(second figure)*, power developed by the cyclist *(third figure)* and power developed by the motor *(last figure)* for scenario *In1*.

data points leave the characteristics and translate vertically.

5.6.3 Conclusion

Several conclusions can be drawn from the experimental results previously presented :

- *C1 - The simulation strategy based on a force-velocity characteristic of the cyclist appears to be a valuable tool to simulate realistic cycling behaviours.*

- *C2 - The force-velocity characteristic is able to produce high fidelity cycling power profiles in simulation, which enable an accurate predicting of the respiratory gas exchanges of the cyclist in chosen road profiles and cycling conditions.*

- *C3 - The force-velocity characteristic however does not reproduce the tendency of the cyclist to regulate its pedalling speed around a fixed value, which prevents the estimation*

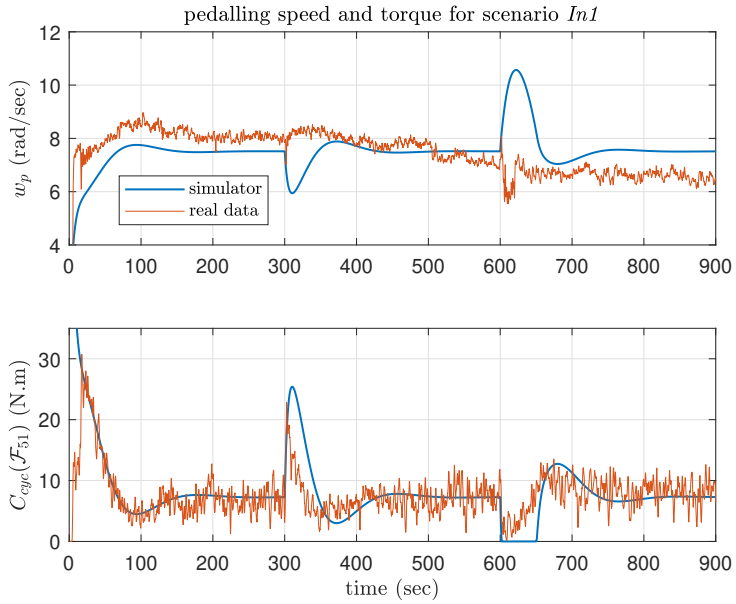

Figure 5.27: Evolution of the real and simulated pedalling speed *(first figure)* and pedalling torque *(second figure)* for scenario *In1*.

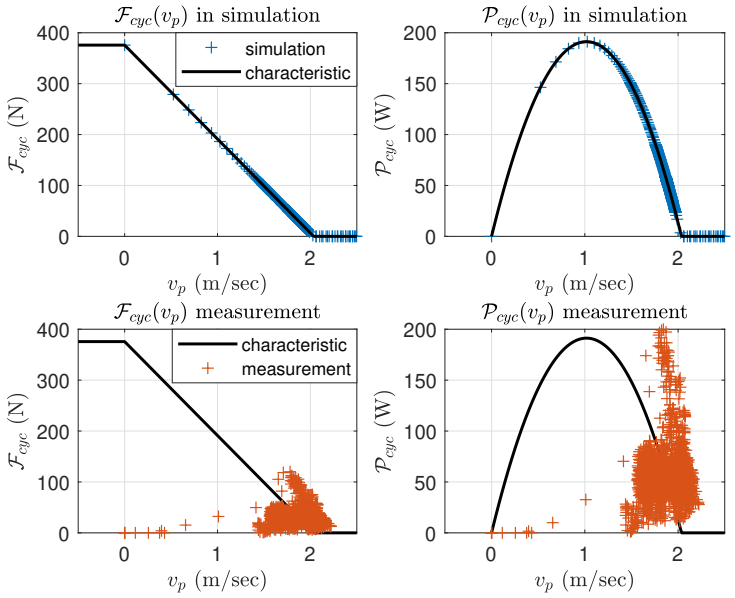

Figure 5.28: Comparison of the simulation and experimental data to the identified characteristics of the cyclist for scenario *In1*. The left column corresponds to the *force-velocity* characteristic and the right column to the *power-velocity* characteristic.

of realistic pedalling force and pedalling speed in simulation. This aspect can be further explored in order to improve the performances of the simulation strategy.

- *C4 - This simulation strategy is applicable to the tuning of control laws in simulation or to the prediction of the physiological stress experienced by an individual in a given exercise scenario.*

5.7 Conclusion

In this chapter, two control strategies aiming at controlling the respiratory gas exchange of an exercising cyclist are proposed. Both control strategies consist in controlling the electrical assistance of an e-bike in order to regulate the load perceived by the cyclist. Two main quantities can be controlled : the oxygen consumption and the carbon dioxide production during exercise.

The first control strategy is based on a proportional integral (PI) controller and the second one on a linear quadratic regulator (LQR). Both control laws were designed in simulation and validated experimentally after being implemented on an e-bike prototype. Both control laws were able to control the oxygen consumption of the cyclist during indoor and outdoor cycling tests and can be considered as valid candidates for future implementation on dedicated e-bike systems.

Also, in this chapter the performances of the simulation strategy used in this thesis in order to reproduce realistic cycling behaviours for a cyclist in simulation were examined. This control strategy is based on a pedalling *force-velocity characteristic* identified using experimental data. The control strategy proved to be a valuable tool for the design of the control laws since both of them were tuned and validated in simulation before practical implementation. Furthermore, the control strategy showed very good repeatability when compared to experimental data recovered during real biking scenarios.

Bibliography

[1] José A Afonso, Filipe J Rodrigues, Delfim Pedrosa, and João L Afonso.
Automatic Control of Cycling Effort Using Electric Bicycles and Mobile Devices.
In *Proceedings of the World Congress on Engineering 2015*, volume 1, page 6, London, U.K., 2015.

[2] José A. Afonso, Filipe J. Rodrigues, Delfim Pedrosa, and João L. Afonso.
Mobile Sensing System for Cycling Power Output Control.
In Paulo Garrido, Filomena Soares, and António Paulo Moreira, editors, *CONTROLO 2016*, volume 402, pages 773–783. Springer International Publishing, Cham, 2017.
Series Title: Lecture Notes in Electrical Engineering.

[3] E. Ammenwerth, G. Schreier, and D. Hayn.
Health Informatics Meets eHealth.
Methods of Information in Medicine, 49(03):269–270, 2010.

[4] Ahmadreza Argha, Steven W Su, and Branko G Celler.
Heart rate regulation during cycle-ergometer exercise via event-driven biofeedback.
Medical & biological engineering & computing, 55(3):483–492, 2017.

[5] Ahmadreza Argha, Lin Ye, Steven W Su, Hung Nguyen, and Branko G Celler.
Heart rate regulation during cycle-ergometer exercise using damped parameter estimation method.
In *2016 38th Annual International Conference of the IEEE Engineering in Medicine and Biology Society (EMBC)*, pages 2676–2679. IEEE, 2016.

[6] Mohammad Mostafa Asheghan and Joaquín Míguez.
Stability analysis and robust control of heart beat rate during treadmill exercise.
Automatica, 63:311–320, January 2016.

[7] Dur-e-Zehra Baig.
Physiological Control of Human Heart Rate and Oxygen Consumption during Rhythmic Exercises.
arXiv:1403.7105 [cs, q-bio], March 2014.

arXiv: 1403.7105.

[8] Dur-e-Zehra Baig, Andrey V. Savkin, and Branko G. Celler.
Self biofeedback control of oxygen consumption (Vo2) during cycling exercise: Based on its real time estimate.
In *2013 35th Annual International Conference of the IEEE Engineering in Medicine and Biology Society (EMBC)*, pages 477–480, Osaka, July 2013. IEEE.

[9] T.M. Cheng, A.V. Savkin, B.G. Celler, S.W. Su, and Lu Wang.
Nonlinear Modeling and Control of Human Heart Rate Response During Exercise With Various Work Load Intensities.
IEEE Transactions on Biomedical Engineering, 55(11):2499–2508, November 2008.

[10] Matteo Corno, Paolo Giani, Mara Tanelli, and Sergio Matteo Savaresi.
Human-in-the-Loop Bicycle Control via Active Heart Rate Regulation.
IEEE Transactions on Control Systems Technology, 23(3):1029–1040, May 2015.

[11] Daniel De La Iglesia, Juan De Paz, Gabriel Villarrubia González, Alberto Barriuso, Javier Bajo, and Juan Corchado.
Increasing the Intensity over Time of an Electric-Assist Bike Based on the User and Route: The Bike Becomes the Gym.
Sensors, 18(2):220, January 2018.

[12] Ali Esmaeili, Asier Ibeas, Jorge Herrera, and Nazila Esmaeili.
Identification and robust control of heart rate during treadmill exercise at large speed ranges.
Journal of Control Engineering and Applied Informatics, 21(1):51–60, 2019.

[13] Clement Girard, Asier Ibeas, Ramon Vilanova, and Ali Esmaeili.
Robust discrete-time linear control of heart rate during treadmill exercise.
In *2016 24th Iranian Conference on Electrical Engineering (ICEE)*, pages 1113–1118, Shiraz, Iran, May 2016. IEEE.

[14] K. J. Hunt and D. B. Allan.
A stochastic Hammerstein model for control of oxygen uptake during robotics-assisted gait.
International Journal of Adaptive Control and Signal Processing, pages n/a–n/a, 2008.

[15] Kenneth J. Hunt and Simon E. Fankhauser.
Heart rate control during treadmill exercise using input-sensitivity shaping for disturbance rejection of very-low-frequency heart rate variability.
Biomedical Signal Processing and Control, 30:31–42, September 2016.

[16] Kenneth J. Hunt and Sepp Gerber.
A generalized stochastic optimal control formulation for heart rate regulation during treadmill exercise.
Systems Science & Control Engineering, 5(1):481–494, January 2017.

[17] Kenneth J. Hunt and Ming Liu.
Optimal control of heart rate during treadmill exercise: Optimal control of heart rate during treadmill exercise.
Optimal Control Applications and Methods, 39(2):503–518, March 2018.

[18] Kenneth J. Hunt and Roman R. Maurer.
Comparison of linear and nonlinear feedback control of heart rate for treadmill running.
Systems Science & Control Engineering, 4(1):87–98, January 2016.

[19] Kenneth J. Hunt, Andreas Zahnd, and Reto Grunder.
A unified heart rate control approach for cycle ergometer and treadmill exercise.
Biomedical Signal Processing and Control, 54:101601, September 2019.

[20] K.J. Hunt, B. Ajayi, H. Gollee, and L. Jamieson.
Feedback Control of Oxygen Uptake During Treadmill Exercise.
IEEE Transactions on Control Systems Technology, 16(4):624–635, July 2008.

[21] K.J. Hunt and A. Bugmann.
Feedback control of human metabolic work rate during robotics-assisted treadmill exercise.
Biomedical Signal Processing and Control, 7(5):537–541, September 2012.

[22] Asier Ibeas, Ali Esmaeili, Jorge Herrera, and Farouk Zouari.
Discrete-time observer-based state feedback control of heart rate during treadmill exercise.
In *2016 20th International Conference on System Theory, Control and Computing (ICSTCC)*, pages 537–542, Sinaia, Romania, October 2016. IEEE.

[23] Nicholas A Jamnick, Robert W Pettitt, Cesare Granata, David B Pyne, and David J Bishop.
An examination and critique of current methods to determine exercise intensity.
Sports Medicine, 50(10):1729–1756, 2020.

[24] Theresa Mann, Robert Patrick Lamberts, and Michael Ian Lambert.
Methods of Prescribing Relative Exercise Intensity: Physiological and Practical Considerations.
Sports Medicine, 43(7):613–625, July 2013.

[25] Patrick Mayerhofer, Matt Jensen, David C. Clarke, James Wakeling, and Max Donelan.
Development of a Feedback System to Control Power in Cycling.

In *The 13th Conference of the International Sports Engineering Association*, page 22. MDPI, June 2020.

[26] Frederic Mazenc, Michael Malisoff, and Marcio de Queiroz.
Model-based nonlinear control of the human heart rate during treadmill exercising.
In *49th IEEE Conference on Decision and Control (CDC)*, pages 1674–1678, Atlanta, GA, USA, December 2010. IEEE.

[27] D Meyer, W Zhang, and M Tomizuka.
Sliding mode control for heart rate regulation of electric bicycle riders.
In *Proceedings of the ASME 2015 Dynamic Systems and Control Conference*, 2015.

[28] Hauke Neuber and Martin Strube.
Closed-Loop heartrate Control with Electric Bicycles for Cardiac Rehabilitation.
In *2020 21st International Conference on Research and Education in Mechatronics (REM)*, pages 1–5, Cracow, Poland, December 2020. IEEE.

[29] Michele Paradiso, Stefano Pietrosanti, Stefano Scalzi, Patrizio Tomei, and Cristiano Maria Verrelli.
Experimental Heart Rate Regulation in Cycle-Ergometer Exercises.
IEEE Transactions on Biomedical Engineering, 60(1):135–139, January 2013.

[30] A. Pennycott, K.J. Hunt, L.P. Jack, C. Perret, and T.H. Kakebeeke.
Estimation and volitional feedback control of active work rate during robot-assisted gait.
Control Engineering Practice, 17(2):322–328, February 2009.

[31] Andrew Pennycott, Kenneth J. Hunt, Sylvie Coupaud, David B. Allan, and Tanja H. Kakebeeke.
Feedback Control of Oxygen Uptake During Robot-Assisted Gait.
IEEE Transactions on Control Systems Technology, 18(1):136–142, January 2010.

[32] Jan Riedo and Kenneth J. Hunt.
Feedback control of oxygen uptake during robotics-assisted end-effector-based stair climbing.
Systems Science & Control Engineering, 5(1):142–155, January 2017.

[33] Amirehsan Sarabadani Tafreshi, Verena Klamroth-Marganska, Silvio Nussbaumer, and Robert Riener.
Real-Time Closed-Loop Control of Human Heart Rate and Blood Pressure.
IEEE Transactions on Biomedical Engineering, 62(5):1434–1442, May 2015.

[34] S. Scalzi, P. Tomei, and C. M. Verrelli.
Nonlinear Control Techniques for the Heart Rate Regulation in Treadmill Exercises.

IEEE Transactions on Biomedical Engineering, 59(3):599–603, March 2012.

[35] Matthias Schindelholz and Kenneth J. Hunt.
Feedback control of oxygen uptake profiles during robotics-assisted treadmill exercise.
IET Control Theory & Applications, 9(9):1433–1443, June 2015.

[36] Steven W. Su, Shoudong Huang, Lu Wang, Branko G. Celler, Andrey V. Savkin, Ying Guo, and Teddy M. Cheng.
Optimizing Heart Rate Regulation for Safe Exercise.
Annals of Biomedical Engineering, 38(3):758–768, March 2010.

[37] S.W. Su, Lu Wang, B.G. Celler, A.V. Savkin, and Ying Guo.
Identification and Control for Heart Rate Regulation During Treadmill Exercise.
IEEE Transactions on Biomedical Engineering, 54(7):1238–1246, July 2007.

[38] Cristiano Maria Verrelli, Patrizio Tomei, Giuseppe Caminiti, Ferdinando Iellamo, and Maurizio Volterrani.
Nonlinear heart rate control in treadmill/cycle-ergometer exercises under the instability constraint.
Automatica, 127:109492, May 2021.

[39] Nianfeng Wan, S. Alireza Fayazi, Hamed Saeidi, and Ardalan Vahidi.
Optimal power management of an electric bicycle based on terrain preview and considering human fatigue dynamics.
In *2014 American Control Conference*, pages 3462–3467, Portland, OR, USA, June 2014. IEEE.

[40] Y. Zhang, W. Chen, S.W. Su, and B. Celler.
Nonlinear modelling and control for heart rate response to exercise.
International Journal of Bioinformatics Research and Applications, 8(5/6):397, 2012.

Chapter 6

Discussion and conclusion

Contents

6.1 Discussion

In Chapter 2, key concepts of the exercise physiology theory were presented. Mainly, the existence of a connection between the power developed during an exercise session and the oxygen consumption and carbon production of the exercising individual. The nature of this link was examined by reviewing the different models to explain respiratory gas exchange that were proposed by the exercise physiology community. From a control science point of view, these models highlight the complex dynamics explaining respiratory gas exchange, including both linear and nonlinear components. Also, in this chapter, the benefits of exercise on health were presented. As such, this chapter constitutes a motivation to develop accurate models and control laws in order to control respiratory gas exchange during exercise, which is the main objective of this thesis.

In Chapter 3, the system studied in this thesis is defined. This system is constituted of both a cyclist and an electric bike. The aim of this chapter is to propose a description of the physiological, behavioural and mechanical interactions existing in this system. In order to describe the physiology of the exercising cyclist, a respiratory gas exchange model is used. A proposition to describe the behaviour of an exercising cyclist, in terms of pedalling force and pedalling speed, was given in terms of a *force-velocity* characteristic. Finally, the mechanical interactions between the bike, the rider and the environment are described using the first principle of dynamics. Based on theses three elements, a simulation strategy is proposed in order to reproduce realistic cycling behaviours in simulation for arbitrary road conditions and electrical assistance strategies. As such, this chapter constitutes the *modelling* and the *simulation* steps of the control science approach to the control of respiratory gas exchange during exercise. In this thesis, these modelling and simulation choices turned out successful to provide a simple but complete description of the bike and cyclist system and were mainly used to design control laws for the electrical assistance of the bike.

In the future, additional modeling efforts could be done in order to improve the cyclist model. For example, a description of the fatigue of the cyclist could be added in the model based on blood lactate. Additional physiological variables, like heart rate, could be added in order to propose a more complete description of the physiological status of the cyclist. In this thesis, the model describing the respiratory gas exchange of a cyclist is identified *once* using exercise tests data. However, it is yet not known if this model remains valid for long periods of time after identification, and especially if the training or health condition of the considered individual affects its accuracy. Thus a study of the evolution during time of the identified gas exchange model could be explored. Finally, the *force-velocity* characteristic proved to be a useful tool in order to generate realistic cyclist power profiles in simulation. However, this characteristic tends to underestimate the tendency of the cyclist of regulate its pedalling speed

around a fixed value, which prevents it to generate realistic pedalling force and pedalling speed profiles in simulation. In the future, the *force-velocity* characteristic could be improved to this end.

In Chapter 4, estimation strategies are proposed in order to estimate the respiratory gas exchange of the cyclist during exercise. The first one is an Explicit Error Bounds Set-Membership observer and is used to estimate the oxygen consumption, *aerobic* carbon dioxide production and the anaerobic carbon dioxide production during exercise based on ventilation or carbon dioxide measurements. By design, this state observer is robust to state and output disturbances and provides uncertainty bounds on the estimated states. The second one is a Robust Proportional Integral observer and is used to estimate respiratory gas exchange and reconstruct model errors under the form of a basal power disturbance based on ventilation or carbon dioxide measurements. It can be used to estimate respiratory gas exchange with good accuracy even when the respiratory gas exchange model is slightly inaccurate or to reconstruct the basal metabolic rate of the cyclist during exercise. Both estimation strategies are validated in simulation.

The main difficulty of estimating respiratory gas exchange during exercise is the invasiveness of the gas exchange measurements, since a mask is required. Both solutions proposed in this chapter are based on measurements of the carbon dioxide production or of the ventilation, which are both performed using a spirometry mask. In the future, solutions to estimate respiratory gas exchange in a *non-invasive* and *accurate* fashion are needed in order to propose an easy to use solution for the control of respiratory gas exchange during exercise using an e-bike. To do so, additional non invasive measurements could be considered, like the body temperature, or the heart rate during exercise.

Finally, In Chapter 5, two control laws are proposed in order to regulate the oxygen consumption or the carbon dioxide production during exercise using the electrical assistance of an e-bike. The first control law is a proportional integral (PI) controller and the second one an LMI-based linear quadratic regulator (LQR). Both control laws are designed in simulation, using the simulation strategy proposed in Chapter 3, and then validated during experimental indoor and outdoor scenarios. Both control strategies show encouraging results. The simulation strategy itself is validated using experimental data and proves to be able to generate accurate respiratory gas exchange profiles, cyclist power output profiles and control effort profiles.

In this chapter, both control laws perform well in simulation, especially the linear quadratic regulator (LQR). However, in order to be implemented on the real system, the respiratory gas exchange model is used in *open loop* in order to provide the required information regarding the states of the system to the controllers. Because of this implementation choice, it is hard to

conclude regarding the performances of the controllers since none of them has access to a live measurements of the system states, but only to *open loop* estimates. In the future, with more accurate and less invasive estimation strategies for respiratory gas exchange estimation, the performances of both controllers could be assessed more accurately. Also, in the considered experimental scenarios, the choice of a low reference value for the oxygen consumption turned out questionable, and more experimental tests using a larger variety of references is needed. Longer outdoor biking tests, including a larger variety of raod profiles could also be considered for the evaluation of the controllers' performances.

6.2 Conclusion

To conclude, in this thesis a control system approach to the problem of regulating the exercise intensity of a cyclist was proposed. This approach is based on the control of the respiratory gas exchange of the cyclist using the electrical assistance of an e-bike. To do so, several contributions were made. First, a complete model of the cyclist and bicycle was proposed based on a respiratory gas exchange model and on a *force-velocity* characteristic of the cyclist. Based on this cyclist characteristic, a simulation strategy generating realistic respiratory gas exchange and cyclist power profiles was proposed. Two methods were proposed in order to estimate the respiratory gas exchange of the cyclist, one based on an Explicit Error Bounds Set-Membership observer and one based on a Robust Proportional Integral state observer. Two control laws were proposed in order to control the oxygen consumption or the carbon dioxide production of the cyclist during exercise, one based on a Proportional Integral (PI) controller, and one on a LMI-based Linear Quadratic Regulator (LQR). Both control laws were implemented on an e-bike prototype and validated in real *outdoor* and *indoor* conditions.